5-2021

In situ Laser Synthesis, Processing and Characterization in the TEM

Chenze Liu
cliu74@vols.utk.edu

To the Graduate Council:

I am submitting herewith a dissertation written by Chenze Liu entitled "In situ Laser Synthesis, Processing and Characterization in the TEM." I have examined the final electronic copy of this dissertation for form and content and recommend that it be accepted in partial fulfillment of the requirements for the degree of Doctor of Philosophy, with a major in Materials Science and Engineering.

Gerd Duscher, Major Professor

We have read this dissertation and recommend its acceptance:

Matthew F. Chisholm, David B. Geohegan, Gong Gu, Philip D. Rack

Accepted for the Council:

Dixie L. Thompson

Vice Provost and Dean of the Graduate School

(Original signatures are on file with official student records.)

In situ Laser Synthesis, Processing and Characterization in the TEM

A Dissertation Presented for the
Doctor of Philosophy
Degree
The University of Tennessee, Knoxville

Chenze Liu
May 2021

DEDICATION

This doctoral dissertation is dedicated to my parents Shunxiang Liu and Yunhua Chen, my parents-in-law Fangwang Ye and Wenxiu Chen, my husband Youxiong Ye, and my daughter Celina Ye

ACKNOWLEDGEMENTS

I would like to express the immeasurable appreciation and deepest gratitude to people who have helped and supported me to achieve my goals during my graduate study at the University of Tennessee, Knoxville. Without them, this dissertation would not have been possible.

Foremost, I owe a deep debt of gratitude to my academic advisor Dr. Gerd Duscher for his continuous support, encouragement, guidance, and suggestions that benefited me much in the completion and success of my PhD study. His profound knowledge and expertise about transmission electron microscopy helped me in building my interest and career for a lifetime. He is such a considerate and open-minded friend of mine that makes my life as a graduate student meaningful, colorful, and memorable. I could not have imagined having a better mentor and friend for my PhD study.

I would also like to thank the rest of the committee members, Dr. David B. Geohegan, Dr. Matthew F. Chisholm, Dr. Philip D. Rack, Dr. Gong Gu. I express my warmest gratitude to Dr. David B. Geohegan for sponsoring me for my graduate program. His guidance into the synthesis of two-dimensional material by pulsed laser deposition has been a valuable input for this dissertation. He is also a true friend in our daily life; we postdocs and students had a lot fun with him playing kayaking and golfing. I am grateful to Dr. Matthew F. Chisholm. His insightful comments and suggestions on understanding the structure of material using electron microscope inspired me to optimize the operation of the Nion UltraSTEM and seek alternative approach in an objective perspective. I gratefully acknowledge the contributions of Dr. Philip D. Rack. His expertise in interpreting the plasmon modes of silver nanoparticles and his commitment towards the project was a significant influence in shaping many of the concepts presented in this dissertation. I would like to thank Dr. Gong Gu for letting me work with their group and for providing valuable insight on my work.

I also appreciate the collaborators who have provided me with a lot of helps during my research. Dr. Kai Xiao, Dr. Alexander A. Puretzky, Dr. Gyula Eres, Dr.

Christopher M. Rouleau guided me in completing my research projects. Dr. Yu-Chuan Lin, Dr. Yiling Yu, Dr. Yueying Wu, Dr Yiyi Gu, Dr. Akinola Oyedele provided me with samples and brought me creative ideas during discussion. I am thankful to Dr. Mina Yoon, Dr. David J. Masiello, Dr. Michael G. Stanford for their collaborations on simulation. Thanks also go to Dr. John Dunlap at JIAM for his continuous help and the training of various instrument operations.

It is a pleasure to thank my groupmates and friends, Dr. Mengkun Tian, Dr. Jingxuan Ge, Nicholas Cross, Cody Pratt, Krishna Koirala for their frequent help and support. In addition, I would like to thank all my friends at the University of Tennessee and Oak Ridge National Lab who shared wonderful time with me and made my graduate life memorable, including Dr. Yuan Li and his wife Wanyi Yan, Dr. Peijun Hou, Dr. Wei Zhang, Dr. Xue Wang, Dr. Ling Wang, Mr. Miaosheng Wang, Dr. Hui Wang, Mr. Zengquan Wang, Dr. Rui Feng, Dr. Shuying Chen, Ms. Nan Huang, Mr. Yongtao Liu, Ms. Robyn Collette, Mr. David A. Garfinkel, Ms. Di Xie, Mr. Xuesong Fan, Ms. Yajie Zhao and Mr. Zongyang Lyu.

I am indebted to my family for their continuous and unparalleled love, help and support. I acknowledge my husband, who shares every important moment together with me, happy or sad. My life would be incomplete without him. I am grateful to my parents who are always supportive to my decisions no matter what it is. This journey would not have been possible if not for them.

Thanks to the sponsorship from U.S. Department of Energy, Office of Science, Basic Energy Sciences (BES), Materials Sciences and Engineering Division. We thank the Joint Institute of Advanced Materials for microscopy access.

ABSTRACT

Rapid materials synthesis, processing and characterization enables a wide variety of materials systems with tuned properties. The objective of this dissertation is to demonstrate how a prototype setup allows laser illumination to be coupled into a (scanning) transmission electron microscope (TEM) for real-time observations of synthesis, processing, and characterization.

The laser synthesis of two-dimensional (2D) crystals and van der Waals (vdW) heterostructures is investigated through stepwise laser crystallization within a TEM. Amorphous tungsten selenide that was deposited by pulsed laser deposition (PLD) evolves through a series of metastable nanophases as crystallizing and coalescing into continuous 2D WSe_2 domains on monolayer graphene or $MoSe_2$ substrates. The lattice-matched $MoSe_2$ substrate is shown to play a guiding role in the formation of heteroepitaxial vdW $WSe_2/MoSe_2$ bilayers both during the crystallization process and afterwards, when crystalline nanosized domains are observed to coalesce by rotation, and grain boundary migration processes. In addition, the controllable implantation of hyperthermal species from PLD plasmas is introduced as a top-down method to compositionally engineer 2D monolayers and form Janus monolayers using *in situ* diagnostics. The chalcogen atoms on both sides of transition metal dichalcogenide (TMD) were resolved by grid tilting and the Janus structure of TMD was confirmed in atomic resolution for the first time. These *in situ* studies of pulsed laser-driven crystallization and implantation represent a transformational tool for the rapid exploration of synthesis pathways and lend insight to the growth of 2D crystals by PLD and laser processing methods.

Laser characterization within the TEM is demonstrated via experimentally accessing photon-stimulated electron energy-loss (sEEL) and electron energy-gain (EEG) responses of individual plasmonic nanoparticles via photon-plasmon-electron interactions induced by simultaneous irradiation of a continuous wave laser and continuous current electron probe. EEG and sEEL probabilities are equivalent and increase linearly in the low irradiance range; importantly the photon energy must be tuned in resonance with the plasmon energy for the sEEG and

sEEL peaks to emerge. This study opens a fundamentally new approach to explore the quantum physics of excited-state plasmon resonances that does not rely on high intensity laser pulses or any modification to the EELS detector.

TABLE OF CONTENTS

LIST OF TABLES

LIST OF FIGURES

Chapter 1. Introduction

Coupling laser illumination into a transmission electron microscope (TEM) allows real-time observations of synthesis, processing, and light-matter-electron interactions. By virtue of the capability of this optical system, we investigate how small building blocks (atom aggregates) can be assembled to novel materials with *in situ* laser heating and how the quantum physics of excited-state plasmon resonances can be characterized. Here we review the phases, structures, morphologies, and properties of the materials investigated, and laser synthesis and characterization method that are relevant to this dissertation.

1.1 Nano Materials

Nanomaterials are defined as materials composed of substances with sizes of 100 nanometers or smaller in at least one dimension, then the materials' properties change significantly from those bulk counterparts.[1] Thus, nanostructures show unique optical, electrical, and magnetic behavior compared to their bulk counterparts attributing to their specific aspect ratios and confinement effects. At nanoscale, properties such as melting point, magnetic permeability, electrical conductivity, and chemical reactivity, fluorescence change with the size scale.[2] By definition, nanomaterials are not in equilibrium. They have a tendency to aggregate and agglomerate with time. So nano-materials can serve as building blocks (it turned out that nano-particles are actually too big to be good building blocks) and as final structures for the research goal. In this dissertation, transition metal dichalcogenides (TMD) nanoparticles were used as the precursors for synthesis of atomically thin two-dimensional (2D) TMD materials, and plasmonic-metal nanostructures were used to characterize the light-matter-electron interactions. The introduction of 2D TMD and plasmonic-metal nanostructures are provided below.

1.1.1 Two-dimensional transition metal dichalcogenides

The discovery of two-dimensional (2D) graphene opens new directions for replacing conventional semiconductors in future optoelectronic devices due to its extremely high electron and hole mobilities and sensitivity to environmental charges.[3, 4] However, because of the small electronic bandgap, graphene retards its application in logic electronics. Recently, monolayers (MLs) of transition metal dichalcogenides (TMD) materials, MX_2 (M=Mo, W; X=S, Se, Te), have attracted great attention owing to their layered structure analogous to graphene. The transistors fabricated with TMD atomic thin layers exhibit extraordinary electrical and optical properties due to changes in the band structure that result from quantum confinement, which make them suitable for next generation transistors.[3, 4] Recently, stacking of two different MLs TMD heterostructure has gain great attention.[5, 6] The hetero-bilayer with a van der Waals (vdW) interface has gain a lot of interest because of the novel optical and transport properties with a rich variety of device physics.[7] In addition, the stacking orientation significantly impacts the interlayer coupling at the interface, therefore, it's possible to tailor the electronic structure of the hetero-bilayer by simply changing the twist angles.[7] Notably, compositional engineering can greatly expand the functionality of atomically thin 2D materials. In our group, we used a simple process to implant atoms precisely into the top layers of ultra-thin crystals and form Janus 2D TMD crystals[8] and the details are describe in section 1.2.3.

In chapter 3, mixtures of 2D chalcogenides and their stacking are produced from different starting materials with a large variation in the building blocks. This synthesis was carried out largely by laser processing within the TEM. In chapter 4, Janus structure of TMD are fabricated using low energy implantation of pulsed laser deposition.

1.1.2 Plasmonic-metal nanostructures

A plasmon is a quasi-particle quantizing collective oscillations of free valence electrons.[9] When a plasmon is excited at the dielectric–metal interface of the materials, this plasmon is a so-called surface plasmon.[10] Plasmonic-metal nanostructures are featured by the manifestation of a resonance with incident photons through an excitation of surface plasmon resonance (SPR).[11] Due to the dramatically enhance light-matter interactions, plasmonic metallic nanostructures have a variety of applications such as surface-enhanced plasmonically enhanced photovoltaics (PV), Raman spectroscopy (SERS), photocatalysis, and subwavelength waveguides.[12] The ability of nanostructured metals to efficiently support plasmons in response to illumination and other electromagnetic fields has implications on many scientific fields and applications such as optoelectronics, [13-15] optical computing,[16, 17] and readout strategies for quantum computing.[18, 19] Furthermore, because plasmon excitations are sensitive to their environment, there are intriguing biological and chemical processes that can be probed using environment-induced plasmon modulation.[20, 21] Plasmons can also transfer electromagnetic energy radiatively,[22] non-radiatively,[23] and/or via hot electron injection and thus can be used to catalyze reactions.[24-26] Because of these, and other, emerging uses, a deeper understanding of plasmons is essential.

Different metals have different SPR. For example, the frequencies of surface plasmons of gold, silver, nickel and copper nanoparticles is in the ultraviolet (UV) and visible (vis) range. Because the UV-vis range is of most commercial interest, metals such as Au, Ag, Ni and Cu have gained great attention to be used as plasmonic-metal nanostructures. The energetic and spatial profiles of surface plasmons can be tuned by changing the nanoparticle's material, size, shape, electronic charge and surrounding medium.[11, 27] Also, mixing metallic alloys serve as a significant method to tune the energy of plasmons and other properties of these nanostructures.[28] Therefore, it is possible to design the plasmonic-metal nanostructures with the desired plasmonic functionalities.

In chapter 5, we demonstrated how high energy resolution of a monochromated TEM combined with laser-activated evanescent light fields allows us to better characterize surface plasmons.

1.2 Laser synthesis and processing

Rapid materials synthesis and characterization of materials systems is critical to advances in a wide variety of applications from electronic devices to more fuel-efficient automobiles. As a method of rapid synthesis, laser synthesis and processing of materials is a field still in its infancy, but it is hot and growing.

1.2.1 Timescale of laser synthesis

The lasers in different timescale like femtosecond (1 fs = 10^{-15} s), picosecond (1 ps = 10^{-12} s), and nanosecond (1 ns = 10^{-9} s) have been used to synthesize and characterize lots of novel materials. Phillips et al. reviewed the different characteristics of laser with different timescale published in *Advances in Optics and Photonics*.[29] They pointed out that compared with pulses with longer widths, ultrashort pulses are exceptional due to their extremely high peak intensities and ultrafast interaction with materials even faster than lattice disordering and heat diffusion.[29] Therefore, ultrafast lasers can manipulate and control the states of materials very precisely attributed to these two kinds of features.

When the surface of the sample absorbs the front part of a femto-second pulsed laser, a dense electron-hole plasma is generated due to the extreme electronic excitations.[30] Then the energy of plasma passes to the lattice, which leads to the disorder of the lattice through cold atom movements. Hence, the sample is at a super nonequilibrium state with a high temperature electron gas within a cold lattice. According to the interaction of the pulse with the sample, the response of the sample after absorption can undergo three different pathways:[29]

1) Nonthermal melting: A nonthermal ultrafast phase transition will be induced when a pulse energy large is enough to excite 10%-15% of the bound valence

electrons to the conduction band in order to achieve a critical density of conduction band electrons (10^{22} cm^{-3}).

2) Thermal phase melting: If a sudden disordering of the lattice is not caused by the pulse energy, the energy of the plasma will pass to the lattice through electron–phonon coupling during a few ps. Then the heat will spread inside and increase the temperature of the local lattice. If the temperature is higher than the melting temperature, melting occurs.
3) Ablation: If the pulse energy is large then boiling occurs at the melted surface; the resulting superheated liquid phase and high nucleation rates of the gas phase cause material to be ejected from the surface. This process is known as ablation.

Compared with femto-second laser, nanosecond laser excites electrons in a markedly different way. When a nanosecond pulse arrives at the surface of the sample and delivers energy to the sample, the excited electrons spread energy to the lattice at the same time with the excitation of electron. Therefore, during the excitation, the lattice and electrons stay in equilibrium. That is, the melting temperature of the materials is rapidly reached within this nanosecond laser pluse. [31] The nanosecond absorption is linear with a much larger absorption length than femto-second absorption. Thus, the nanosecond absorption can reach deeper melt depths. Comparing femto-second absorption, nanosecond absorption will lead to a more uniform temperature distribution. Consequently, the time of melting is larger, and the speed of resolidification-front is smaller. If the laser energy lies in the transparent range the sample, multiphoton absorption occurs for both femto-second and nanosecond absorption. However, the nanosecond laser will have a deeper melt depth attributed to a smaller absorption cross-section comparing with an femto-second laser. However, if the laser energy is in the opaque range of the sample, the melt depth is dependent on the absorption coefficient attributed to single photon absorption. For a small absorption coefficient, a shallower melt depth of the femto-second laser may be attained attributed to a mixture of nonlinear and

linear absorption. Compared to ultrafast lasers, the longer nanosecond pulse widths reach lower peak powers. Working at lower peak powers, the ablation of materials by nanosecond lasers is a thermal process.[32] Shockwaves and melt redeposition may occur due to large heat-affected zone induced by this thermal process, and at this circumstance, defects such as chipping and cracks are induced.

Since the laser widths we used in our study are nanosecond or longer, these processes are thermal heating or annealing, which can be compared with normal heat annealing. In the following we will review the impact of this difference in laser matter interaction for the synthesis of the starting material and the subsequent recrystallization.

1.2.2 Synthesis by pulsed laser deposition

Laser ablation happens when the laser energies are larger than that of the ablation threshold. Laser ablation can be used for film deposition, mainly oxide/superconductor films or nanocrystals/nanotubes. The application of laser ablation in synthesis of 2D materials is through pulsed laser deposition (PLD). Pulsed laser deposition (PLD) is a versatile method that has been a mainstay for the epitaxial growth of oxide thin films as thin as one unit-cell, as well as complex heteroepitaxial superlattices. For example, the stoichiometric MoS_2 with controllable number (1–10) of layers was synthesized by PLD using ns-pulse 248 nm ablation (1–3 J/cm^2) with typically sulfur-rich mixed powder as the targets onto a variety of substrates at 700–850 °C in vacuum.[33]

It is challenging to control the stoichiometry, areal uniformity, crystallite size, number of the layers, and growth location using conventional vapor-phase synthesis [34]. In contrast, PLD has the advantage of controlling these parameters in the growth of 2D crystals by a variety of in situ diagnostics. Especially, the kinetic energy of the plasma plume can be tuned by changing the Ar background pressure, distance from target to substrate. The type of precursors arriving at the

substrate could also be adjusted from amorphous clusters to crystalline nanoparticles. Geohegan et.al summarized pulsed laser deposition of two-dimensional materials in the Chapter 1[33] of *Advances in the Application of Lasers in Materials Science*. They showed that in situ intensified charge couple device (ICCD) can be used to adjust the species of plasma plume and produce “building blocks” as desired. An excimer laser (KrF 248 nm, 20 ns full width at half maximum (FWHM)) was used to ablate the GaSe target and transfer precursors on to the target. Using this technique, lateral and vertical GaSe was synthesized by controlling the temperature and the deposition rate from amorphous precursors deposited in vacuum at room temperature.[3] Therefore, PLD is an appropriate tool to fabricate two dimensional TMD materials with different morphology through adjusting deposition conditions.[34] Although successful deposition of thin films has been demonstrated by PLD, the guiding mechanisms of assembly are poorly understood and hinder the widespread development of such PVD approaches in general. Therefore, the nanoscale mechanisms of 2D film growth by which amorphous precursors crystallize and coalesce to form continuous, atomically thin two-dimensional (2D) crystals are investigated through stepwise laser crystallization within a TEM. The details are described in Chapter 3.

1.2.3 Laser conversion of 2D materials

A great advantage of PLD is the ability to moderate the kinetic energy of plasma plume arriving at the substrate using background gas collisions,[35-37] therefore, it can be used to implant atoms precisely into the top layers of ultra-thin crystals. In laser-ablation plasmas used for PLD the kinetic energy of species can exceed 100 eV in vacuum, allowing the synthesis of metastable phases (e.g., amorphous diamond by laser ablation of graphite).[35] PLD of sulfur in vacuum was shown to controllably replace Se atoms in monolayer $MoSe_2$ crystals at 700 °C to digitally tune the composition of $MoS_{2x}Se_{2(1-x)}$ alloys, eventually resulting in total conversion to MoS_2 with successive pulses.[38] A great advantage of PLD is the ability to

moderate the kinetic energy of species arriving at the substrate using background gas collisions.[3, 35, 37]

Janus monolayer TMDs are intriguing compositionally-engineered 2D materials in which different chalcogens occupy the top and bottom of a monolayer (ML).[39, 40] The broken symmetry and permanent dipole moment inherent in Janus monolayers offer enhanced functionality, such as piezoresponse,[39, 41] catalytic behavior,[40] and charge separation.[42] Therefore, in chapter 4,[8] we explore precise tailoring of the hyperthermal nature of pulsed laser ablation plasmas to implant Se species into WS_2 ML.

1.2.4 Laser annealing and recrystallization

Annealing is a method to change the crystallinity and performance of a material through a kinetically equilibrium process. Traditionally, annealing is performed using furnaces at an elevated temperature. The traditional thermal annealing has a limitation of not able to heat a specific layer in a multilayer stack. In contrast, ultrafast laser annealing is an extremely nonequilibrium process. Laser annealing using both continuous-wave (CW) and pulsed diode and excimer lasers was adopted to achieve the site-specific annealing.[43, 44] For example, Kwon et al. used picosecond, pulsed laser to anneal the Au/Ti films contacts to enhance the performance of multilayer MoS_2 field effect transistors (FETs) on flexible plastic substrates without thermal damage.[45] The temperature of the substrate remains low (<200 °C) during the annealing process, which is compatible with the flexible PEN substrate.

The lack of methods to produce large-scale, high quality films on all kinds of substrates has slowed the commercial application of 2D materials such as transition metal dichalcogenides. Recently, McConney et al. demonstrated the synthesis of high quality, few-layer TMD films on stretchable polymeric materials by magnetron sputtering and following laser annealing under 514 nm CW laser

radiation.[46] This new method is of big breakthrough toward commercial application of two dimension based flexible/stretchable electronics.

1.3 In situ laser characterization in the TEM

We reviewed the possibilities of laser synthesis and processing; we will now discuss how laser irradiation combined with TEM can lead to a deeper understanding of electron-matter-light interaction. State-of-the-art TEM with ultra-high resolution is the ideal tool to reveal the structure and property of nanomaterials. Albeit standard TEM provides plenty of information regarding to the static structure and property, the dynamic structure-property relationship is essentially required for the investigation of non-equilibrium processes.

Sophisticated modifications have been applied to improve the versatility of standard TEM techniques such as electron diffraction, phase- and z-contrast imaging, and electron energy-loss spectroscopy. In this circumstance, in-situ TEM has gain great attention that reveals the nanostructure and property of the materials at ultra-high resolution in response to external stimuli, such as laser, heat, electrical current, and mechanical force.[47] With this technique, the size, morphology, property, crystallinity, and property of the nanomaterials can be measured in real-time under the external stimuli. Therefore, the true dynamic of structure-property relationships can be revealed with reduced uncertainty. Among all these stimuli, lasers are of great interest because it is not only a synthesis and processing tool, but also a pump probe to characterize the optical and optoelectronic properties of a material. Especially, optical spectroscopies (such as Raman, CL and PL) and optoelectronic experiments can be performed with in situ laser characterization in the TEM.

1.3.1 in situ Raman in the TEM

Raman spectroscopy provides information about vibrational, rotational, and other low-frequency modes in molecules based on inelastic scattering of monochromatic photons.[48] The shapes and positions of the Raman peaks could

provide useful information such as defect density, structure chirality, chemical composition, temperature, stress/strain, and magnetization.[49, 50] Thus, combining in situ high resolution imaging with in situ Raman spectroscopy could reveal much more useful information of the materials. Allen et al. set up a prototype that combine both laser processing and in situ Raman spectroscopy within a TEM.[49] This prototype reveals not only the dynamic microstructural change in MoS_2 flake, but also the Raman response during the pulsed laser ablation.

1.3.2 in situ cathodoluminescence and photoluminescence in the TEM

Cathodoluminescence characterization is performed by acquiring the luminescence (emission of a photon) from a material when stimulated by the incident electron beam inside an electron microscope. The luminescence energy can be detected is in the range of ultraviolet to infrared wavelength (200-2300 nm or 6-0.5 eV). Cathodoluminescence is a significant tool because it is able to acquire information of a sample down from a nanoscale region by focusing the incident electron beam within the TEM or SEM to a sub-nm length scale.

Photoluminescence (PL) is performed by acquiring the luminescence from a material under the excitation by light energy or photons. The electrons of the material transit to a higher electronic state under the photo excitation, then energy releases (emit a photon) by returning to the ground state. PL has high sensitivity and it is non-destructive to sample. The composition, structure and electronic information of the materials can be easily revealed by PL. In addition, PL can be used to determine band gap, detect impurity and defect levels, investigate the recombination mechanisms. Therefore, PLD has a widely application in academic and industry in fields like materials science, physics, biology, and chemistry.

In situ cathodoluminescence and photoluminescence characterization in the TEM open a way to reveal dynamical information of a sample during synthesis, processing, characterization, and to evaluate its possibilities for commercial applications. For example, Kizuka et al. installed the scanning optical fiber in high-

resolution TEM for in situ cathodoluminescence and photoluminescence characterization.[51] And they found a strange phenomenon that, some ZnO nanoparticles were luminescent, while some other particles were not, albeit all particles were from the same batch. Interestingly, both kinds of particles were similar in crystal structure, but the non-luminescent particles were smaller in size. This observation is of significance because it could not be observed by convention techniques. Therefore, such in situ techniques help to better understand of the properties of the material and show scientists a clearer way towards better design of an optical products.

1.3.3 Energy Gain via Photo-induced excitation

Optical pump-probe strategies have long been critical tools to unravel complex materials phenomena. While the probe size typically limits spatial resolution, the temporal domain of pump-probe techniques is virtually un-paralleled with sub-femtosecond laser pulses. To push the spatial resolution, over the past two decades optical pumps and focused electron probes have merged into ultrafast electron microscopies (UEMs) with modalities such as diffraction[52, 53] and photo-induced near field electron microscopy (see refs[54-58] for recent perspectives and reviews). For instance, 4D (x, y, z, t) UEM systems utilize photocathodes, which are exposed to short laser pulses to generate electron beamlets (and single electrons) that synchronously arrive at the sample relative to a pulsed laser. Though only a few UEM systems exist worldwide, a wealth of interesting excited state nearfield information has been revealed as described below.

Electron energy-gain due to electron/phonon coupling was first observed by Boerch et al. in 1966[59] and more recently in high energy resolution scanning transmission electron microscopy ((S)TEM)-based electron energy-loss spectroscopy (EELS).[60] Photoinduced electron energy-gain (EEG) spectroscopy was first suggested by Howie,[61] and later García de Abajo et al.[62] developed a theoretical framework for EEG and suggested optical power densities of $\sim 10^{10}$

W/m^2 would be necessary to observe continuous wave (CW) EEG spectroscopy of gold nanostructures. More recently, Barwick et al.[63] introduced photo-induced nearfield electron microscopy (PINEM), which couples an intense laser pulse indirectly to a fast electron probe through the laser-induced evanescent nearfield of the target material, thereby generating stimulated electron energy-loss (SEEL) and EEG signals at discrete quanta of photon energy (+/-n$\hbar\omega$). They studied the electron energy-gain and stimulated energy-loss spectra of carbon nanotubes and compared them to silver nanorods.[63] The ~10^{14} W/m^2, 200 fs pulses produced symmetric gain/loss spectra evidencing photon-plasmon-electron interactions involving up to 8 photon quanta. Later, energy-filtered PINEM maps were used to image the interference of Fabry-Perot type surface plasmon polariton waves [54] as well as to visualize the channel-like patterns formed in the near-fields of entangled silver nanoparticles.[64] Recently, spectrally resolved PINEM experiments of silver nanorods have confirmed that optical energy resolutions of ~20 meV can be obtained via a tunable light source.[65] Theoretical treatments of photoinduced EEG have also been developed[66-69] and it was suggested that continuous wave (CW) EEG can be realized with irradiance values on the order of 10^8 W/m^2 for silver nanoparticles, though some have hypothesized[56] that impractically high sample heating would result at these CW irradiances, thus rendering CW EEG/SEEL unfeasible.

In chapter 5, we demonstrated experimental accessing of the sEEL and EEG responses of plasmonic nanoparticles via the simultaneous irradiation of electron and a continuous wave laser.

1.4 Motivation of setup optical delivery system in the TEM

Rapid materials synthesis and characterization of materials systems is critical to advances in a wide variety of applications from electronic devices to more fuel-efficient automobiles. To accomplish this, one critical pathway is the development of combinatorial approaches to rapidly synthesize multicomponent material

libraries.[70-72] Another critical need is the development of in situ and rapid ex situ characterization approaches, so that materials can be exposed to external stimuli and the subsequent responses can be measured to elucidate, for instance, the free-energy landscape of various phase transformations. Among the various characterization techniques (scanning) transmission electron microscopy [(S)TEM], and its associated spectroscopic complements, is one of the few techniques in which this information can be gathered with atomic scale resolution. Thus, there has been a concerted effort to develop various in situ accoutrements for the (S)TEM,[73-75], examples include: in situ heating stages, gas[76] and liquid cells[77], optical delivery and collection[47, 78, 79]. Furthermore, over the past few decades, a few groups across the world have developed very complex and specialized ultrafast electron microscope or dynamic TEM systems using photo-cathodes that are exposed to short laser pulses to generate electron beamlets (and single electrons), that synchronously arrive at the sample in time relative to another pulsed laser directed at the same sample.[54, 55, 80-84]

Chapter 2. Experimental Method

In this chapter, all the methods used for synthesis, characterization, and calculation involved in this study will be described. The optical system overview is discussed in section 2.1, in situ laser synthesis of Van der Waals bilayer are described in section 2.2, formation of Janus structure of WSSe are described in section 2.3 and characterization of plasmonic state by stimulated electron energy gain are discussed in section 2.4. The temperature estimated during laser irradiation are described in section 2.5.

2.1 In Situ Photon Delivery System Overview

A new optical delivery system has been developed for the (scanning) transmission electron microscope. In this chapter, we describe the in situ and “rapid ex situ” photothermal heating modality of the system, which delivers >200mW of optical power from a fiber-coupled laser diode to a 3.7 μm radius spot on the sample. Selected thermal pathways can be accessed via judicious choices of the laser power, pulse width, number of pulses, and radial position. Please note that the system produces a very small heated area on the sample, so fast temperature ramping is easy and multiple sites can be examined on the same sample. There is no thermal damage to detectors or the column, and thermal-mechanical drift in the sample is minimal, so it’s easy to perform long duration studies and acquire stop-go movies of processes on the atomic level.

Motivated by the desire to develop a commercially available and more ubiquitous system useful for a variety of optical in situ studies, Waviks Inc. has developed a new photon delivery system which can be mounted on any (S)TEM system. Fig. 2.1a and b are photographs of the system mounted on the Libra 200 (S)TEM. Fig. 2.1c is a computer-aided design schematic overview of the system with magnified images of the: Fig. 2.1d the lens assembly subsystem which houses the focusing optics that images the fiber optic ends; Fig. 2.1e the flange adaptor, in vacuo shaft carrying the fiber optics, and part of the x–y–z nanomanipulator; Fig. 2.1f the

protective shield for the individual fiber optics (3 shown in the diagram in purple) which are cabled and carried via a ~10m fiber optics to the control box which houses the laser/light sources and electronic drivers (not shown). Fig. 2.1g is a screen shot of the Waviks Inc. software which interfaces with the nanomanipulator and the laser drivers. This system has been adapted from a system previously developed for the dual scanning electron and ion microscope,[85] and used for in situ laser-assisted nanoscale electron[86-88] and ion[89-91] beam synthesis.

The alpha prototype used in these experiments contains two optical delivery channels/fibers. Peak powers up to >200mW are delivered to the sample from a 785 nm wavelength laser diode system coupled through a 5 μm mode field diameter single-mode fiber. The laser is gated by a software-controlled pulse generator that can vary the laser pulse width from a few nanoseconds to continuous wave (cw) at repetition rates up to 16 MHz. A second optical channel, containing a 100 μm core diameter broad spectrum multimode fiber, is available for coupling to any excitation source in the wavelength range from 200 to 2,100 nm using a standard subminiature assembly fiber connector. The system is mounted to a 3 axis (± x, y, z) nanomanipulator for easy focusing to the electron/sample coincident point (with sample tilted at ~45°) and uses a lens system to re-image the fiber optics (1 × magnification) at a working distance of ~10 mm. The working distance is sufficiently long so as to not introduce any charging artifacts when the optical probe is inserted and aligned and minimizes redeposition of material onto the lens system. The current system is installed on the energy-dispersive X-ray analysis port, which is perpendicular to the sample entry and provides convenient access to the sample via simply tilting the stage. Future options under development include co-mounting the system with the aperture strip or integrating the system with the sample entry/manipulation system.

Fig. 2.2a schematically illustrates the end of the optical probe in proximity (~1 cm) to the TEM substrate and Fig. 2.2b is a schematic illustrating that a vast array of thermal pathways can be achieved via different combinations of laser power,

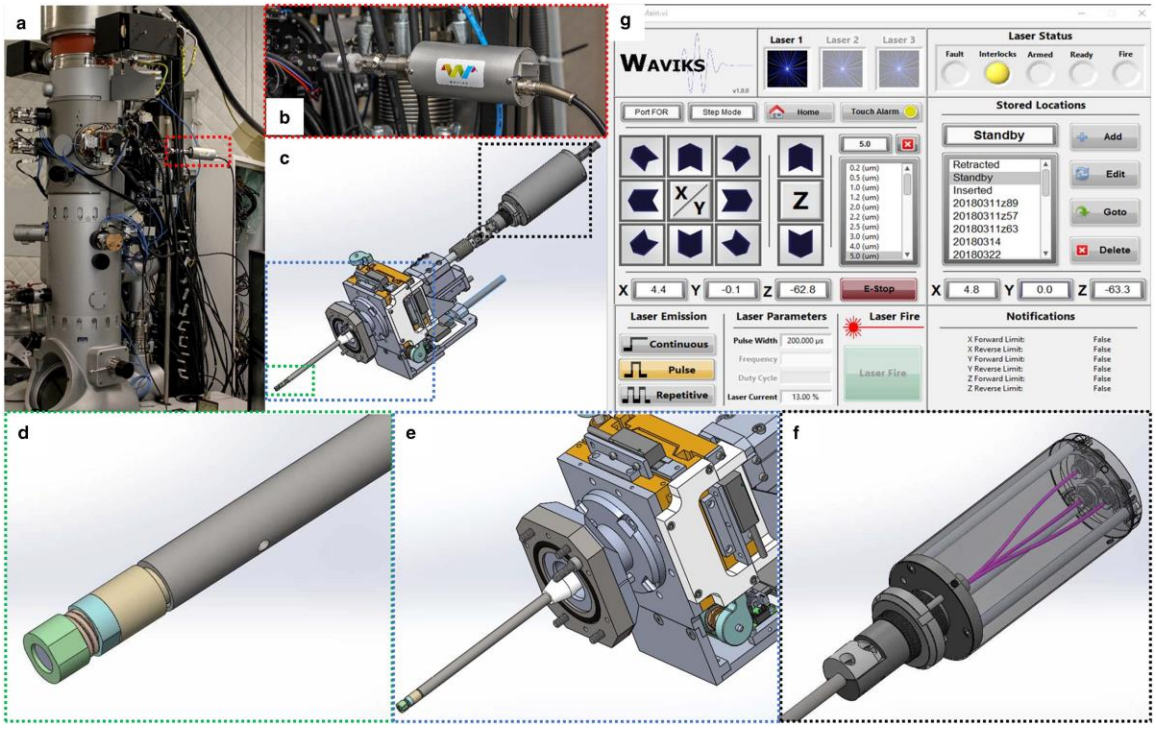

Fig. 2.1 (a, b) Photographs of the optical delivery system mounted onto the Libra 200 (scanning) transmission electron microscopy. (c) An overview computer-aided design schematic of the system with magnified views of the (d) lens assembly end piece, (e) vacuum mounting flange and in vacuo shaft which carries the optical fiber and part of the x–y–z nanomanipulator, and (f) protective shielding for the fiber optics which are cabled and carried to the control box which houses the laser/light sources and electronic driving units (not shown). (g) A screen shot of the Waviks Inc. software which controls the nanomanipulator and laser drivers.

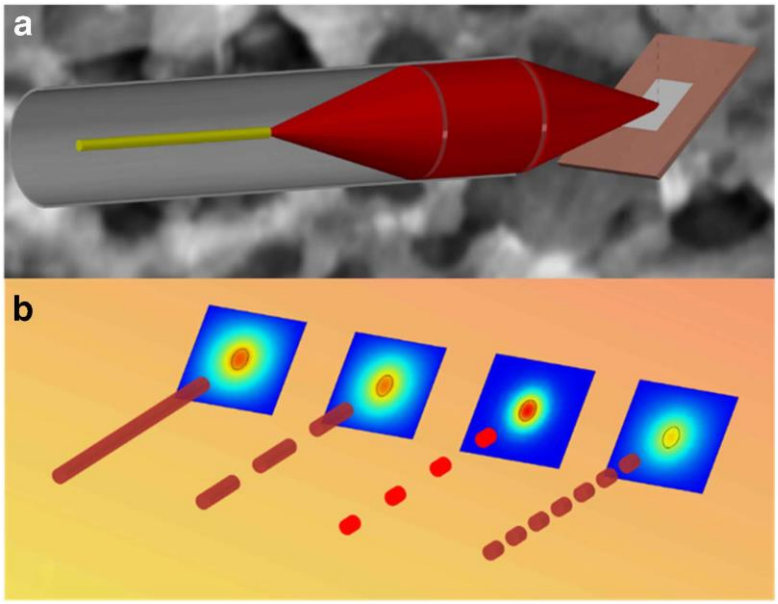

Fig. 2.2 (a) Schematic illustrating the end of the optical delivery system which re-images a laser-coupled single mode fiber optical fiber onto the transmission electron microscopy sample. b: Schematic illustrating that various laser conditions can generate numerous in situ photothermal pathways via different combinations of laser power (up to 215 mW), pulse width (1 ns to CW), number of pulses and radial position.

pulse width, number of pulses, and radial position. For instance, from left to right we can run the laser cw, and various pulse widths (>1 ns), and various power densities (up to ~500 kW/cm^2).

2.2 Methods for synthesis of Van der Waals bilayer

2.2.1 Sample Preparation.

The a-WSe_2 precursor was deposited directly to holey silicon nitride TEM grids by PLD. The holey silicon nitride (SiN_x) has 2.5µm holes with a 4.5µm pitch in 200nm Si_3N_4 over a 0.5 × 0.5mm window size. The grids covered with graphene are commercial single-layer graphene samples (Ted Pella Inc., Redding/CA 21712-5 PELCO) grown with chemical vapor deposition (CVD). The grids support $MoSe_2$ are holey SiN_x grids (Ted Pella Inc., Redding/CA 21535-10 PELCO). The 1L $MoSe_2$ domain with 30 μm of the edge length was also grown by CVD and was transferred to the holey SiN_x grid using poly (methyl methacrylate) (PMMA). A pulsed KrF (248 nm, 25ns FWHM, 1-50 Hz repetition rate) laser was used for the ablation of the targets in vacuum and argon background gas. A 1 in.-diameter WSe_2 pellet (Testbourne Ltd, 99.9% purity) was used as the ablation target. Using a projection beamline, an aperture was imaged onto the target to produce a 1.3 mm x 4.5 mm rectangular spot. 40 mJ of laser energy was used, providing ~ 0.8 J/cm^2 per laser pulse at the target surface. SiO_2/Si substrates (typical size 1cm x1cm) were adhered onto a 1 in. diameter heater (HeatWave Laboratories, Inc.) with a thin conductive silver paint. SiN_x TEM grids used for STEM measurements were attached to the substrates using tiny droplets of a silver paint. The substrate was placed 5 cm away from the WSe_2 target in a cylindrical stainless-steel chamber (50 cm inner diameter, 36 cm tall). The heater temperature was controlled to ± 2 °C via a PID controller, and ramp up and cooling rates were 30 ℃/min. The growth was performed at 600 ℃ at a base pressure of 5.0 × 10^{-6} Torr. The amorphous precursor for laser synthesis was deposited at room temperature.

2.2.2 *In situ* TEM observation with laser irradiation.

High-resolution transmission electron microscopy (HRTEM), selected-area electron diffraction (SAED) and electron energy loss spectroscopy (EELS) were conducted using a ZEISS LIBRA 200MC TEM operated at 200 kV. *In situ* HRTEM images and SAED patterns are acquired with the irradiation of laser. The details of the laser system were provided in section 2.1. A laser width of 10 ms and a frequency of 0.5 Hz was used to ensure the stability of the movie during laser irradiation. As for the detailed dynamic evolution, a laser with 300 μs and 0.5Hz was used because the final temperature of the material is only just reached within this pulse width (no dwell time). In such circumstance, the evolution of microstructure changes slowly after each laser pulse and the drift of sample during acquisition is small. To ensure that microstructure has reached the stable structure, 5 laser pulses (10 s) was implemented at each energy before increasing laser energy. Each *in situ* laser irradiation experiment was repeated at least twice to confirm the structure change.

For the core-loss EELS acquisition, the electron beam was blanked during the laser irradiation to minimize beam effects on the sample. The EELS data was acquired with laser beam kept off after certain power of laser was performed. All core-loss EELS spectra were quantitatively analyzed using the Quantifit software.[92] The post-growth high-angle annular dark-field scanning transmission electron microscopy (HAADF-STEM) characterization and *in situ* STEM heating experiment was conducted using a Nion Ultra STEM 200 microscope operated at 100 kV. The TEM grids were baked at 160 °C for 8 h in HV before putting in the microscope chamber in order to remove the adsorbents left by sample handling. HRTEM images shown in the figures were Fourier filtered to remove high frequency noise.

2.2.3 First-principles density functional theory calculations.

All the calculations were performed using the all-electron, numeric atom-centered orbital code FHI-aims.[93] We employed “tight” basis and Perdew-Burke-Ernzerhof (PBE) functional[94] with vdW functional of Tkatchenko and Scheffler[95] in the exchange-correlation functional, which accurately captures the long-range interaction between the layers. We used experimental lattice constants to construct the flakes of $MoSe_2$, WSe_2, and Gr. The optimum distance between WSe_2 and the substrates ($MoSe_2$ and Gr) were determined by interoperating the total energies calculated for different distance between WSe_2 and substrates. We thank Mina Yoon for providing us these calculations.

2.3 Methods for synthesis of Janus WSSe

2.3.1 Pulsed Laser Deposition of Se and *in Situ* Diagnostics.

A pulsed KrF (248 nm, 25ns FWHM, 1-5 Hz repetition rate) laser was used for the ablation of the targets in vacuum and argon background gas. A 1 in.-diameter selenium pellet (Plasmaterials, Inc., 99.99% purity) was used as the ablation target. Using a projection beamline, an aperture was imaged from an aperture onto the target to produce a 1.25 mm x 4.5 mm rectangular spot. Typically, 57 mJ of energy was used, providing 1.0 J/cm^2 per laser pulse at the target surface. WS_2 monolayer crystals grown by CVD on SiO_2/Si substrates were mounted on a 1 in. diameter heater (HeatWave Laboratories, Inc.) placed d = 10 cm away from the Se target in a cylindrical stainless-steel chamber (50 cm inner diameter, 36 cm tall). The heater temperature was controlled to ± 2 °C *via* a PID controller, and ramp-rates were typically 30 ^{o}C/min. The gas pressure was controlled with a mass flow controller (Ar 99.995%, 10 standard cubic centimeters per minute (sccm)) and a downstream throttle valve.

Imaging of the visible luminescence of the plasma plume (or laser-induced fluorescence (LIF)) was performed with a gated-ICCD camera (Princeton

Instruments ST-130) with variable gate width (5 ns minimum). The camera was triggered by a digital delay generator (SRS DG 545) which was triggered by a fast photodiode at the exit of the KrF laser. The camera lens (Nikon, f4.5) was positioned 46 cm away from the center of the plume, outside the chamber and through a 2 in x 8 in fused silica (Suprasil) window. In low-light situations, the exposure time was typically set to 10% of the delay time. Ion probe current waveforms (-40 V floating bias supplied by a battery and 1 μF decoupling capacitor, detector area ~ 1 mm^2) were recorded by a digitizing oscilloscope (LeCroy WaveJet 354T) using 1 or 5 kΩ input impedance.

Simultaneous spectroscopy also could be performed using a second gated, intensified CCD-array detector (PI-MAX 3, Princeton Instruments) that was coupled to a spectrometer (Spectra Pro 2300i, Acton, f = 0.3 m, 150, 600, and 1200 grooves/mm gratings). Light from the plume was collected using a 2-inch, f = 0.5 m lens outside the chamber, through a 2 in x 8 in fused silica (Suprasil) window located opposite the former window. Different collection positions could be chosen by sliding the spectrometer and lenses on a translation table. For the laser induced fluorescence (LIF) experiments, the third harmonic of a Nd:YAG laser (355 nm, 8 ns pulse width, 1 Hz repetition rate) was triggered (at a time delay selected on the delay generator relative to the KrF-laser ablation pulse) to irradiate the plume species at different distances from the target, and the spectroscopy CCD-detector could be gated to collect light during this pulse, or afterward, using the delay generator.

Transient deposition and desorption of Se species were detected on tailored SiO_2/Si substrates using a specularly-reflected HeNe laser beam which was passed through the windows of the chamber, through a 633nm filter, and onto a fast photodiode (Thorlabs SM1PD1A).[39] The transient decrease in reflectivity was recorded on a digitizing oscilloscope (LeCroy WaveJet 354T) to estimate the arrival and residence times at different temperatures and pressures.

2.3.2 Synthesis of WS_2 and MoS_2 monolayers.

CVD synthesis of WS_2 monolayers was performed using sulfur powder (Sigma-Aldrich) that was placed 20 cm upstream from the center heat zone where WO_3 (10 mg, 99.99%, Sigma-Aldrich) powder mixed with 3% of KCl powder (Sigma-Aldrich), by mass, was placed. SiO_2/Si substrates also were placed in the center of the 2 in. tube furnace, face down above the powders. A typical growth run was performed at 820°C-850 °C for 5 min under a flow of Ar gas at 60 sccm and ambient pressure. CVD MoS_2 monolayers, specifically, were grown using a mixture of MoO_3 (5 mg) and S powders at 750 °C for 4-6 min under a flow of Ar gas at 70 sccm and ambient pressure.

2.3.3 Sample preparation and HAADF STEM experiments for alloys monolayers on TEM grids.

A thin layer of poly(methyl methacrylate) (PMMA) was deposited onto a substrate with WS_2 monolayers in a spin-coater (500 rpm for 10 s and 3000 rpm for 50 s) and then left in a fume hood overnight to evaporate the solvent. The PMMA-coated monolayers on SiO_2/Si substrate were placed in a Petri dish filled with KOH solution (30 wt%, 90 °C) to dissolve the substrate, leaving a PMMA/WS_2 membrane. The membrane was transferred onto a SiN_x grid (Ted Pella) with 2.5 μm holes, and then washed in acetone and isopropyl alcohol to remove the PMMA. Prior to electron microscopy experiments, the samples were directly implanted and selenized on TEM grids in the PLD chamber. The TEM grids were baked at 160 °C overnight in vacuum before STEM measurements to remove residual hydrocarbons.

The HAADF Z-contrast STEM characterization was conducted in a Nion Ultra STEM 200 microscope with sub-angstrom resolution operated at 100 kV. The STEM-ADF image simulation for the normal and tilted views of an ideal Janus WSSe ML was performed using the QSTEM simulation package.[96] WSSe Janus ML model consists 10×10×1 unit cells. The probe array was 400×400 pixels with

a resolution of 0.05 Å. The high voltage was 100 kV, convergence angle was 30 mrad, the brightness was 5×10^{8} $Acm^{-2}sr^{-1}$, temperature was 300 K, and the detector geometry was 70 to 200 mrad. For normal view image simulation, the sample tilt angle was 0°, while for tilted view image simulation, the sample tilt was set to x = +15° and y= +15°.

2.3.4 Analysis of HAADF STEM images

Stacks of images were registered first registered rigidly and then with a Diffeomorphic Demon Non-Rigid Registration as provided by the simpleITK package.[97] These registered images of a stack were summed along the time axi s resulting in images with high signal noise ratio. We also used single images again with high spatial resolution and high contrast. The atom positions were determined with a two-step process in which first, the most common blob detection based on the Lapalacian of Gaussian (implemented in the scipy package) was performed. Any atom detection algorithm will lead to the same result as the blob detector for such high contrast images. Then a Gaussian was fitted to each blob to obtain sub-pixel precision in atom position. An affine distorted lattice was fitted to the W atom sites and the rough position of the chalcogenide site was determined by a shift of the W-atoms lattice. The chalcogenide atom positions were further refined by determination of the position centered in the middle of the three nearest neighbor W atoms, to observe local distortions. The atom positions were used to sum over the same-sized circular area around an atom position separately for the two different sublattices. The intensity-histograms of the two sublattices can then be plotted independently. This approach makes it possible to detect vacancy and low intensity atom sites, even though no atomic column is visible in the image.

2.4 Methods for characterization of plasmons

2.4.1 Sample Preparation.

An ~25 nm silver film was RF magnetron sputter deposited directly onto 20 nm SiO_2 membranes (TEMwindows.com, a division of SiMPore Inc., Rochester, New York.). The silver film was sputtered at: 20 W RF power, 25 standard cubic cm per minute Ar flow, and 5 mTorr chamber pressure.

2.4.2 TEM experiment

The TEM coupled with the optical system used in this section is the same as described in section 2.1. During low-loss EELS acquisition, the TEM was operated at 200 kV in (S)TEM mode with a camera length of 945 mm. The collection semi-angle (β) was 45 mrad, and the convergence semi-angle (α) was 10 mrad. The low loss spectra were collected with a monochromator slit of 0.5 μm, and a dispersion of 30 meV per channel was chosen for the spectrometer acquisition. The average energy resolution (defined as the full width at half maximum of the zero-loss peak) was measured to be 136 meV for a summed spectrum; the energy spread for all single and summed spectra collected was between 120 and 150 meV. For each low-loss point spectrum, 10 frames with a dwell time of 0.1 s each were summed up to yield high count values and signal-to-noise ratios. The average energy resolution (defined as the full width at half maximum of the zero-loss peak) was measured to be 136 meV. For the EELS map acquisition, a region of interest with 20 × 13 pixel spectra (1 pixel ~19.5 nm × 19.5 nm) is defined over the entire silver nanoparticle. The pixel dwell time for each pixel in the EEL maps is 0.3 s. The maps of the sEEG (–1.58 eV), sEEL (1.58eV), 1.21 eV dipole mode, and the 2.3 eV quadrupole mode are generated using the Gatan Digital Micrograph software by plotting spectra intensity in designated energy slices within the 3D spectrum image data cube (x, y, energy-loss).

2.4.3 Linear least-square fit of EELS spectra

In order to quantify position and scattering probability of the EEGS and EELS peaks, we fit a model to the unprocessed experimental spectrum. We used the linear least-square fitting routine of scipy to find the best fit with a python program realized in a jupyter notebook [30, 92]. The static webpage of the jupyter notebook analyzing the spectrum in series A with laser irradiance of 2.2×10^8 W/m^2 was converted to PDF and attached in the end of this supporting information. Before fitting, the zero-loss peak was shifted to zero eV to ensure the exact positions of the plasmon, EEGS and SEELS peaks in the spectra. Sub-pixel determination of the origin was established by fitting a Gaussian to the zero-loss peak. Then the intensities of all the peaks in the EEL spectra were normalized within an energy window from -6 eV to 56 eV. The zero-loss peak was fitted by a product of two Lorentzian peaks. After subtracting the zero-loss peak, we modeled the spectrum of the un-irradiated sample by a combination of several Gaussians. Please note that we fit the whole low-loss spectrum with the minimum number of peaks for a good fit. A fit was considered acceptable when the difference between experimental spectra and reconstructed spectra was close to the noise level (< 2 times the standard deviation).

The large broad peak in the EELS spectrum at 18 eV originates from the bulk plasmon of SiO_2 substrate and carbon contamination. Inter-band transitions of SiO_2 start at 9.5 eV[3] and of silver at 10 eV[4]. Therefore, all peaks between 1 and 9 eV originate from surface plasmons. The broad plasmon peak at around 5 eV is from the carbon contamination and may contain a weak contribution of the SiO_2 surface plasmon which is at about the same energy (5.5 eV).[98] Since the shape of the particles is very complicated, it is hard to assign the multipole characteristic of each plasmon peak. This is however the strength of the EEGS as only dipole plasmons will produce a strong gain peak and thus the method can be used to differentiate the dipole from other multipole plasmons. Noteworthy, the extra peaks around the zero loss (-0.7 to 0.7 eV) are due to the broadening of the zero-loss

peak by phonon interaction and spectrometer aberrations. The phonon influence on the peak at 0.7 eV is especially strong as can be derived from the increased intensity at higher temperatures. For spectra recorded while exposed to the laser irradiation, we had to add two peaks with the same shape as the zero-loss peak at about -1.58 eV and 1.58 eV for the EEG and SEEL, respectively. Then by linear least-square fitting, 10 % change of position and FWHM (full width at half maximum) with respect to the un-irradiated case was allowed for the plasmon peaks. The amplitude of the plasmon peaks and all the fitting parameters of the peaks representing substrate and carbon contamination were unrestricted. However, on spectra series A in Fig. 4.3, the broadening of the zero-loss peak and the plasmon peak right under the SEEL peak at about 1.58 eV allows for multiple representations of that energy-interval. Therefore, the amplitude of plasmons at 1.06 eV and 1.5 eV were restricted within 10 % of the spectrum of the un-irradiated sample. For the high laser irradiance spectra where the EEG and SEEL peaks notably decrease, no variables were restricted. It is noted that position and amplitude of the EEG and SEEL peaks were nearly the same regardless of whether the variables were restricted or not.

2.5 Temperature estimation

The temperature increased during laser illumination is also an important parameter. One way to estimate the temperatures is using finite element simulations on COMSOL software, as described in section 2.5.1. Another way is to use the peak shifts of excitons induced by increased temperature measured by EELS, as discussed in section 2.5.2.

2.5.1 Temperature estimation by laser heating simulations

The temperatures presented in what follows are estimated by finite element simulations as described below. The simulation was performed by Michael G. Stanford. The simulations assume a continuous uniform film with the relevant parameters and assumptions listed below. Importantly, the simulations are valid

for the continuous film and will change when dewetting occurs, as the incident angle and thickness will change, as will the thermal conduction, which for the continuous film dominates via the $Ag_{0.5}Ni_{0.5}$ film and for isolated islands and particles is limited by conduction through the SiO_2 membrane. High-resolution pyrometry and/or patterned thermistors are planned in the future. Importantly, while the laser power is sufficient to significantly photothermally heat on thin membranes due to the limited thermal conduction in effectively the radial direction, the overall power is low and thus it is easily dissipated in the surrounding silicon substrate.

Simulations of laser-induced heating of the $Ag_{0.5}Ni_{0.5}/SiO_2$ membrane were performed using COMSOL Multiphysics 5.0 a commercial finite element method software package. The simulation used a thickness of 20nm for AgNi and the SiO_2 membranes. The membranes were 50 × 50 μm in length and anchored onto a Si heat sink, to emulate the geometry of TEM membranes. The expression for heat delivered to the substrate from the laser is derived from the Beer–Lambert law:

$$Q_{in}(x,y,z) = P_o(1-R_c)\frac{2A_c}{\pi w_x w_y}G(x,y)exp(-A_c z)\ , \qquad (2.1)$$

where P_0 is the optical power of the laser, R the reflection coefficient, A the linear attenuation or absorption coefficient, G(x,y) the Gaussian laser irradiance profile, w_x and w_y the $1/e^2$ irradiance radii of the Gaussian laser profile in the x and y directions, respectively, and z the depth from the substrate's surface. w_x and w_y were experimentally determined to be 3.7 and 5.2 μm, respectively, as described above. A linear 10 ns laser ramp time was assumed for this simulation and the laser pulse width was 200 μs. All absorption was assumed to occur in the $Ag_{0.5}Ni_{0.5}$ film, since the extinction coefficient for 785nm photons in SiO_2 is ~0. The following time dependent heat equation was used to simulate the heat transfer throughout the $Ag_{0.5}Ni_{0.5}$ and SiO_2 membranes, as well as the silicon heat sink:

$$\rho C_p \frac{dT}{dt} + \rho C_p \boldsymbol{u}\cdot\nabla T = \nabla\cdot(k\nabla T) + Q(x,y,z) \qquad (2.2)$$

where ρ is the material density, C_p the heat capacity at constant pressure, **u** the velocity vector for thermal transport, and κ the thermal conductivity. Convective heat transfer to the surrounding atmosphere was neglected since irradiation conditions were under high vacuum and T_0 was defined as 293.15 K. Notably we have ignored radiative heat loss in the simulation where including radiative heat loss would lower the simulated temperatures and have a more pronounced effect on higher temperature simulations. A backward differentiation formula time-stepping method with strict time steps was used to generate the temporal temperature evolution during laser irradiation.

Table 2.1 reports relevant simulation and material parameters used to simulate the temperature temporal evolution induced by the 785nm laser pulse. The $Ag_{0.5}Ni_{0.5}$ and SiO_2 heat capacitance and thermal conductivity were approximated for thin films in accordance to the Refs[99-101]. For the $Ag_{0.5}Ni_{0.5}$ film, heat capacities and densities were averaged for each element to estimate the values for the alloy. The thermal conductivity was estimated based on the literature, which suggests that Ni thermal conductivity is independent of thickness,[99] and at 20 nm, Au thermal conductivity will be ~20% of the bulk value,[100] which is applied to the Ag bulk value.

As the laser irradiation profile on the sample is approximately Gaussian and the confined thickness limits thermal diffusion to the radial direction, the time-temperature profile varies with radius. Fig. 2.3a is a plot of the simulated temperature as a function of radius at various times and Fig. 2.3b is a two-dimensional temperature map of the surface temperature at 200 μs for a 200 μs and 36.5mW pulse. The temperature map exhibits the elliptical irradiation profile on the sample surface caused by the ~45° sample tilt with respect to the incident laser beam (see Fig. 2.2a).

Table 2.1 Material and laser parameters for the thermal simulations.

Simulation Parameters	Value	Description
w_x	3.7 [µm]	Laser $1/e^2$ irradiance radius - *x*
w_y	5.2 [µm]	Laser $1/e^2$ irradiance radius - *y*
R	0.69	Reflection coefficient of AgNi at 785 nm
A	5.52E5 [1/cm]	Absorption coefficient of AgNi at 785 nm
P_0	12.8-22.2 [mW]	Laser power
Pulse	200 [µs]	Laser pulse width
C_p(AgNi)	340 [J/(kg*K)]	AgNi heat capacity
ρ(AgNi)	9700 [kg/m^3]	AgNi density
κ(AgNi)	88 [W/(m*K)]	AgNi thermal conductivity
C_p(SiO_2)	710 [J/(kg*K)]	SiO_2 heat capacity
ρ(SiO_2)	3440 [kg/m^3]	SiO_2 density
κ(SiO_2)	1.0 [W/(m*K)]	SiO_2 thermal conductivity

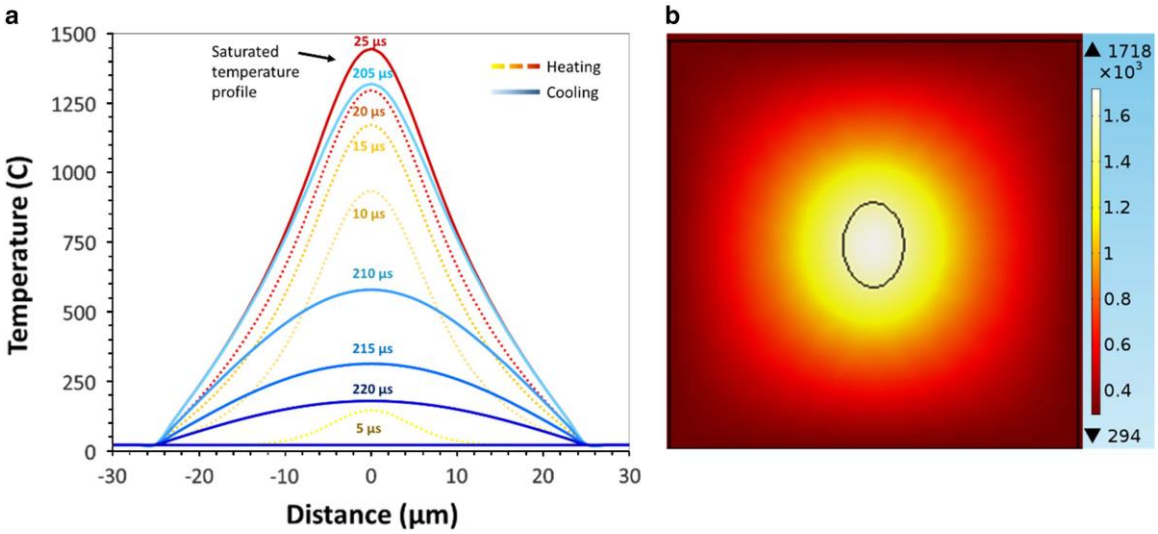

Fig. 2.3 (a) Simulated surface temperature versus position for various times illustrating the spatial and temporal temperature evolution for a 36.5 mW power and 200 µs pulse width (b) two-dimensional plot of the surface temperature at 200 µs for the 36.5mW power.

2.5.2 Temperature estimation by temperature-dependent excitonic effects

The force-field simulations are frequently employed to predict the temperature rises in constructed model systems under laser irradiation[102]. However, we take a direct experimental approach to estimate the temperature raised in the suspended 1L $MoSe_2$ crystals based on the temperature-dependent excitonic effects in the optical properties of 2D semiconductors[103-106]. We irradiated a bare suspended 1L $MoSe_2$ on the holey SiN_x TEM grid and performed *in-situ* EEL experiments at cryogenic temperatures to obtain its low-loss EELS spectra for increasing laser powers (Fig. 2.4a). The peaks in the EEL spectra were fitted by linear least-squares fitting[107]. The redshift of the A and B excitonic peaks of the suspended bare 1L $MoSe_2$ was observed. The peak widths also broadened due to enhanced electron-phonon interaction with increasing laser powers. This trend has also been observed on the thermally annealed suspended 1L $MoSe_2$[104-106].

In Fig. 2.4b, the redshifted peak position of the exciton A is plotted as a function of increasing laser powers. The excitonic position was red-shifted inversely proportional to increasing laser power. Similarly, several works have shown that the peak redshift has an inverse linear relationship with increasing temperatures[105, 106, 108]. With this understanding, we correlated laser powers with the temperature through the redshifted exciton peak position using the vibronic model[109] describing temperature dependence of semiconductor gaps that has been used for 2D $MoSe_2$[105, 108];

$$E_g(T) = E_g(0) - S < hv > [\coth(< hv >/2k_BT) - 1]$$

, where $E_g(0)$, S, $< hv >$, and the $\coth$ term represent the bandgap of $MoSe_2$ at 0 K, a dimensionless electron-phonon coupling parameter, the average acoustic phonon energy, and the density of phonons at a particular temperature. The values of these parameter adopted from Tongay *et al*.[105] were fitted into the linear plot of peak position *vs.* temperature in Fig. 2.4b. Although the low-loss EELS was acquired at cryogenic temperatures, since the linear relationship holds from liquid

nitrogen temperature to 800K[104, 105], we set room temperature (25°C) as the starting temperature at 0 mW laser irradiation to make it consistent with our *in situ* laser experiments. Therefore, the laser power can be correlated with temperature directly as shown in Fig. 2.4b. For example, laser power of 8 mW can raise the temperature of a suspended 1L $MoSe_2$ to near 160 °C. And 15 mW and 20 mW can raise the temperature to 280 °C and 360 °C, respectively.

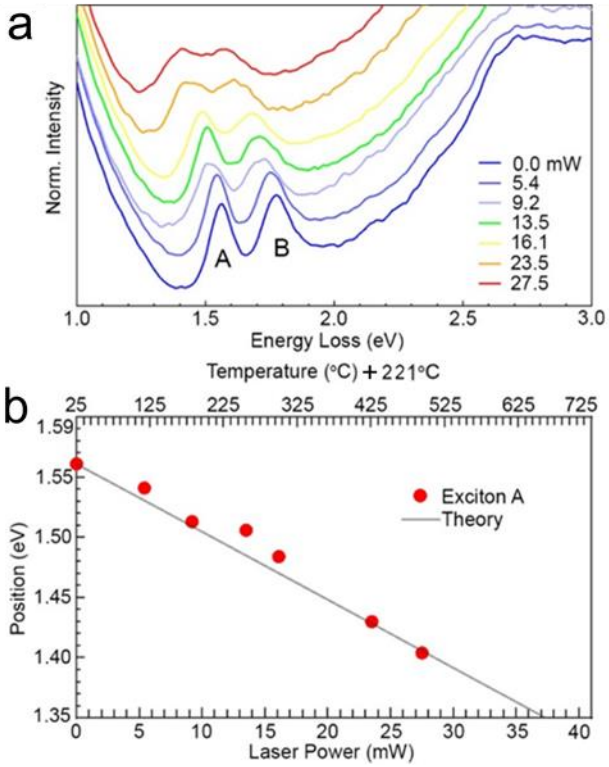

Fig. 2.4 Laser power dependence of EEL spectra measured for suspended 1L $MoSe_2$ on holey SiN_x grid at 77 K in cryo-TEM holder within a Libra 200MC with energy resolution of 0.14 eV. (a) Excitonic band-shifts of $MoSe_2$ for different laser powers (illuminating tilted 5-mm spot). (b) Laser intensity dependence of the peak positions of exciton A and correlation of temperature with laser power, where the temperature scale has been adjusted for comparison with the *in situ* laser heating of room temperature (298 K) substrates in our experiments by +221°C (= 298 K – 77 K).

Chapter 3. Synthesis of Van der Waals bilayer by *in situ* laser-induced heating

In the chapter, we investigate how amorphous precursors of tungsten selenide that are deposited by PLD assemble to form well-aligned 2D heterostructures when guided by vdW epitaxy from other 2D monolayer (ML) crystals. This vdW epitaxy is demonstrated first in direct PLD experiments using ML Gr and $MoSe_2$ substrates held at 600 °C, where lattice matching between WSe_2 and $MoSe_2$ is found to form well-aligned 2D $WSe_2/MoSe_2$ heterostructures, while the poor lattice match between WSe_2 and Gr produces polycrystalline, misaligned WSe_2/Gr heterostructures. To gain some insight on the mechanisms of alignment and assembly responsible for this vdW epitaxy we deposit the same quantity of amorphous precursor clusters by PLD onto these substrates at room temperature (RT), then employ pulsed laser heating within a transmission electron microscope (TEM). Using *in situ* high-resolution TEM (HRTEM) imaging, selected area electron diffraction (SAED) and electron energy loss spectroscopy (EELS) we characterize the structure, crystallinity, alignment, and temperature as the precursor species crystallize and assemble into 2D crystalline domains.

These *in situ* HRTEM and SAED measurements reveal that the nanoscale grains can assemble and coalesce into larger grains by non-classical crystallization pathways involving a variety of particle attachment processes, including grain rotation and grain boundary migration. Density functional theory (DFT) calculations reveal that nanoscale domain rotation is guided by the energetic favorability of alignment with the substrate. These *in situ* laser heating methods to stepwise evolve PLD-deposited precursors toward vdW-aligned heterostructures reveals processes that are likely undergone over much more rapid timescales during growth under actual PLD conditions. The results are directly applicable and point the way to optimize the growth of 2D TMD vdW heterostructures by laser or pulsed thermal processing of pre-deposited precursors through the use of domain matched substrates.

3.1 Substrate-guided synthesis of vdW heterostructures in PLD

First we explored the PLD of ~ 1L WSe_2 layers on both suspended and supported $MoSe_2$ (lattice-matched) and Gr (lattice-mismatched) substrates to form vdW heterostructures, following techniques we previously developed for the *in situ* optical reflectivity controlled growth of ML $MoSe_2$ layers.[110] Fig. 3.1a, b show the experimental arrangement. Monolayer Gr and $MoSe_2$ crystals were mounted as substrates across the 2.5 μm imaging windows on holey silicon nitride (SiN_x) TEM grids that were attached to a resistive heater in the PLD chamber. When the temperature of both TEM grids reached 600 °C, 20 pulses from a KrF-laser firing at 1 Hz were used to ablate a WSe_2 target 5-cm away to supply plasma plumes for the growth of 1L WSe_2 domains. Gated-ICCD photography of the plasma plume emission as shown in Fig. 3.1a and b was used to measure the propagation of the WSe_2 plasma plume through vacuum, as well as 50 mTorr Ar, and 200 mTorr Ar background pressures (see Fig. 3.2 for analysis). As shown in Fig. 3.1b and Fig. 3.2, scattering collisions with the background argon can be used to slow the fastest species arriving at the substrate position from a vacuum speed of 0.91 cm/μs in vacuum (corresponding to ~ 35.2 eV/Se-atom and 82 eV/W-atom), to 0.29 cm/μs in 50 mTorr Ar (~ 3.6 eV/Se-atom and 8.5 eV/W-atom), and 0.078 cm/μs in 200 mTorr Ar (~ 0.26 eV/Se-atom and 0.6 eV/W-atom). These background gas collisions not only slow the plume, but change its composition (shown below) by inducing gas-phase clustering, allowing the selective deposition (if desired) of ultrasmall amorphous nanoparticles in vacuum which we have shown can serve as the 'building blocks' for crystalline thin films and 2D materials.[3, 8, 37]

Despite this wide variability in the kinetic energy and size of the precursors delivered under these different PLD conditions, in each case we found crystalline WSe_2 layers on both substrates resulting in 2D vdW bilayer heterostructures (Fig. 3.3). Moreover, the lattice-matched $MoSe_2$ substrate was found to preferentially induce strong vdW epitaxial alignment of the WSe_2 monolayers. As shown in Figs. 1c-1d, Z-contrast high-angle annular dark-field scanning transmission electron

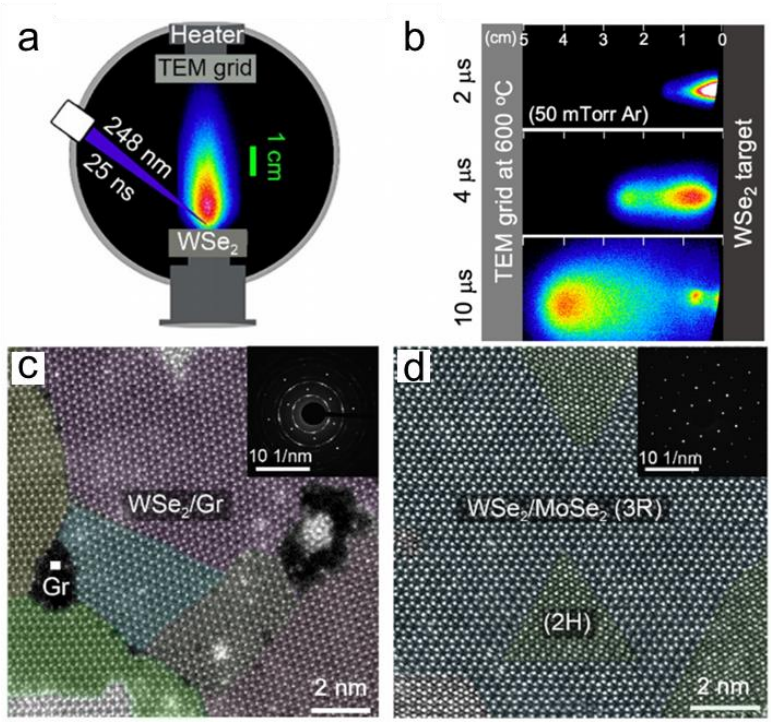

Fig. 3.1 Pulsed laser deposition of WSe_2 onto suspended graphene and $MoSe_2$ crystals. (a) Schematic of the experimental setup showing a TEM grid location inside the PLD chamber. Substrates of 1L Gr or $MoSe_2$ are suspended across 2.5 µm diameter holes on holey silicon nitride grids that are mounted on a resistive heater. (b) False-color gated ICCD images showing the laser generated plasma plume expansion in 50 mTorr (Ar) to the d = 5 cm grid position after KrF-laser (248 nm wavelength, 25 ns pulse width (FWHM), ~ 0.8 J/cm^2 energy fluence) ablation of a WSe_2 target. The visible plasma emission is shown at Δt (delay times) = 2, 4, and 10 µs (exposures are 10 % of the Δt for each image). (c), (d) False-colored HAADF-STEM image and SAED patterns (insets) of WSe_2 grown on a suspended 1L Gr showing its polycrystallinity and WSe_2 grown on a suspended 1L $MoSe_2$ forming epitaxial $WSe_2/MoSe_2$ bilayers, respectively.

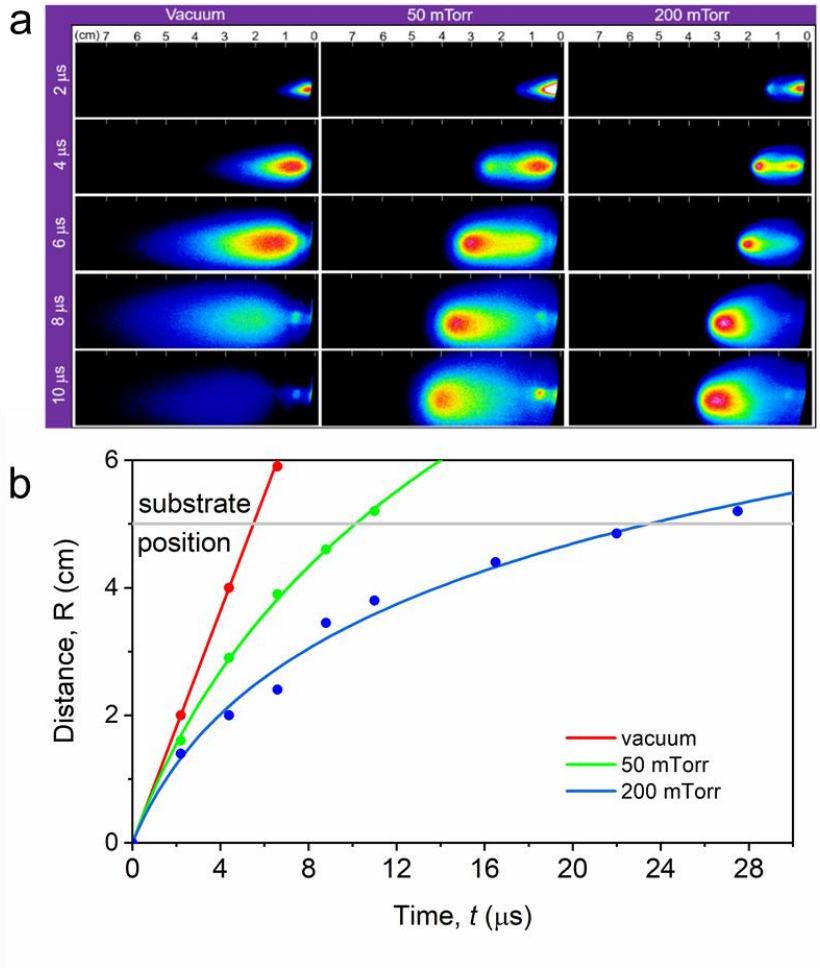

Fig. 3.2 (a) False color, gated-ICCD images of the visible luminescence of WSe_2 plasma reveal the propagation dynamics of the plume through vacuum, 50, and 200 mTorr argon background gas pressures at the indicated delay times following the laser pulse. (Gate width is 10% of each delay time) (b) R−t plots of the leading edge of the WSe_2 plasma track the propagation and deceleration in different background Ar pressures (vacuum, 50, and 200 mTorr). The propagation for each pressure is fit by the $a = -\alpha v^2$ drag model, where $R = \alpha^{-1}\ln(1 + \alpha v_o t)$ and $v = v_o(1 + \alpha v_o t)^{-1}$, from which the maximum WSe_2 kinetic energy/atom at the d = 5 cm substrate position could be adjusted. For all plots, v_o = 0.91 cm/μs. α = 0.233 and 0.486 cm^{-1} for Ar pressures of 50 and 200 mTorr, respectively

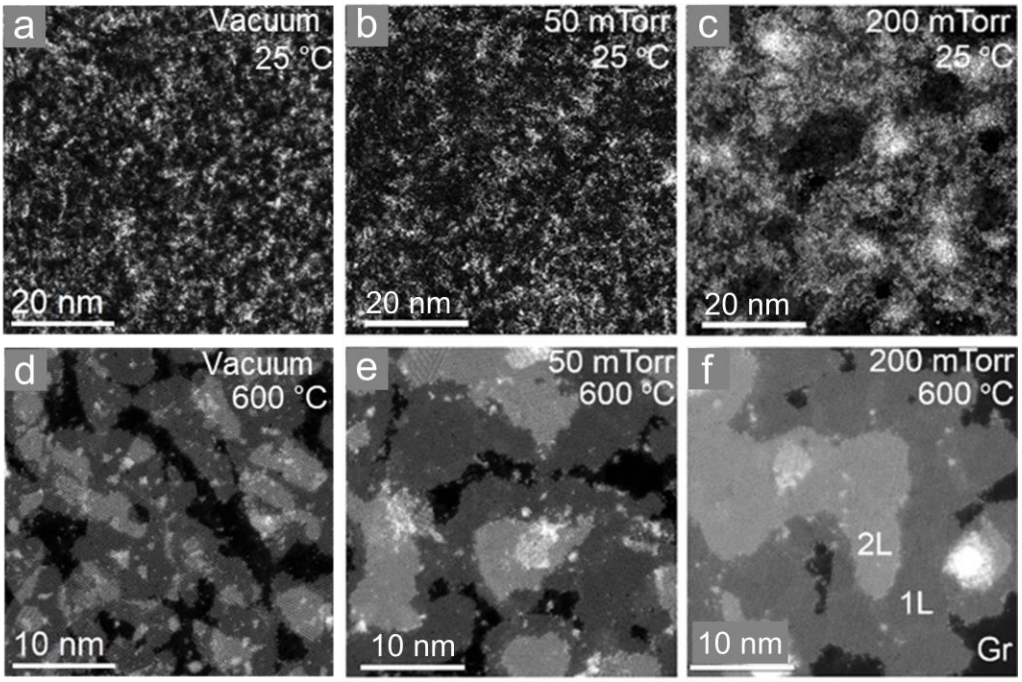

Fig. 3.3. (a-b) HAADF STEM images of amorphous tungsten selenide (a-WSe_x) deposited on graphene at 25 °C by PLD at 1 Hz (a) in vacuum (10-6 Torr), (b) at 50 mTorr in Ar, and (c) at 200 mTorr in Ar. The number of pulses is 10 for all three conditions; and HAADF STEM images of tungsten selenide deposited at 600 °C by PLD crystallized into 1L-2L WSe_2 domains at 1Hz (d) in vacuum, (e) at 50 mTorr Ar, and (f) at 200 mTorr Ar. The number of pulses is 25 for all three conditions.

microscopy (HAADF-STEM) characterization of the bilayer heterostructures show that 1L WSe_2 domains grown on 1L Gr are comprised of randomly oriented domains, as represented by different false colors in Fig. 3.1c as well as the SAED pattern (inset), which was obtained from a circular area with a diameter of 500 nm. On the other hand, 1L WSe_2 domains grown on 1L $MoSe_2$ display a single-crystalline SAED pattern shown in Fig. 3.1d and its inset. The two patterns shaded in false colors on the $WSe_2/MoSe_2$ bilayer in Fig. 3.1d denote the 2H- and 3R-stacking orientations found for this heterostructure. Since the deposition conditions on the different substrates were the same, the main factor leading to the improvements in crystalline alignment and grain size of WSe_2 on $MoSe_2$ *vs.* Gr substrates appears to be the small (0.4 %) lattice mismatch between 1L WSe_2 (3.297 Å) and 1L $MoSe_2$ (3.283 Å) and the large mismatch (25.8 %) with Gr (2.445 Å).[111, 112]

In order to understand the role of the lattice-matched substrate in guiding the assembly of PLD precursors, we first examined the precursors collected by PLD onto Gr substrates at RT for the three different PLD conditions. HAADF-STEM images of the amorphous precursors deposited at RT after 10 laser pulses are shown in Fig. 3.3 for vacuum, 50 mTorr Ar, and 200mTorr Ar, while the crystalline 2D WSe_2 films accumulated after 25 laser pulses (sufficient for near monolayer coverage)[110] at 600°C are shown in Fig. 3.3b. The amorphous precursors deposited in vacuum are seen to be molecular clusters and chains. Some of these may have formed from the aggregation of atoms and molecules deposited on the substrate, however a variety of small clusters are always expected from thermal desorption of chalcogens, and can be recognized as a slower-moving component of the laser ablation plume.[8, 35] Raising the background pressure from vacuum to 50 mTorr clearly increases the size of the clusters deposited on the substrate, indicative of their gas-phase formation process. Increasing the pressure to 200 mTorr results in non-uniform deposits consisting of agglomerated clusters and nanoparticles < 5 nm in diameter, which have been shown to form in the gas phase

and penetrate to longer ranges than atomic and molecular species.[37] Despite this variety in the amorphous precursor sizes, in all these cases PLD at 600 °C onto the same Gr substrates results in formation of crystalline domains of 1L and bilayer (2L) WSe_2 (Fig. 3.3b). Understanding how such non-uniform amorphous precursors crystallize and coalesce to form the uniform 2D layers shown in Fig. 3.1c, d requires a time-dependent investigation of these processes.

3.2 *In situ* laser crystallization of WSe_2 on graphene

3.2.1 In situ laser crystallization of PLD precursors

To understand this evolution from amorphous WSe_x to crystalline 2D WSe_2 on Gr and $MoSe_2$, a new approach of laser-induced crystallization in a specially configured HRTEM[102, 107] was developed as shown in Fig. 3.5. First, 40 pulses of amorphous precursors from the laser ablation of WSe_2 target in vacuum were collected on two separate holey silicon nitride (SiN_x) TEM grids (2.5 μm diameter grid holes) at RT with transferred 1L Gr or 1L $MoSe_2$ as substrates. The TEM grids with 2D substrates were first annealed at 300 ℃ for 90 minutes at 10^{-7} Torr to remove residual adsorbates and then cooled down to RT before PLD. HAADF-STEM images of ultra-thin WSe_x deposited on both Gr and $MoSe_2$ indicate that WSe_x is amorphous and comprised of monomers and clusters (Fig. 3.5a-b). Second, after PLD of amorphous WSe_x precursor (*a*-WSe_x), the TEM grids were moved into a HRTEM for *in situ* crystallization with a fiber-coupled laser diode coupled into the microscope's column and also for *in situ* imaging and electron spectroscopy characterization (Fig. 3.5c). [102, 107] The laser intensity is adjustable and can be triggered either in single ns-pulse, or multiple pulses at repetition rates as fast as 16 MHz in order to adjust the delivery of energy to explore crystallization pathways with digital precision in predetermined sequences. The laser beam is focused by nanomanipulating the fiber/lens within the column to illuminate a focused ellipse (a = 5.2 μm and b = 3.7 μm) spot and ~50 μm heat affected zone. The grid is tilted at α = 40° and the center of the laser spot is aligned to coincide

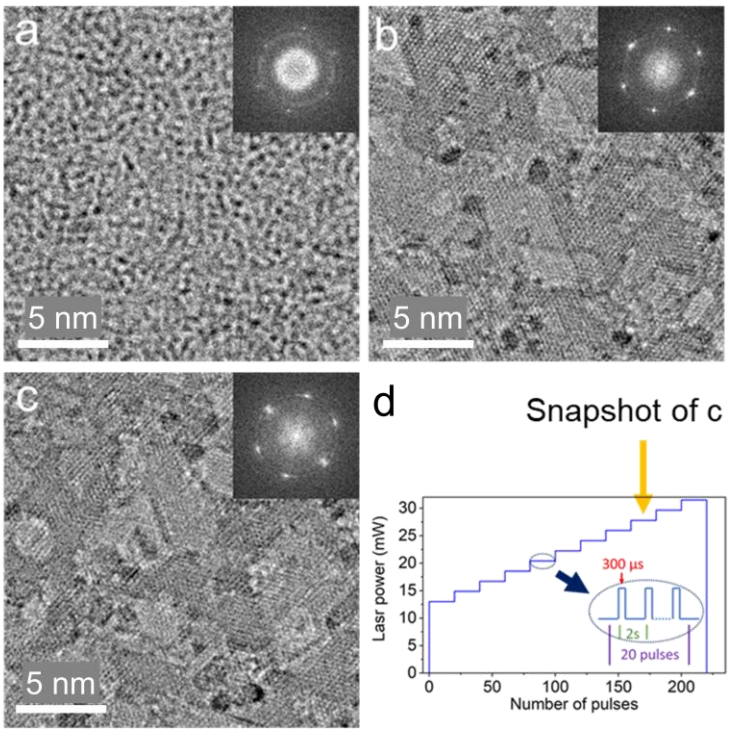

Fig. 3.4 Comparison of rapid synthesis and sequential processing of WSe_2 on monolayer $MoSe_2$ substrate showing that a single 300 µs duration pulse of high (28 mW) laser power induced the formation of 1L-2L crystalline films that were very similar in all respects to those that had been sequentially crystallized using many laser pulses where the power was slowly-increased in steps from low levels. (a) as deposited; (b) Rapid crystallization: a single 300 µs laser pulse at 28 mW; (c) Snapshot of sequential crystallizing processes at 28 mW with 300 ms laser pulse widths and 0.5 Hz frequency. The laser profile for the sequential crystallization is shown in (d).

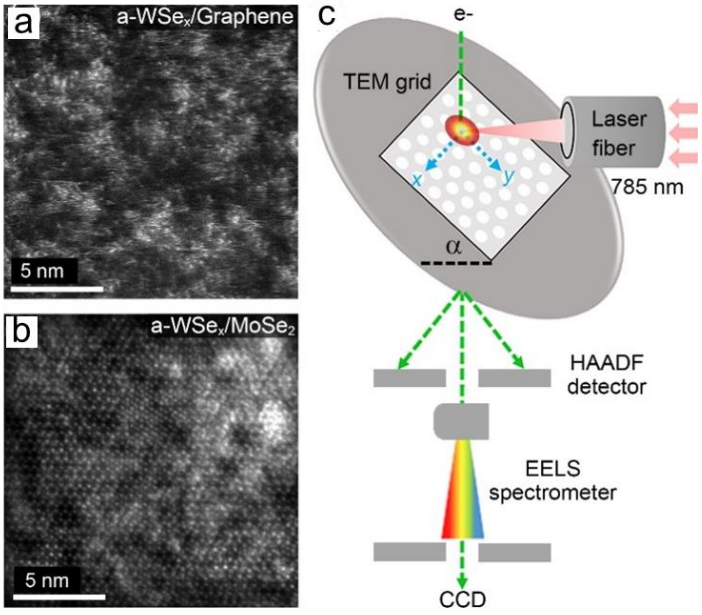

Fig. 3.5 Setup for the laser crystallization experiments within a TEM. (a-b) HAADF-STEM images showing the WSe_x precursors deposited from 40 PLD shots from a WSe_2 target in vacuum onto 1L Gr (a) and $MoSe_2$ (b) crystals transferred onto holey silicon nitride grids. The precursors are amorphous, consist of enough material to form a continuous monolayer, and are comprised of atomic clusters and chains. The underlying crystalline $MoSe_2$ substrate is evident in (b). (c) Illustration of the *in situ* observation arrangement within the HRTEM incorporating laser processing. The grid is tilted at $\alpha = 40°$, a 785-nm fiber laser is focused to an ellipse (a = 5.2 µm and b = 3.7 µm) onto the silicon nitride grid and exposed crystal, and the electron beam is available for EELS, SAED, or HAADF imaging.

with the electron beam observation position. While *a*-WSe_x precursors absorb some energy from the laser with 785 nm wavelength, the great majority of the heat in these experiments is deposited into the 200-nm thick SiN_x grids onto which the $MoSe_2$ or Gr substrates were mounted.

Given sufficient energy, it was found that crystallization could occur very rapidly. For example, a single laser pulse with 300-microsecond (μs) duration using 28 mW laser power (see Fig. 3.4a- b) induced the formation of 1L-2L crystalline films that were very similar in all respects to those that were sequentially crystallized using sequential laser pulses with increasing laser power (see Fig. 3.4c-d). Since the EELS temperature measurements were performed using continuous laser power, we selected laser pulse widths of 10 ms duration for the sequential crystallization experiments to ensure that temperature stability was achieved and maintained throughout the great majority of the laser pulse.

3.2.2 The Evolution of Structure and Stoichiometry During Crystallization of WSe_x on Gr

The stepwise evolution of an a-WSe_x/Gr film to a crystalline 2D heterostructure, and then a dewetted phase, was captured *in situ* by HRTEM imaging and SAED as sequences of laser pulses with different laser powers (5 pulses with 10 ms duration and 0.5 Hz frequency) were applied to a single region of supported graphene, as shown in Fig. 3.7. Crystallization of the amorphous precursors in Fig. 3.7 a-f was gradually induced by increasing the laser power (Fig. 3.6). After first shots at each laser power, a distinct change was observed which did not perceivably change with successive shots. Nevertheless, 5 laser pulses were applied for each laser power onto the precursor films to ensure that a uniform metastable state was reached at each power. The movie of crystallization was recorded and the snapshots of representative structures are presented in Fig. 3.7a-f. First, the amorphous nature of the as-deposited WSe_x was characterized by exhibiting no long-range order in HRTEM image (Fig. 3.7a) and a circular diffuse

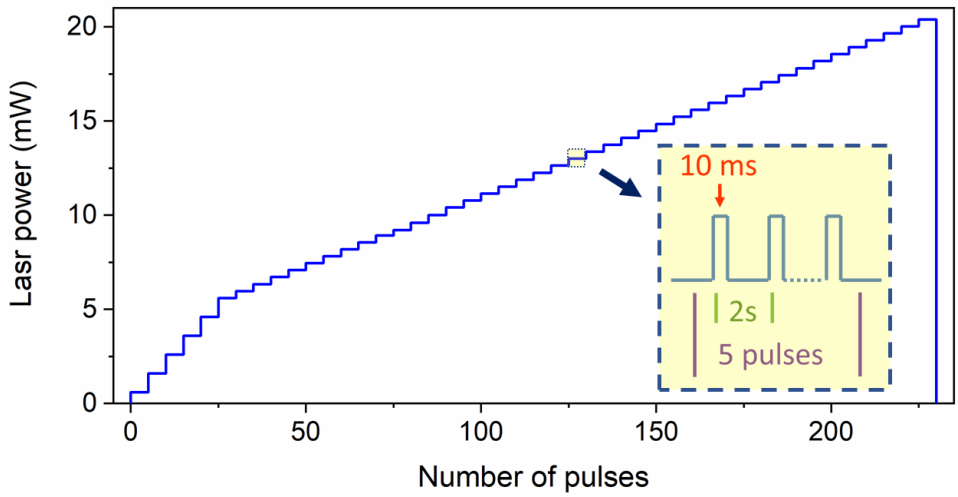

Fig. 3.6 Increment of laser power with number of pulses for both the crystallization experiments of WSe_2/graphene in Fig. 3.7, and $WSe_2/MoSe_2$ in Fig. 3.10.

ring that overlaps with the sharp spots that correspond to the Gr (001) zone axis in its SAED pattern (Fig. 3.7g-*A*). The surface morphology and SAED pattern barely changed when the laser power was ≤ 6 mW. After the laser power was increased to 7 mW, the first nanocrystals formed indicated by lattice–fringes in the HRTEM images (Fig. 3.7b). Another feature appearing in the HRTEM images is the (002) lattice fringes, showing that some crystals grow in vertical orientation (out of plane, lattice planes perpendicular to the Gr substrate). Similar "vertically-oriented" MoS_2 structures were reported as intermediate states forming on SiN_x substrates, so we will adopt this terminology.[113, 114] A close look at these vertically aligned structures, which reaches the highest density at 9.2 mW laser irradiation, is shown in the inset of Fig. 3.7c. The average interlayer distance of these vertical structures is calculated to be ~0.7 nm, slightly larger than the bulk counterpart of WSe_2 (0.65 nm). Although the growth processes of the vertically aligned TMD have been reported,[113, 114] their atomistic structure and compositions have not been studied. Here, we further studied the structure and composition of these vertically aligned structures using STEM and EELS.

When the power was increased to 13.4 mW, all of those vertically aligned structures disappeared, suggesting that these vertical structures are metastable intermediate phases (Fig. 3.7d). Also, the crystallinity of the flakes was improved substantially that is evident by the sharper ring-shape diffraction patterns (Fig. 3.7g-*C*) compared with those in Fig. 3.7g-*B*. The radial plots representing the circumferentially integrated SAED patterns from Fig. 3.7g are compared with the reference index patterns for planar Gr, planar WSe_2, and powder WSe_2 in Figure 3h. The radial plot of SAED pattern *B* can be deconvoluted as a composite of the stoichiometric WSe_2 layered structure plus other 3-dimensional metastable tungsten selenides. However, the line *C* shows only in-plane 2H-WSe_2 along with Gr along the (001) zone axis indicating a full conversion from a 3D metastable structure to 2D WSe_2. After the laser power was increased again, from 17.1 mW

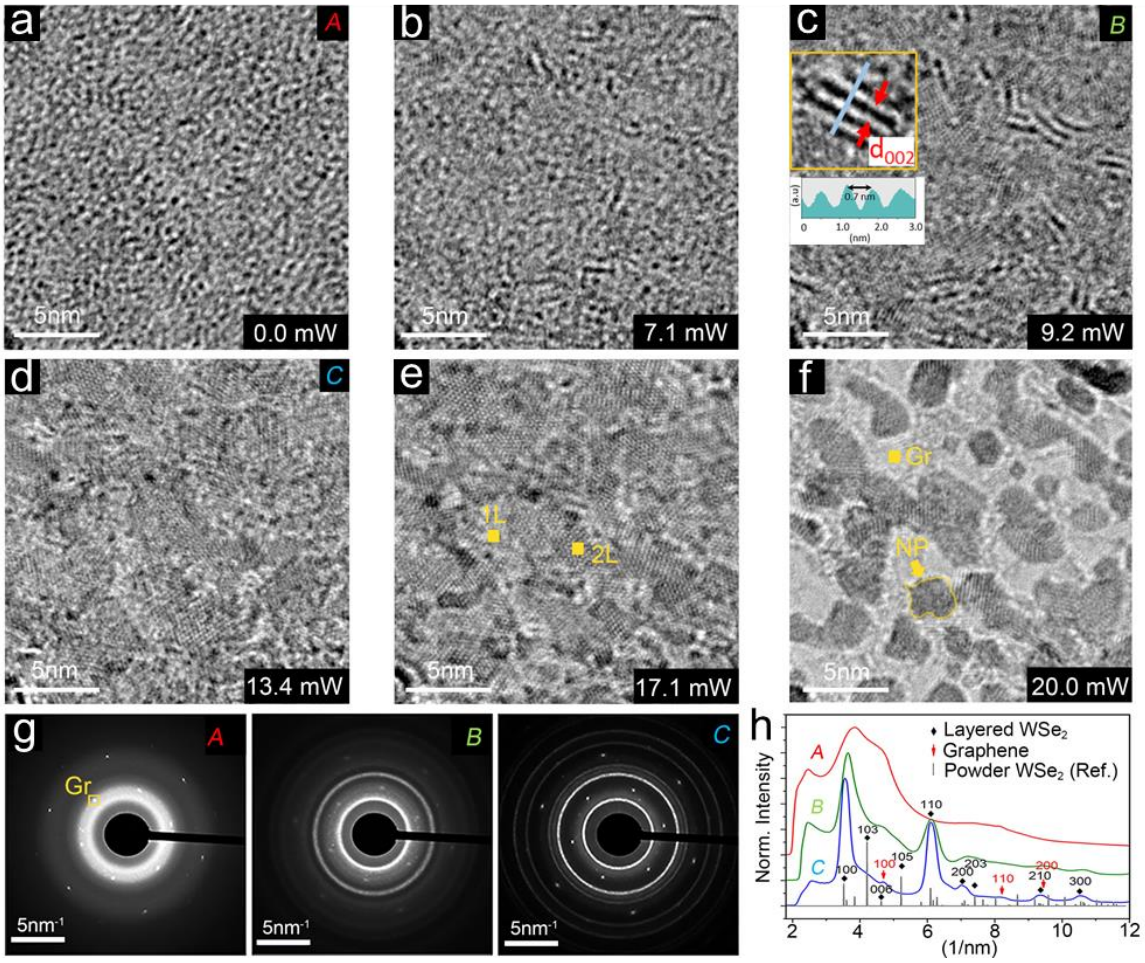

Fig. 3.7 Crystallization of WSe_2 on CVD graphene evolved with increasing laser energy. (a-f) HRTEM images corresponding to irradiation with laser powers of 0, 7.1, 9.2 and 13.4, 17.1, and 20 mW, respectively measured from the same focused area. (Laser pulse width: 10 ms; Repetition rate: 0.5 Hz) (g) The SAED patterns along (001) zone axis of the sample after laser irradiation of 0, 9.2 and 13.4 mW, respectively. (h) Radial plot of the circumferentially integrated SAED patterns in (g) showing the initial, intermediate, and final reciprocal spacing of the unirradiated, low-, and medium-laser power irradiated samples.

to 20 mW, the WSe_2 film permanently and irreversibly dissociated into a network of metal rich nanoparticles on Gr, indicating a dewetting of W-rich material.

Therefore, the changes induced by laser irradiation in the structure and stoichiometry of WSe_x precursors categorized into three regimes as a function of the irradiation laser power. In Regime I at low laser powers, a series of changes occurs leading to crystallization of intermediate phases in variable orientation. In Regime II at moderate laser powers, the out-of-plane metastable phases evolve into crystalline 2D material with the correct stoichiometry and in-plane orientation. In Regime III at higher than optimal laser powers, the 2D crystals are damaged and devolve into metal-rich, dewetted nanoparticles. The compositional evolution in these three irradiation regimes were analyzed during these transformations using *in situ* EELS.

The evolution of the precursor's chemical composition during thermal treatments is obviously a critical parameter in the pathway to crystallization toward the desired 2D phase. A major challenge during the optimization of growth techniques such as PLD for 2D TMD's are the compositional changes that occur due to the preferential loss of the volatile chalcogenide component, requiring a significant chalcogen oversupply depending on the growth method to achieve stoichiometric composition of the crystalline phase.[115, 116] Here *in situ* EELS was performed starting with the pre-deposited precursor under exposure to increased laser powers to correlate the compositional changes with materials structure, which are summarized in Fig. 3.8. Such compositional evolution has not been monitored in early *in situ* TEM heating of $(NH_4)_2MoS_4$ precursors for MoS_2 synthesis.[113, 117] In our experiments, we acquired an EELS spectrum after each stepwise increase in laser power, following 20 laser shots at the same laser power using 10 ms pulse widths. The EELS spectra with Se and W ionization-edges after background subtraction are presented in Fig. 3.8a. The calibration standard for the energy-loss edges of W and Se was an exfoliated flake of bulk WSe_2 crystal which was used as a benchmark to establish the 2:1 ratio of Se/W. Figure 4b shows the evolution of W

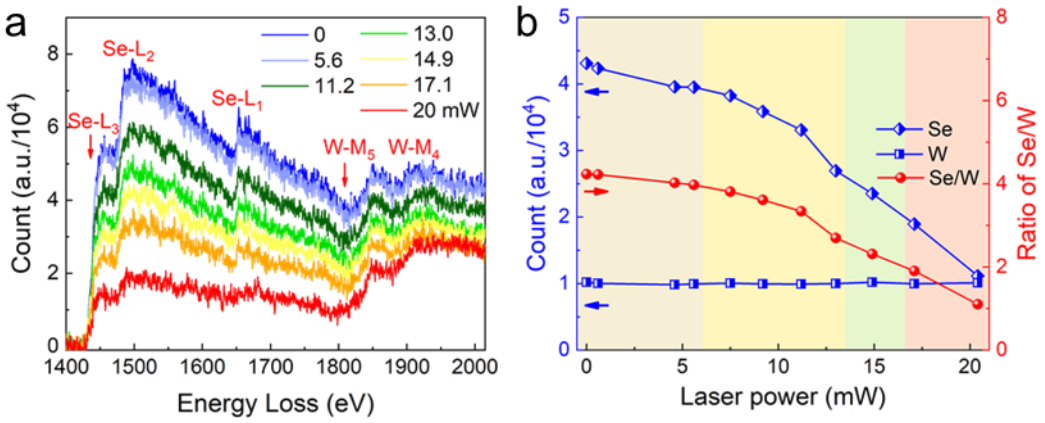

Fig. 3.8 Evolution of Se/W ratios during laser annealing monitored by *in situ* EELS. (a) EELS spectra of Se and W edges after background subtraction showing stoichiometry changes of PLD films irradiated with increased laser power at a fixed position. The EELS of Se (L_3) and W (M_5) edges used for calculation are marked at 1436 eV and 1809 eV, respectively. (b) Integrated intensity counts of W and Se EELS signals and Se/W ratio acquired at a fixed position showing the compositional evolution with increased laser power.

and Se intensities and the Se/W ratio derived from quantitative analysis of the core-loss EELS spectra.[48] The as-deposited *a*-WSe_x has a Se/W ratio of 4.2. Additional X-ray photoelectron spectroscopy (XPS) measurement of a large-area *a*-WSe_x film deposited on a Si substrate also indicates that the as-prepared film is Se rich (Se/W > 5), in agreement with other data in the literature obtained for WSe_x films deposited at RT.[118] As the laser power increased, Se was lost gradually while W remained constant because Se has a much higher vapor pressure. In the low power regime (from 6 to 13.5 mW), the Se/W ratio decreased from 3.9 to 2.6, and the irradiated film contained regions of nanocrystals in various 3D orientations (Fig. 3.7c and the inset), including the vertically-aligned nanocrystalline regions. These vertical structures are Se rich therefore are termed vertically aligned WSe_{2+x} structures. In the medium power regime (13.5 to 16.5 mW), the Se/W ratio dropped to the range of 1.9 to 2.6, and most of the nanodomains were 2H-phase.

After these dynamic *in situ* measurements, a series of irradiated tungsten selenide samples were prepared at different stages in the structural evolution for *ex situ* imaging investigation in an atomic resolution HAADF-STEM (Fig. 3.9). After low power irradiation (Regime I), the Se-rich amorphous nanoclusters and chains of the starting precursor material shown in Fig. 3.9a were converted into highly defective nanocrystals in different orientations (Fig. 3.9b), including the aforementioned vertically-aligned WSe_{2+x} nanocrystalline domains. In this non-stoichiometric film at this stage, no perfect in-plane 2H-WSe_2 could be observed. The intensity profiles in Fig. 3.9c show the vertically aligned domains that are only 2 layers tall. This intermediate layered structure shows an interlayer spacing larger than that of pristine 2H-WSe_2 layers (0.7-0.74 nm *vs*. 0.65 nm). According to the *in situ* EELS characterization, the Se to W ratio at this stage (~3:1) is still higher than the optimal (2:1) stoichiometry of WSe_2, indicating more Se in the highly defective nanocrystals and vertically aligned WSe_{2+x} crystals. However, after laser irradiation at 13.4 mW (Regime II), planar 1L-3L WSe_2 crystals are formed (Fig. 3.9d). The inset of Fig. 3.9d provides a detailed view of laser-synthesized 1L 2H-

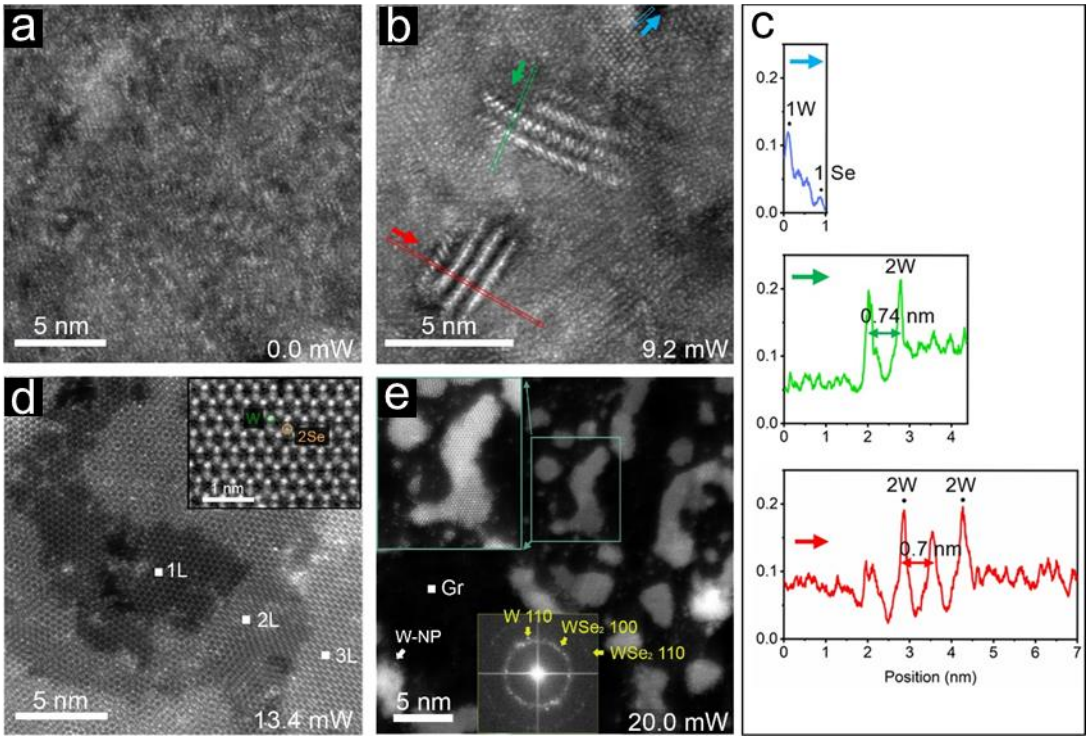

Fig. 3.9 Atomic-resolution *ex situ* HAADF-STEM characterization of the evolution of PLD-deposited tungsten selenide on graphene grids after sequential *in situ* laser treatments within a TEM. (a) *a*-WSe_x precursor prior to laser exposure. (b) After the laser treatment to 9.2 mW, the Se-rich film is crystallized in a variety of orientations and intermediate phases, including the vertically aligned WSe_{2+x} domains. (c) Intensity profiles of blue, green and red frames in Fig. 5b, revealing that the vertically aligned domains are only 2-layers tall and have a variety of layer spacings (0.7 and 0.74 nm). (d) After further laser treatment to 13.4 mW, the film has transformed completely into planar WSe_2 layers. Inset shows an atomically resolved HAADF image of 2H-WSe_2 monolayer structure on Gr. (e) After further exposure to 20 mW, the 2H-WSe_2 layered film on graphene decomposed into a Se-deficient network comprised of WSe_2 and W nanoparticles after being exposed to high-power laser. Inset in the upper left corner shows a dendritic structure with a portion of remaining (001) WSe_2 structure; Fast Fourier transformation (FFT) of the whole image in the bottom inset shows diffraction spots of WSe_2 and metallic W.

WSe_2.[112, 119] The Se to W ratio dropped to stoichiometric 2:1 at this stage as measured by *in situ* EELS analysis. Therefore, crystallization is observed to proceed through a series of metastable phases and changes in stoichiometry, with discrete thresholds, until a 2:1 Se:W ratio is observed, when a 2D layered crystal forms. At the final stage (Regime III), the 2H-WSe_2 film dewets and forms a Se-deficient network of thick WSe_2 islands or W nanoparticles (Fig. 3.9e and the inset) due to severe depletion of Se. Similar networks have been seen on the dewetted films of MoS_2 and WS_2 by either thermal or electrical heating.[113, 114, 120] Therefore, the dynamic composition of the constituents plays a significant role in determining the evolving structure of the 2D layer and is here directly correlated with the change from 3D- to 2D-oriented materials. In general, *in situ* TEM studies should be a powerful method to determine different synthesis pathways for different kinds of precursors (stoichiometry, morphology) toward developing practical laser crystallization approaches for 2D materials.

We have observed that Se-rich *a*-WSe_x precursors transform into stable 2D WSe_2 crystalline phases *via* metastable intermediate phases, a progression that is generally consistent with Ostwald's rule of stages.[121] During this progressive transformation toward more stable crystalline structures, increasing the laser power enables intermediate crystalline phases to thermally fluctuate and overcome the activation energies to reach a more stable state, where they remain stable over repeated irradiation at the same laser power. The available phases and stabilities are governed by the Se evaporation, unstable *a*-WSe_x first appears to crystallize into a variety of intermediate states of different stoichiometry and crystalline orientations before forming 2H-WSe_2 domains in vdW contact with graphene. This 2D WSe_2/Gr heterostructure is also metastable since it devolves at higher laser powers into mixtures of dewetted WSe_2 and W nanoparticles. *In situ* heating experiments on lacey carbon grids allow an estimate of the temperatures for 2D crystal crystallization. Although the results presented illustrate just one possible transformation pathway, it is clear that *in situ* HRTEM imaging,

SAED, and EELS of laser-induced transformations allows the visualization and characterization of growth pathways of crystallization through multiple metastable phases to optimize the synthesis of desired nanostructures.

3.3 *In situ* Synthesis of $WSe_2/MoSe_2$ heterostructure

3.3.1 $WSe_2/MoSe_2$ heterostructure formation

To understand how vdW epitaxial growth from amorphous precursors is assisted by a lattice-matched substrate, the similar evolution of crystallization processes as a function of laser power were investigated for the same *a*-WSe_x precursor film on 1L $MoSe_2$ (). The as-deposited *a*-WSe_x on 1L $MoSe_2$ (Fig. 3.10a) is amorphous, indicated by the absence of long-range-order structure in the image (Fig. 3.10a) and also by its SAED pattern (Fig. 3.10g-*A*). The bright Bragg spots in the diffraction pattern are from the $MoSe_2$ substrate, which also serves as a reference lattice. From 6 mW of laser power, nanocrystals and nanochains start to appear in the image (Fig. 3.10b). At a power of 9.2 mW, the morphology transforms to many small 2D nanodomains (Fig. 3.10c). The circular SAED pattern of *a*-WSe_x also became sharper (Fig. 3.10g-*B*) compared to the as-deposited one, indicating a higher degree of crystallinity. Additionally, polycrystalline WSe_2 domains caused Moiré fringes on the $MoSe_2$ in the image. Note that the vertically oriented nanodomains observed on graphene in Figs. 3.7c and 3.9b (and by others seen on amorphous substrates[113] and graphene[122]) were not observed on $MoSe_2$. The close lattice match between $MoSe_2$ and WSe_2 clearly promote planar growth of the stoichiometric WSe_2 phase at lower temperatures. At 13.5 mW of laser power, the size of domains increased together with the elimination of Moiré fringes (Fig. 3.10d), which is also evident by the 6-fold symmetry SAED pattern of aligned $WSe_2/MoSe_2$ (Fig. 3.10g-*C*). A dynamic SAED evolution with increasing laser power shows a continuous crystallization from amorphous, to 2D polycrystalline, and to the epitaxial formation of $WSe_2/MoSe_2$ by 13.5 mW (Fig. 3.11). Beyond 14

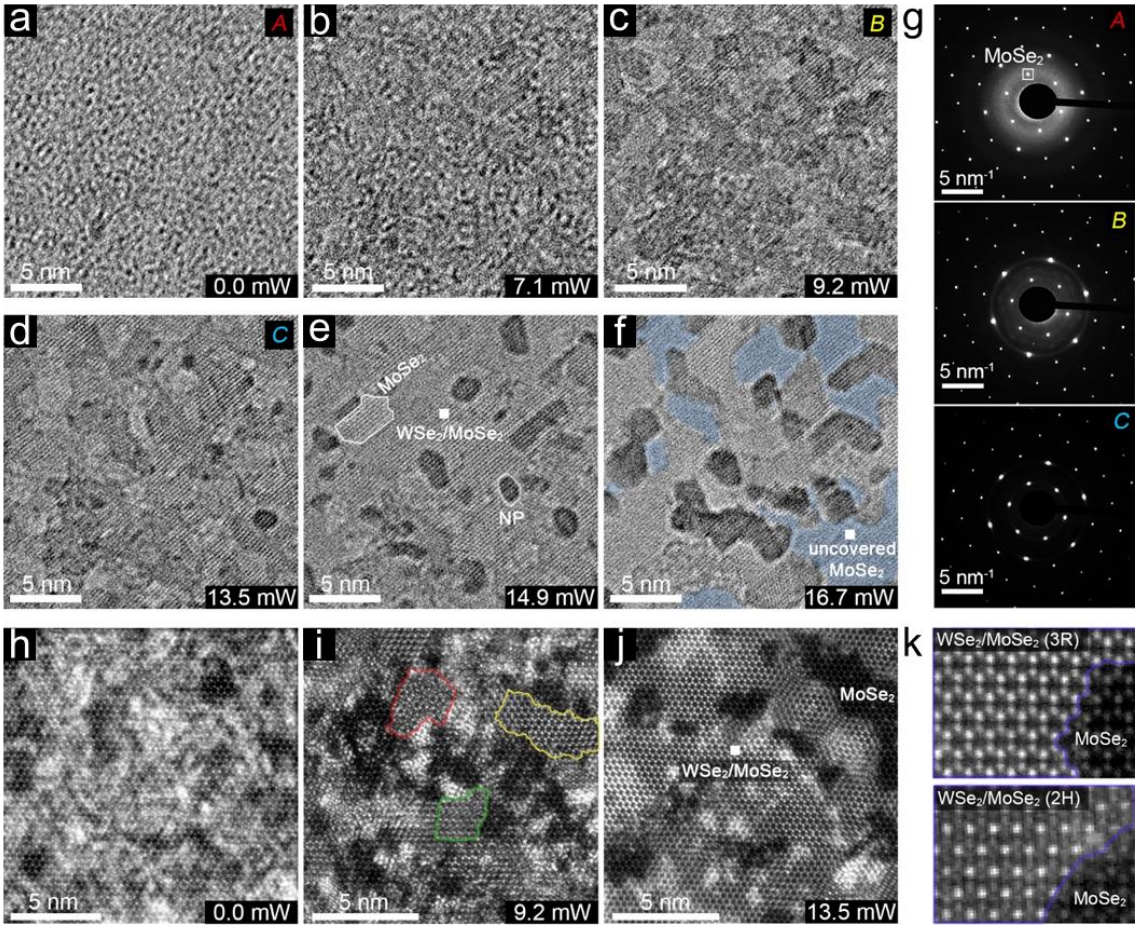

Fig. 3.10 Crystallization of WSe_2 on CVD grown 1L $MoSe_2$ evolved with increasing laser energy. (a-f) HRTEM images *vs* the increase of laser energy of 0, 7.1, 9.2, 13.5, 14.9 and 16.7 mW; In (f), after WSe_2 was removed, the uncovered $MoSe_2$ is put in a false color. (g: *A*-*C*) 2D SAED patterns of the 0, 9.2 and 13.5 mW laser-irradiated layers. (h-j) Atomic-resolution *ex situ* HAADF-STEM characterization of the evolution of PLD-deposited tungsten selenide on $MoSe_2$ grids after sequential in situ laser treatments terminated at 0, 9.2 and 13.5 mW respectively. (k) Enlarged HAADF view of 3R and 2H heterobilayers. (Laser irradiation conditions:10 ms, 0.5 Hz, 10 s for each power in (a)-(f))

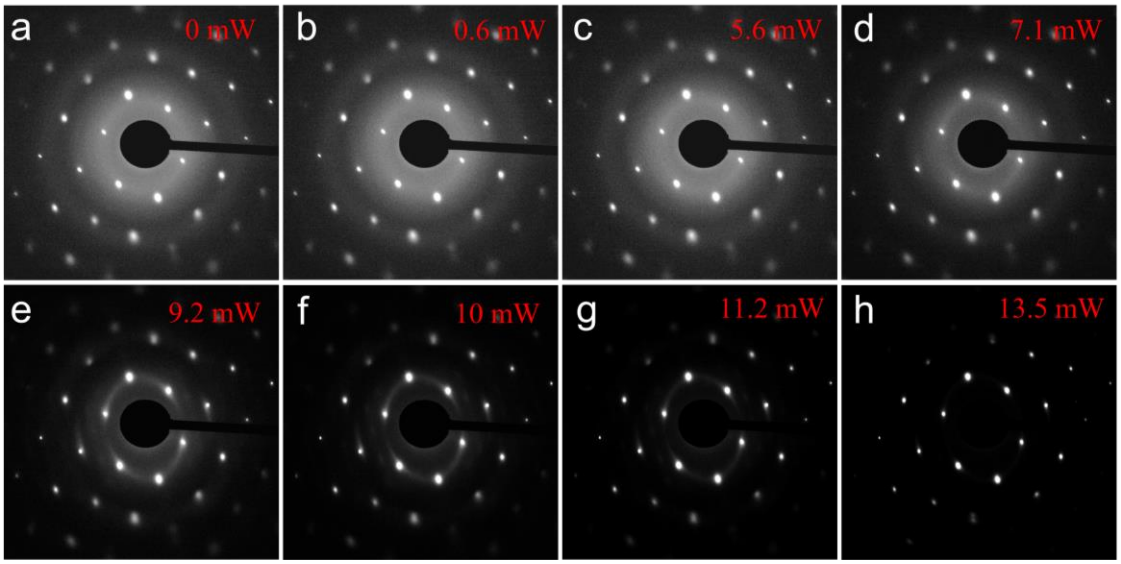

Fig. 3.11 *In situ* evolution of SAED patterns of WSe_2 precursor on $MoSe_2$ with increasing laser power at wavelength of 10 ms and frequency of 0.5 Hz showing a continuous crystallization from amorphous, to 2D polycrystalline, and to the epitaxial formation of $WSe_2/MoSe_2$ by 13.5 mW.. a) as deposited; b) 0.6 mW; c) 5.6 mW; d) 7.1 mW; e) 9.2 mW; f) 10 mW; g) 11.2 mW; h) 13.5 mW. WSe_2 starts to crystallize at 7.1 mW. It is fully crystallized at 9.2 mW while showing random orientation. At 13.5 mW, the diffraction ring almost vanishes, showing epitaxial alignment with $MoSe_2$ substrate.

mW, Se-depleted nanoparticles and some bare 1L $MoSe_2$ are observed due to dewetting of WSe_2 layers (Fig. 3.10e-f).

The heterostructures that were synthesized by stepwise pulsed laser heating of amorphous (PLD-deposited) precursors in the TEM on the 1L graphene and $MoSe_2$ substrates are nearly identical in crystallinity and alignment to the bilayer heterostructures that were produced directly by PLD on these same substrates at 600°C (Fig. 3.1c-d). While the precursors in direct PLD are delivered at 1 Hz and crystallized sequentially over ~ 20 pulses, the precursors in the TEM were delivered all at once, then laser-crystallized within the TEM. Despite these different synthesis pathways and the demonstrated variation in the size of the amorphous precursors, the similarity in the heterostructure crystallinity and alignment supports the hypothesis that vdW lattice matching from the substrate provides the dominant role in guiding the crystallization of amorphous precursors by vdW epitaxy.

3.3.2 Oriented attachment and self-rotation of WSe_2 nanodomains

After the amorphous precursor was partially crystallized by low power laser irradiation, WSe_2 nanodomains and sparse crystalline clusters coexisted, as shown in Fig. 6i. These nanodomains serve as the primary particles at the early stage of crystallization. Some of these primary particles already had good crystallinity, exhibiting 3R stacking with $MoSe_2$ (indicated by yellow outlines). Some particles were completely misoriented (red outlines), while others showed only small misorientation (green outlines). Both highly defective crystallites and amorphous clusters also surround these primary particles. At higher power (≥ 10 mW), these clusters and non-crystalline materials integrated with WSe_2 nanodomains and increased the domain size and crystallinity, as shown in Fig. 3.10j. Still, these key pathways of transformation from small polycrystalline domains to a large single crystal need to be understood.

Generally, two competing growth models, classical and non-classical, are used to explain crystallization. Classical crystal growth models are frequently invoked to

explain diffusion-controlled crystal growth processes, suggesting that nanocrystals grow by monomer attachment.[123, 124] By contrast, non-classical crystal growth includes nanocrystal growth by particle attachment, including processes involved in aggregation and oriented attachment. [123, 124] It is worth mentioning that classical and non-classical crystallization theories share the same initial stage of forming primary particles (nuclei) when the system deviates from equilibrium,[123] and they only differ at later stages.[125] In the non-classical model the primary nanoparticles arrange into an iso-oriented crystal by oriented attachment and form a single crystal upon the fusion of the nanoparticles.[123] Several studies have revealed that nanoparticles can grow simultaneously by monomer addition and particle attachment.[126, 127] In the following we will investigate which mechanisms are present in the growth of vdW epitaxial heterostructures.

To reveal the dynamics of growth pathways, a shorter laser pulse width of 300 μs was chosen to study crystallization on a finer time scale because simulations indicate that the transient heating of the material just reaches a steady state within this pulse width (no dwell time). Despite the reduced temperature produced in the SiN_x membrane and 2D substrates, this shortened laser pulse width does not affect the general trends that we saw previously using a 10 ms pulse width. This domain initially had a twist angle of about 30° (determined from dynamic FFTs) with the $MoSe_2$ substrate (25 mW/1p, Fig. 3.12a). Under continuous pulsed laser irradiation, the domain responded and rotated continuously until a thermally stable structure was achieved (29 mW/1 p, Fig. 3.12a). Fig. 3.12c shows two WSe_2 domains oriented differently (image labeled as 22 mW/1 p) attached to each other initially (A and B, highlighted with yellow and green dash lines respectively). Between the two domains, the B domain had a larger misorientation angle, according to its Moiré pattern. After 22 consecutive laser pulses at 22 mW, the B domain rotated noticeably, while the A domain remained stationary. Some portions of the original domain B incorporated into the A domain, while the remaining B domain exhibited a smaller misorientation angle based on the Moiré pattern. After

a few more pulses (22 mW/25 p, Fig. 3.12c), the two domains eventually formed a single domain.

The rotation of 2D domains is reminiscent of thermally-induced crystal rotation that has been observed on Gr and hexagonal boron nitride (hBN).[128, 129] For instance, Wang *et al.* demonstrated a Gr/hBN heterostructure with large misorientation angle can self-rotate into thermally stable configurations that reduces the misorientation after thermal annealing at 200 °C. Our results are consistent with these previous results. After WSe_2 nanodomains form, many of them are misoriented. With the thermal energy provided by pulsed laser irradiation, these misoriented WSe_2 domains could rotate until they achieve the stable states in the form of either 3R or 2H-type $WSe_2/MoSe_2$ heterobilayers.[130-132]

Another growth pathway to form larger single crystal domains is through grain boundary (GB) migration, which was observed as shown in Fig. 3.12b. The highlighted Moiré domain (within the red dashed lines) is from $WSe_2/MoSe_2$ with small misorientation angles (≤ 1°).[133] It gradually integrated with the adjacent domains by grain boundary migration with increasing pulse numbers at the same power. Since GBs are not energetically favored, the atoms at the grain boundary move until the misoriented WSe_2 domain manifested itself into a stable state with $MoSe_2$ (22 mW/12p and 40 p in Fig. 3.12b). The annihilation of stacking faults and reorientation of domains to homoepitaxial alignment by grain boundary migration were also observed by Zhao *et al*. in multilayered MoS_2 crystals.[134] Therefore, the interlayer interactions in 2D materials can play a significant role in guiding the reorientation of domains and leading to single-crystalline TMDs. These rotation and GB migration assisted by templates are consistent with oriented attachment of the non-classical model.[135]

The growth of WSe_2 domains is also seen to follow classical crystallization theory. The domain in Fig. 3.12a was surrounded by amorphous materials like those in Fig. 6i. Then it grew gradually by integrating nearby absorbing molecules and amorphous clusters (marked by red arrows). This observation indicates that

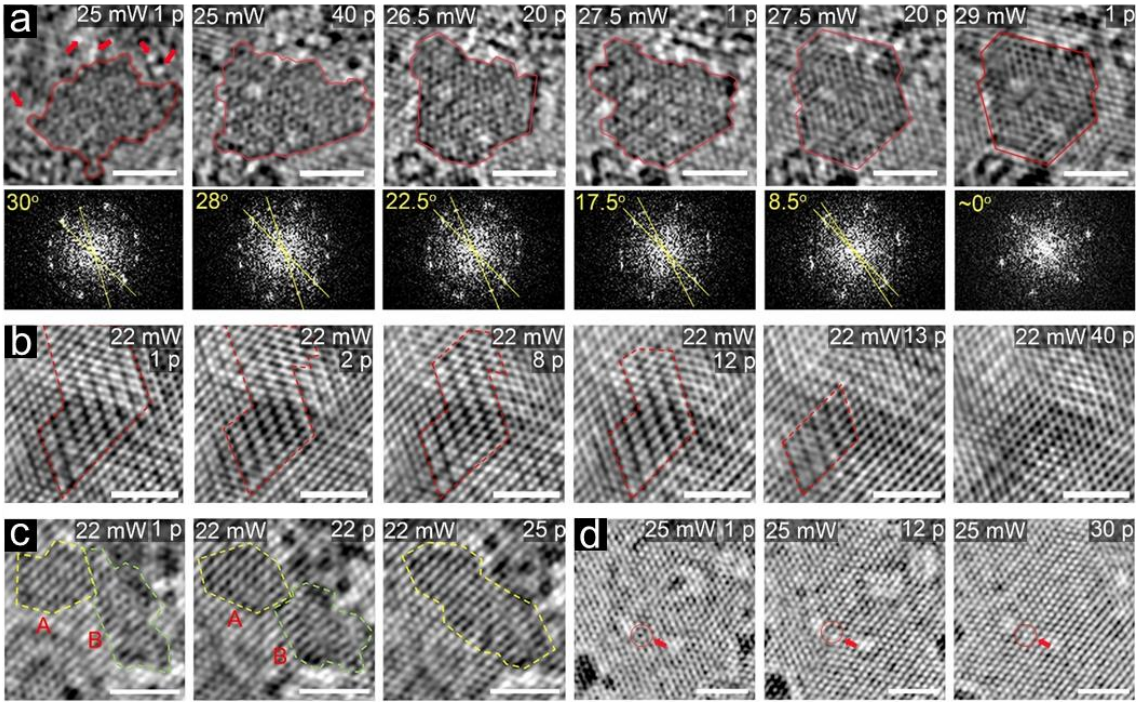

Fig. 3.12 Sequential *in situ* HRTEM images showing slow evolutions of WSe_2 nanocrystals on $MoSe_2$. (a) Top panel of images shows rotation and reshaping of a WSe_2 domain on top of $MoSe_2$, pulse by pulse with increasing laser power as indicated. Red arrows indicate the amorphous clusters that eventually attached to the domain. (b) Coalescence of a slightly misoriented domain and its surrounding domains by grain boundary migration. (c) Two originally misoriented attached domains, A and B, sequentially rotate and integrate into one domain with increasing numbers of laser pulses indicated. (d) Sequential elimination of surface corrugation under increasing laser pulses. (Pulse width: 300 μs; Repetition rate: 0.5 Hz; Scale bar: 2 nm)

the growth WSe_2 domains has contributions that follow the classical growth model of monomer attachment by substrate diffusion. Structural relaxation, including edge reshaping and short-range recrystallization, was also achieved by laser annealing. After nucleation, flakes with irregular shape or random planes (e.g., 25 mW, 1 p in Fig. 3.12a) can lower their surface energy and surface curvature upon laser irradiation when atoms on the surface diffuse to form {100} planes, terminating with hexagonal shapes as shown in the 29mW panel of Fig. 3.12a. Fig. 3.12d shows an area with wavy image contrast (potentially due to surface corrugation) after the bilayer was initially formed (25 mW/1 p, Fig. 3.12d). These features were eliminated after a short-range recrystallization by several pulses of laser irradiation (25 mW/12 p and 30 p, Fig. 3.12d).

In summary, a variety of classical and non-classical growth modes were observed to be active simultaneously in the dynamic, stepwise laser irradiation studies. Simultaneous monomer addition and oriented attachment were observed to increase the size of 2D WSe_2 domains grown on $MoSe_2$ substrate. The oriented attachment is completed by the rotation of domains that diminishes their misorientation and also the GB migration that eliminates the GBs, resulting in growing large, aligned WSe_2 domains on $MoSe_2$.

3.3.3 Impacts of substrate energetics on vdW epitaxy

The main difference between Gr and $MoSe_2$ substrates for WSe_2 crystallization is the ability to drive epitaxial alignment of the heterostructure across the vdW gap. To understand why the $MoSe_2$ substrate promotes single-crystalline heterostructure growth while graphene does not, we performed first-principles density functional theory (DFT) calculations to examine the energetics of triangular WSe_2 nanoflakes (consisting of 100 atoms) on larger Gr and $MoSe_2$ triangular nanoflakes. To accurately capture the energetics of such a large-scale system we performed DFT calculations using an all-electron electronic structure code that allows scalability to large system sizes on current distributed-parallel high-

performance computing architectures.[93] The number of atoms in our model systems range from 418 atoms to 498 atoms, where the distance between the layers remain fixed after optimization for each subsystem in terms of WSe_2 and its substrates (see Methods section for more details). Fig. 3.13b shows a side view of the two systems. The binding energy between the two nanoflakes (ΔE_b) for each system in Fig. 3.13c is defined as the total energy of the two nanoflakes at the indicated spacing and angle with respect to that of the asymptotic limit, where the two flakes are infinitely separated (no interaction). The optimum distance between WSe_2 and the substrate for a given configuration (θ) is determined at the minimum energy position (See the definition of θ in Fig. 3.13a). Fig. 3.13d compares the difference in the binding energy of the WSe_2 nanoflakes on the two substrates as a function of the misorientation angle (θ) with respect to the energy of the aligned ($\theta=0$) configuration (see Fig. 3.14a-b for precise stacking configuration) using the energies at the optimized interlayer spacings from Fig. 3.13c. This represents the energy barrier (ΔE_R) between different optimized rotational configurations of the WSe_2 nanoflake for each substrate. The results show a couple of local minima configurations for WSe_2 on $MoSe_2$. They are $\theta = 0°$, 30°, 60°, and 90°, with the deep potential wells at $\theta = 0°$ and 60°. For a WSe_2 flake consisting of 100 atoms within 2.37 nm^2, the ΔE_R is 51 meV per WSe_2 on $MoSe_2$ but only 9 meV per WSe_2 on Gr. When misoriented WSe_2 nanodomains receive thermal energies at elevated temperature (~ $\frac{3}{2} k_B T$, due to the degree of freedom of planar motions and vibration), they can rotate and migrate until the total energy on the substrates is minimized.[128, 129, 136, 137] In our models, the driving force for WSe_2 to rotate from metastable states to stable states can be described as $F = -\Delta(E_b)/\Delta(\theta)$. As shown in Fig. 3.13d, the driving force for rotation of WSe_2 on $MoSe_2$ is over 25 times greater than that on Gr for $45° < \theta < 75°$. As a result, misoriented WSe_2 domains are more prone to rotate on $MoSe_2$ than on Gr to achieve equilibrium.

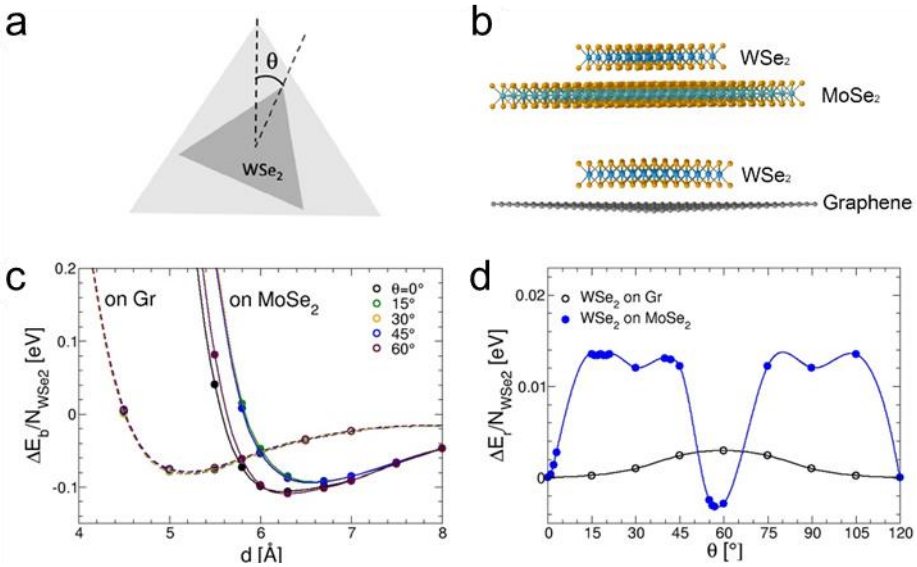

Fig. 3.13 First-principles description of energetics of WSe_2 on $MoSe_2$ or Gr substrates vs. misorientation angle. (a) A schematic illustration of rotation of a WSe_2 nanoflake on a substrate. (b) The atomic side views of WSe_2 on $MoSe_2$ (Top) and Gr (Bottom). (c) The binding energy of a WSe_2 nanoflake consisting of 100 atoms within 2.37 nm^2 as a function of interlayer spacing from Gr and $MoSe_2$ substrates. (d) The difference in the binding energies of the same WSe_2 nanoflake as a function of misorientation angle (θ) on Gr and $MoSe_2$ substrates. The energy of the heterostructures at 0° is set to zero.

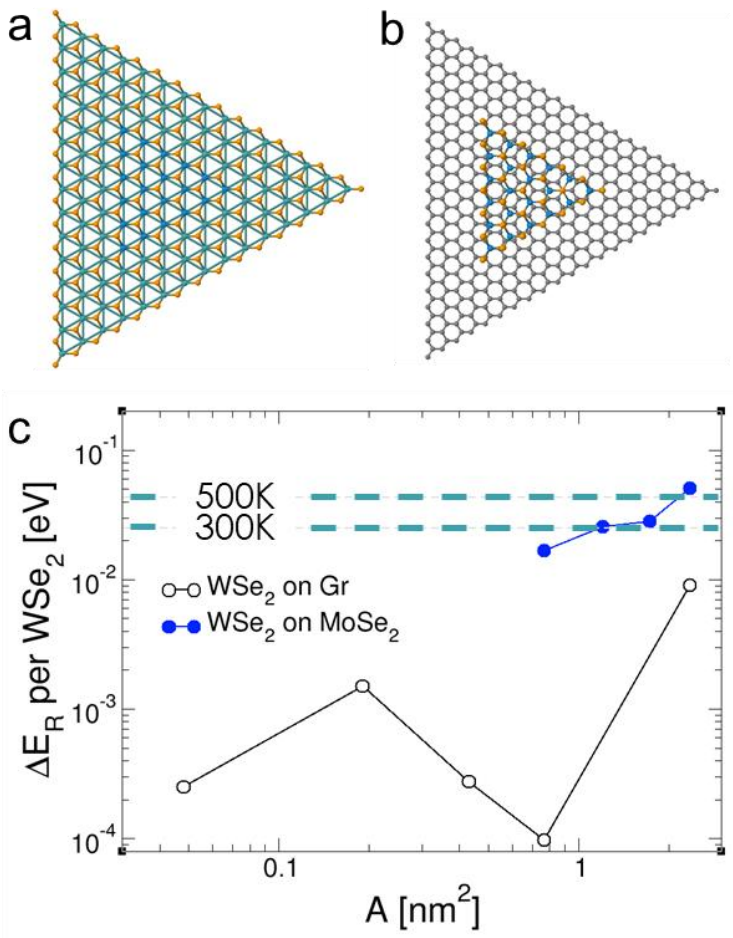

Fig. 3.14 The aligned ($\theta = 0$) stacking configuration of the heterostructures of $WSe_2/MoSe_2$ (a) and WSe_2/Gr (b). (c) Rotational energy barrier (ΔE_R) depending on the size of the WSe_2 nanoflake, translated to the area (A), on graphene and $MoSe_2$. The dash lines indicate thermal energy at room temperature (300 K) and 500 K.

As the experimental temperature increases, the probability of rotating a WSe_2 nanoflake increases exponentially. Therefore, the thermodynamic driving force for nanoflake rotation that enables the epitaxial alignment of the WSe_2 nanoflakes to the 2D substrates arises from the highly anisotropic energy distribution between the configurations with different orientations. Although the discussion above is focused on a very small nanoflake (2.37 nm^2) size, we also investigated ΔE_R and d for different WSe_2 flake sizes (Fig. 3.14c).

3.4 Summary

These *in situ* TEM studies revealed pathways by which amorphous precursors of tungsten selenide, which can vary in morphology from a film to loosely assembled small nanoparticles, can crystallize and coalesce to form atomically thin 2D layers and vdW heterostructures. Through the use of atomically thin substrates and stepwise laser-crystallization within the TEM, the nanoscale crystallization processes and guiding role of the substrate during vdW epitaxy could be directly visualized with *in situ* imaging, EELS, and SAED.

The excellent agreement between 2D vdW heterostructures grown by stepwise crystallization of pre-deposited precursors within the TEM and those directly deposited by PLD onto heated substrates indicate that similar processes are likely ongoing at much faster timescales within typical PLD at elevated temperatures (or other similar PVD processes such as sputtering).

Two regimes, crystallization and coalescence, were observed on both Gr and $MoSe_2$ monolayer substrates. First, the crystallization driven by pulsed laser irradiation proceeds through a series of changes in metastable phases and stoichiometry, with discrete energy thresholds, until a stable 1:2 stoichiometry of WSe_2 crystals was achieved. During this co-evolution of stoichiometry and structure as the precursor lost selenium and was attracted by vdW forces to form a semi-continuous layer, metastable nanophase domains of nonstoichiometric tungsten selenide were observed in TEM imaging. After each increase in laser

power (transient temperature pulse), the new structure and stoichiometry remained essentially constant over successive pulses with the same fluence. These results are consistent with Ostwald's law of stages, that indicates that crystallization can proceed through a series of metastable phases if barriers are overcome toward the most stable crystalline form. Polycrystalline WSe_2 monolayers or bilayers on Gr or $MoSe_2$ substrates can be thought of as a metastable phase also, since increasing to high laser powers can decompose it into W-rich particles. However, once WSe_2 layers are formed in intimate vdW contact with Gr or $MoSe_2$, they remained remarkably stable through the second phase of crystallization toward layer formation, the coalescence of neighboring nanophase domains.

The dominant guiding role of the substrate in the crystallization and coalescence process of forming vdW epitaxial heterostructures can be put in the context and terminology of crystallization by particle attachment (CPA) phenomena,[138] but in a novel two-dimensional context. This comparison is especially appropriate for the larger amorphous particle precursors explored in the studies. When amorphous nanoparticles encounter lattice-matched substrates during crystallization, the *in situ* studies revealed that a large fraction of these directly template to match the orientation of the substrate as they crystallize. The reorientation of the misaligned 2D domains to attach the substrate are accomplished by rotation and grain bound migration, as shown in Fig. 3.15. That such CPA processes occur during vdW epitaxy is remarkable, because typically covalent bonds are involved in the CPA of an amorphous particle. While CPA processes often are characterized in liquids, where particles are free to rotate in 3D, in the growth of vdW heterostructures the problem is reduced to 2D where rotation and migration are limited within a single plane. On Gr, with large lattice mismatch, DFT calculations indicate that small WSe_2 nanoflakes are easy to slip, rotate, and attach with other nanoflakes by CPA. However, with essentially no preferential rotation angle provided from the substrate, the random assortment of WSe_2 nanodomains on Gr will coalesce to

only nanometer dimensions. On the other hand, the DFT calculations show that the strong vdW attractive forces with respect to lattice matched $MoSe_2$ substrates tend to lock WSe_2 crystallites into epitaxial alignment. These crystallites provide edges for lateral attachment and recrystallization while flakes are able to rotate through the observed twisted Moiré orientations until the vdW attachment to the substrate orientation is achieved. In this way, large domains that all share a common crystalline orientation with that of the substrate evolved to form lattice matched, vdW heterostructures. Please note we not only observe the non-classical growth mode, but also the classical growth process like monomer attachment, as summarized in Fig. 3.15. Here we would like to emphasize that all the above classic and non-classical growth modes are active simultaneously in our system, but the rotational motion and substrate energy landscape make it possible to grow large single crystals.

We demonstrated that the guiding role of the substrate observed in the *in situ* TEM measurements permitted vdW heterostructures to be rapidly grown in a few seconds directly by PLD at 600 °C over large areas with grain sizes only limited by that of the underlying crystalline domains, as shown in Fig. 3.1d. These results to unravel the stepwise evolution of phase and structure within the TEM have direct implications to guide the vdW epitaxial growth of 2D crystals from direct PVD processes and for the laser crystallization of amorphous precursors deposited by such processes. As concluded in prior work with the sintering of ultrasmall TiO_2 nanoparticle precursors,[37] the timescales for such processes can be exponentially faster at the typical high temperatures employed in PLD (e.g., 600 °C here). Similarly here, with the appropriate choice of laser power, the entire crystallization and coalescence process was observed to occur within a single, milliseconds-long laser pulse. Such *in situ* TEM studies of non-equilibrium crystallization phenomena represent a transformational pathway to rapidly explore synthesis and processing methods occurring on much different length and time scales, and to stimulate the

development of *in situ* process diagnostics to capture such phenomena during growth using practical methods.

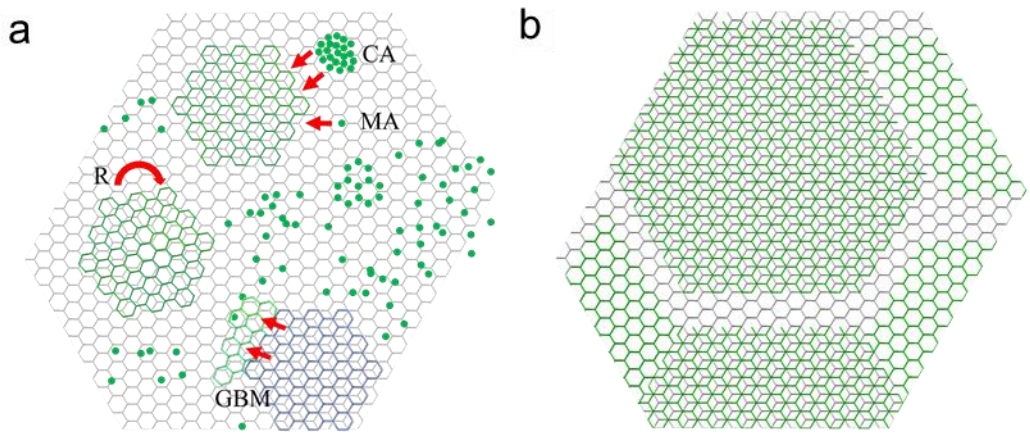

Fig. 3. 15 Schematic illustration of the multiple competing growth mechanisms observed during the laser crystallization of 2D heterostructures on lattice matched $MoSe_2$ substrates (grey hexagonal lattice). (a) Amorphous precursors (represented by green dots) are observed to crystallize and grow larger grains by molecular attachment (MA) or cluster attachment (CA). After crystallization, grain growth and coalescence are observed by both classical crystallization theory and non-classical crystallization model (oriented attachment). Oriented attachment is accomplished by rotation (R) and grain boundary migration (GBM). (b) Larger oriented grains in different stacking (2H and 3R) are fused by lateral recrystallization enabled by substrate-induced rotation and grain boundary migration.

Chapter 4. Synthesis of Janus TMDs through controlling energy of plasma plumes using *in situ* diagnostics

In this chapter, we explore precise tailoring of the hyperthermal nature of pulsed laser ablation plasmas to implant Se species with KE < 10 eV/atom into WS_2 ML. We first determine the thresholds for soft landing, for selenization limited to the top-most S layer, and for selenization of the bottom S layer. Then we demonstrate that by controlling the KE, selective and complete selenization of the top layer of suspended or supported WS_2 ML can be achieved to form high-quality Janus WSSe ML at low (300 °C) temperatures in an implantation and recrystallization process. The WSSe Janus monolayer structure was confirmed by atomic-resolution electron microscopy in tilted geometry.

4.1 *In situ* diagnostics of Se plasma plumes

Hyperthermal Se species with KE < 42 eV/atom were naturally generated by laser vaporization of a solid Se target in vacuum and were directed toward WS_2 ML crystals on TEM grids or substrates as shown in Fig. 4.1a. The plasma plume propagation was measured by a combination of *in situ* intensified-CCD array (ICCD) photography of its visible luminescence (Fig. 4.1b) and ion probe current waveforms measured at different positions (Fig. 4.1c). By adding 5-50 mTorr of argon, the plasma plume was decelerated controllably to tune the maximum KE of species arriving at the substrate from 42 eV/atom in vacuum, to < 1 eV/atom at 100 mTorr. The plume deceleration followed a standard $a = -\alpha v^2$ drag model (Fig. 4.1c),[139, 140] however the small deceleration coefficient compared to typical atomic and molecular plasmas,[37] along with its highly forward-directed angular distribution and weak luminescence, implied that its main constituents were clusters.[139, 140]

The weakly-ionized plasma travels at maximum velocities of ~ 1 cm/μs in vacuum (Fig. 4.1b) and is only weakly luminescent until arrival at the substrate,

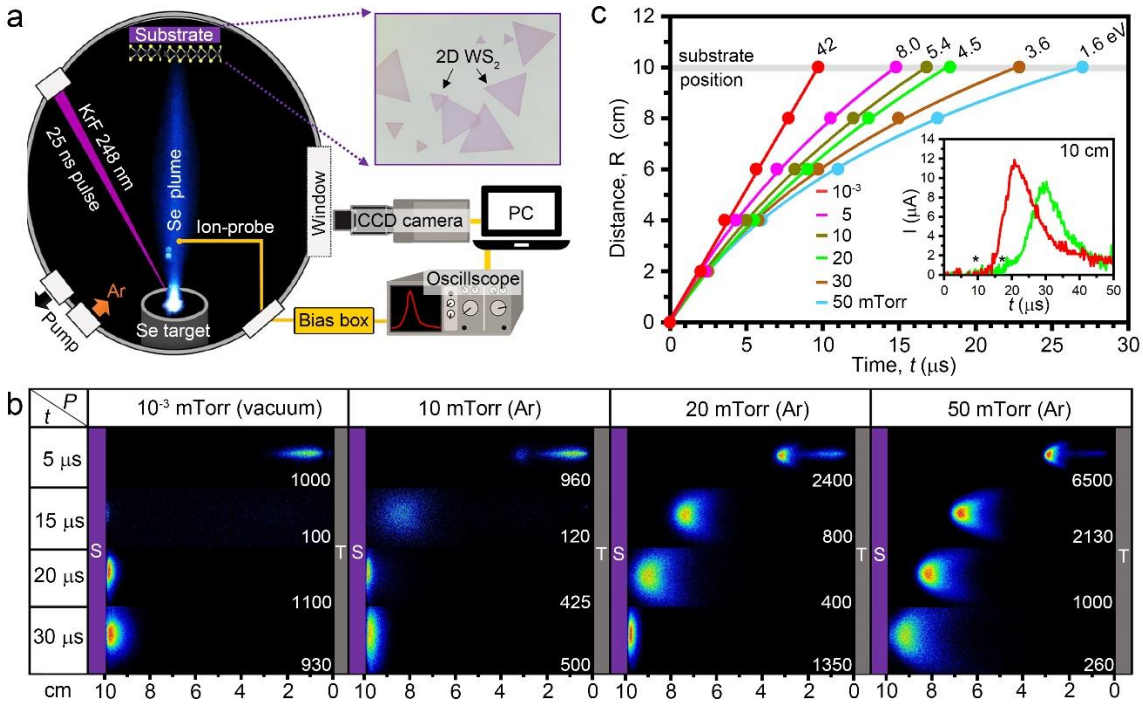

Fig. 4.1 *In situ* diagnostics of Se plasma plumes. (a) Experimental setup for Se plasma plume generation and impingement on CVD-grown WS_2 ML within a vacuum chamber equipped with an ICCD camera and a translatable probe for ion-flux measurement. (b) False color, gated-ICCD images of the Se plasma's visible luminescence reveal the plume's propagation dynamics through vacuum and 10, 20, and 50 mTorr argon background gas pressures at the indicated delay times following the laser pulse. (Gate width is 10% of each delay time, maximum intensity is shown for comparison.) (c) R-*t* plots of the leading edge of the plasma (from ion probe currents, see * in inset) track the propagation and deceleration in different background Ar pressures.

where collisions within the boundary layer result in comparatively brighter emission. Similarly, confinement of the plasma by the Ar gas during propagation results in significantly enhanced emission intensity as shown in Fig. 4.1c.

4.2 Correlation of kinetic energy of plasma plume with structure

WS_2 MLs were exposed to Se plasma plumes with different maximum KEs. The substrates were held at 250°C to desorb excess Se within 1 ms after each pulse arrived, as measured by time-resolved optical reflectivity. After deposition, Raman and photoluminescence (PL) micro-spectroscopies were used to gauge the extent of conversion of the WS_2 crystals for equal numbers of Se pulses using different KEs. As shown in Fig. 4.2a, for 800 Se pulses at pressures ≥ 40 mTorr, corresponding to KE ≤ 3 eV/atom, the characteristic (2LA(M)+E')[141] Raman peak at 350 cm^{-1} of WS_2 ML was barely affected, indicating little or no selenization. Corresponding PL peak positions were unaffected from unexposed WS_2 ML until 40mTorr, where spectral broadening became noticeable. When the pressure was lowered to 20 mTorr, corresponding to < 4.5 eV/atom, two predominant Raman peaks measured at 278 cm^{-1} and 320 cm^{-1} resemble out-of-plane and in-plane vibrations of a Janus WSSe ML predicted at 277 cm^{-1} and 322 cm^{-1},[142] indicating that the upper S layer was largely replaced with Se. With further increase in KE, the Raman and PL spectra continue to transform until the Raman peak at 251 cm^{-1} and PL peak at 1.67 eV of WSe_2 ML were obtained, indicating full conversion of WS_2 to WSe_2.

To understand atomistic effects of the KE-dependent selenization process, WS_2 ML crystals were suspended on TEM grids, exposed to Se plume pulses under the same conditions, and then examined using high angle annular dark field (HAADF) Z-contrast scanning transmission electron microscopy (Z-STEM). The samples exhibit 3 regimes, summarized in Fig. 4.2c: (i) For low KE < 3 eV/atom, no perceptible Se incorporation or lattice damage was observed. (ii) At 4.5 eV/atom, significant replacement of S by Se in the lattice was confirmed by image contrast

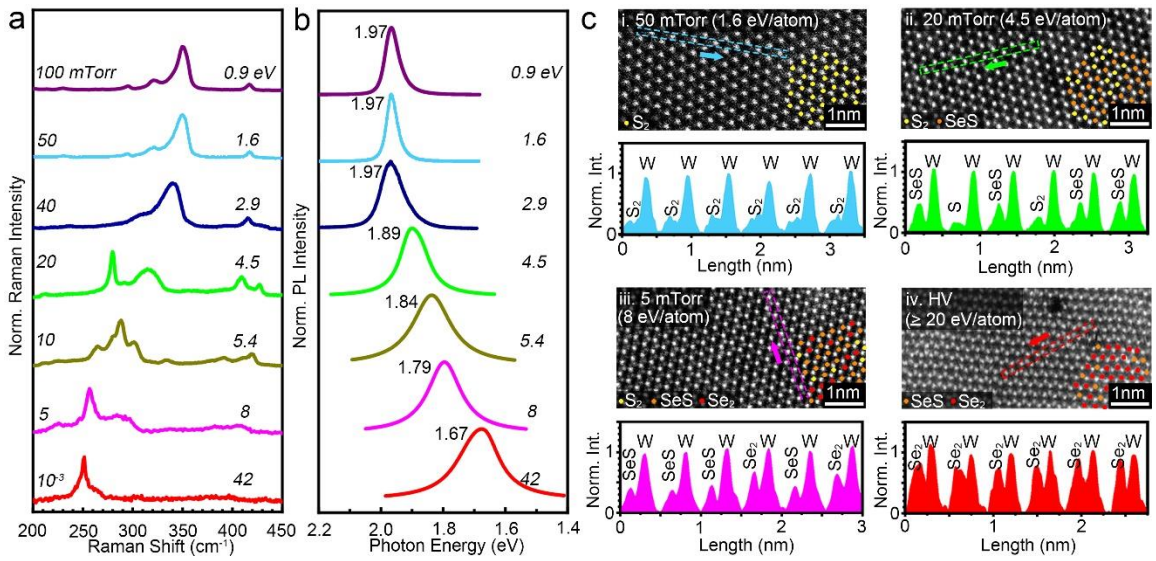

Fig. 4.2 Characterizations of $WS_{2(1-x)}Se_{2x}$ ML converted from WS_2 by Se plasma plumes. (a) Raman spectra of WS_2 ML on SiO_2/Si substrates exposed by 800 Se plasma plume pulses in different background Ar pressures at 250 ^oC. (b) Corresponding PL spectra and peak energy positions of the irradiated WS_2 MLs measured in (a). (c) HAADF Z-contrast STEM images of WS_2 ML suspended on TEM grids and irradiated by Se plasma plumes arriving through Ar pressures with maximum KEs: i) 50 mTorr (1.6 eV/atom, 800 pulses), ii) 20 mTorr (4.5 eV/atom, 800 pulses), iii) 5 mTorr (8 eV/atom, 600 pulses), and iv) 10^{-6} Torr (≥ 20 eV/atom, 600 pulses). Chalcogen columns containing S-S, Se-S, and Se-Se pairs in the images are labeled with yellow, orange, and red balls based on their Z-contrast intensity (based on $Z^{1.9}$ scaling) with respect to W. The line profiles below each panel compare the relative Z-contrast intensity between W and dichalcogenide sites.

line profiles which reveal columns containing S-Se pairs but not Se-Se pairs. The fraction of S-Se pairs approach 100% with increasing numbers of shots, suggesting that just the atoms in the top S layer might be selenized to form Janus MLs. (iii) For higher KE, (≥ 5.4 eV/atom) columns containing Se-Se pairs appear in higher concentration in addition to Se-S pairs, suggesting penetration of Se to the lower layer of S atoms.

4.3 Characterization of Janus structure using UltraSTEM

The experimental data indicates that controlling selenium KE ≤ 4.5 eV/atom should selenize only the top layer of S atoms in WS_2 without causing W atom displacement, enabling the formation of a Janus WSSe ML. Therefore, WS_2 MLs suspended on TEM grids or supported on SiO_2/Si substrates were held at 300 °C and exposed to 2000 Se plume pulses (at 5 Hz) in 20 mTorr Ar gas. The samples directly converted on TEM grids were first imaged by Z-contrast STEM as shown in Fig. 4.3a, b to identify the chalcogen compositions by their Z-contrast. As shown in Fig. 4.3c, a histogram of image intensities scaled (by $Z^{1.9}$) to the intensity of the W atom peak, reveals that all of the chalcogen columns can be assigned to Se-S pairs (and not S, Se, S-S, or Se-Se), consistent with Janus ML formation.

To understand whether the substituted Se atoms were all situated on one side of the ML, the TEM grid was tilted by 15° around both x- and y-axes and re-imaged to get a perspective view, as shown in Fig. 4.3d. A comparison of the HAADF image with the overlaid ball-and-stick model shows that the Se atoms are all located on one side of the monolayer and the Se-S pairs are oriented in the same direction across the image, which corresponds to a Janus structure. For comparison, simulated HAADF images from a Janus ML in both normal and tilted views are shown in Fig. 4.3e. The images and simulated linescan intensities in Fig. 4.3f agree well with the experimental images. The experimental tilted images were also compared with simulated tilted views of pure WS_2 and WSe_2 ML (Fig. 4.4) to confirm the presence and uniformity of the Janus ML. In addition, other tilt angles

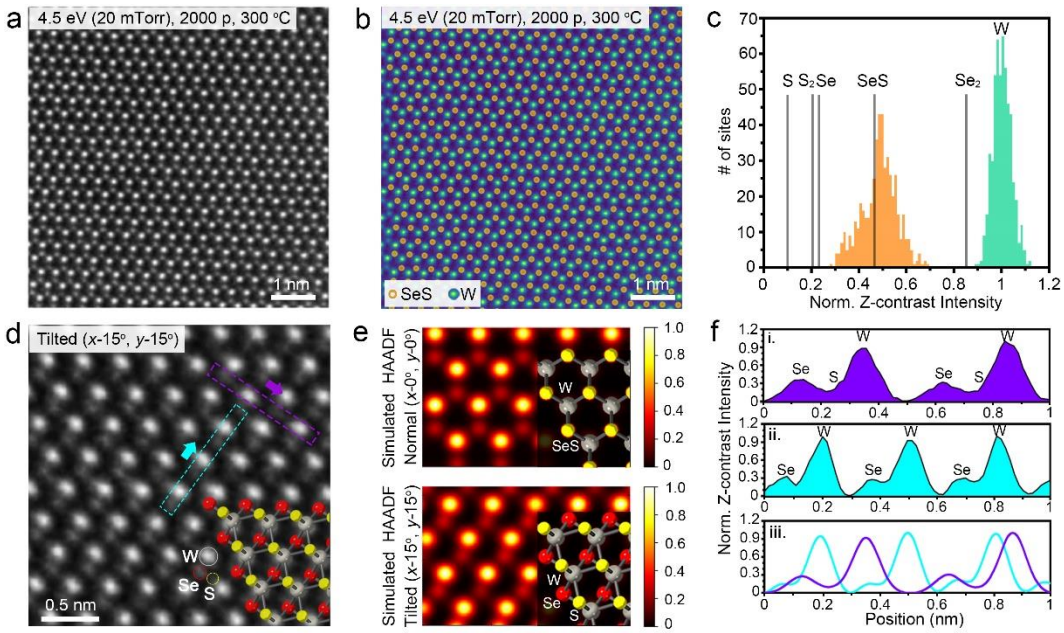

Fig. 4.3 Characterization of Janus WSSe ML formed by Se implantation in WS_2. (a) Normal view HAADF Z-contrast STEM image of WS_2 ML irradiated by 2000 Se plume pulses at < 4.5 eV/atom. (b) Same image as in (a) where Se-S sites and W sites are colored orange and green, respectively. (c) Histogram shows the numbers of W and Se-S pairs found in (b), indicating full conversion of S-S into Se-S. (d) A tilted HAADF Z-STEM image (x-15°, y-15°) permits visualization of both top and bottom atoms of a Janus WSSe ML. (e) Simulated Z-contrast STEM image intensities and models (insets) for the Janus WSSe ML in normal (top) and tilted (bottom) views agree well with the experimental STEM images. (f) i) and ii) intensity line profiles from (d) match well with iii) the simulated intensity from an idealized Janus structure.

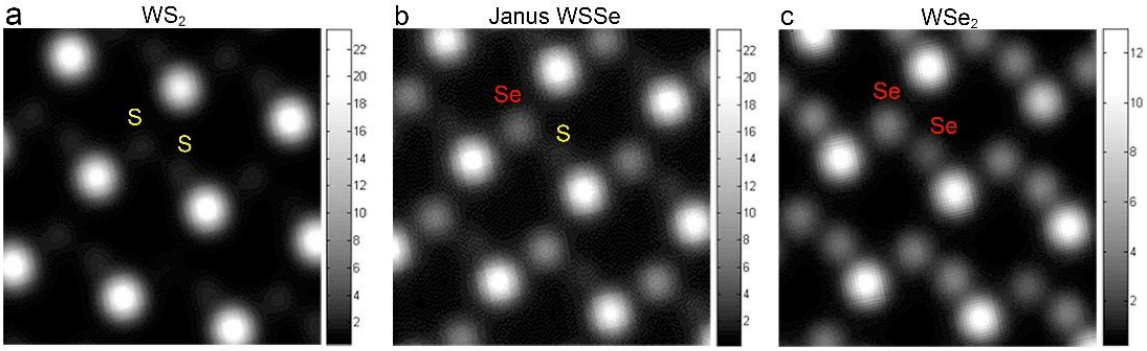

Fig. 4.4 Simulated HAADF-Z-STEM images for (a) WS2 (b) Janus WSSe (c) WSe2 monolayers tilted at x = +15° and y = +15°. For reference, the locations of representative S and Se atoms are indicated just above the atom positions in the images.

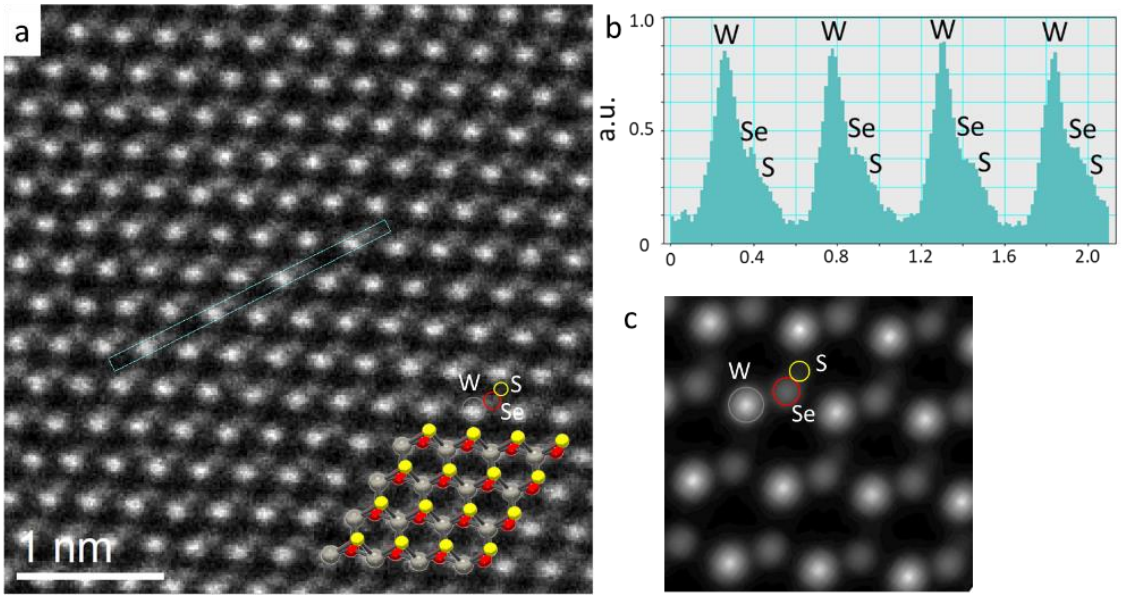

Fig. 4.5 Tilted HAADF-Z-STEM images of ML Janus WSSe (a) Experimental image tilted at x = +15° along with overlaid ball-and-stick model with W atoms (gray), Se atoms (red) and S atoms (yellow). (b) The line intensity profile across the atomic chain highlighted by the green box in (a) shows the relative intensity of detected electrons compared to the W peak, with definable shoulders of Se, then S, in a repeating pattern. (c) The corresponding simulated STEM image for Janus WSSe tilted at x = +15°, confirms the relative intensity ratio measured experimentally.

were explored to confirm that the projected image changed accordingly. For example, a comparison of experimental and simulated tilted HAADF-STEM images for a rotation about x = +15^{o} of 2D WSSe are shown in Fig. 4.5. The projections of S and Se are displaced as expected, however not as far as the relatively large distance in the HAADF image of Fig. 4.3 with a tilt angle of x = +15^{o} and y = +15^{o}, which permitted a more straightforward intensity analysis.

4.4 Summary

In summary, moderating the natural hyperthermal kinetic energy of species inherent within pulsed laser deposition plasmas to < 10 eV has revealed the thresholds for selenization of suspended WS_2 monolayer crystals, summarized in Fig. 4.6, including a ~3-5 eV/atom window for the low-temperature (< 300 °C) formation of high-quality Janus WSSe ML. This non-equilibrium synthesis process permits materials of interest to be controllably implanted to different depths within atomically thin layers. The key to the process is the implantation of extra atoms to form high energy defect structures that are Se-rich and disordered. This implantation process overcomes a significant fraction of the barrier ≤ 8.8 eV/Se for a single Se adatom to diffuse to the bottom layer. For low KE (3-5 eV/atom) for Janus layer formation, the damage is localized in the top chalcogen layer of the monolayer, and recrystallization into a Janus ML requires < 300 °C.

However, Se implantation to the lower chalcogen layer can be achieved experimentally by Se species with 5-8 eV/atom KE. These impacts are also sufficient to displace W atoms. At even higher energies, such as 40 eV/atom, rapid selenization of both layers occurs despite the irreparable loss of W atoms caused by these larger Se clusters. In both cases, moderate 600 °C substrate temperatures allow the crystal to self-repair, returning displaced W atoms to their lattice sites and reorganizing pores. Through repeated Se implantation and recrystallization, the WS_2 crystal can be fully converted into either Janus WSSe or WSe_2 MLs, with the extent of alloying controlled by the number of Se dose pulses.

These results provide valuable insights to guide the bottom-up PLD synthesis of 2D materials and to develop hyperthermal implantation as a top-down method to explore the synthesis of metastable 2D Janus layers and alloys of variable composition.

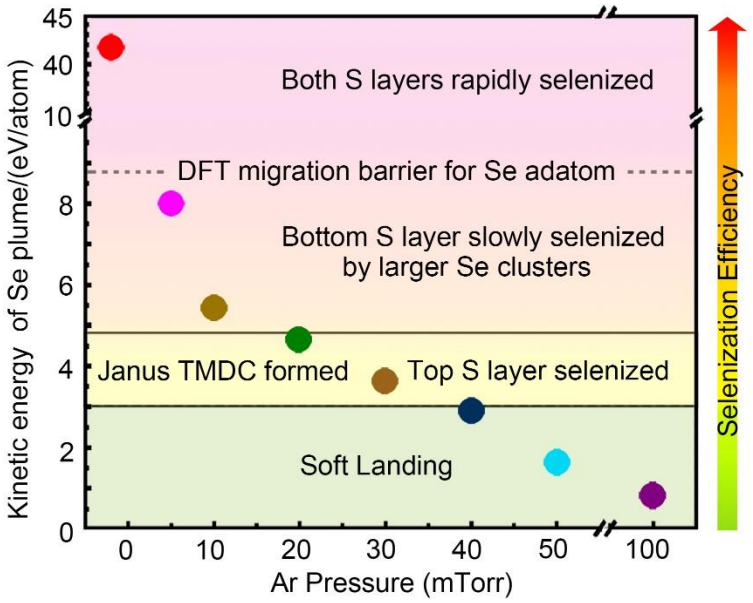

Fig. 4.6 Summary diagram of KE regimes for selenization of WS_2 ML by implantation using Se PLD. Points indicate maximum KEs measured from Se plume leading edge arriving at suspended WS_2 MLs placed at 10 cm as shown in Fig. 4.1 for different background Ar gas pressures. For ≥ 40 mTorr selenium species soft-land inducing no selenization or damage, then desorb for > 200 °C. Selenization of only the top S layer of WS_2 ML suitable for Janus WSSe formation occurs between 20-40 mTorr for Se plume KEs between 3-4.5 eV/atom. At low pressures (≤ 20 mTorr) and plume KEs above 5.4 eV/atom, selenization of the bottom S layer by larger Se clusters increases and becomes rapidly once pressures decrease towards vacuum.

Chapter 5. Characterization of plasmons using Photon Stimulated Electron Energy-Gain

In this chapter, Here, through a combination of experiment and theory, we demonstrate a low irradiance continuous wave (cw) regime (10^8 W/m^2) where strong photon-plasmon coupling is critical to observing the sEEL and sEEG signals; in this way, we expect bright plasmon modes to couple stronger than dark plasmon modes. This resonant mode provides the ability to spectrally and spatially map the steady- state near field of individual plasmonic nanostructures via cw photo-excitation and a continuous electron source in the (S)TEM.

5.1 Characterization of Photon Stimulated Electron Energy-Gain and Energy-Loss

5.1.1 *In situ* synthesis of silver particles

Motivated by the desire to investigate excited state phenomena in plasmonic nanomaterials, we leveraged a recently developed optical delivery system that can be attached to any (S)TEM for both photothermal heating[102] and excitation modalities and used it to image the plasmonic responses of individual silver nanoparticles in the weak-field continuous wave (cw) limit. The particles are photothermally dewetted from a continuous 30 nm thick silver film (Fig. 5.1) using our *in situ* laser delivery system. Fortuitously, the photothermally dewet nanostructures do not have any silver oxidation because they are generated in high vacuum and provided a distribution of particle shapes and sizes in which to probe for resonance with our laser energy. Fig. 5.2a is a schematic illustrating the system, developed by Waviks, Inc., attached to a monochromated (S)TEM. The system consists of a laser diode with an emission wavelength of 785 nm and a 1 nm (or 1.4 meV) full-width-half-maximum (FWHM) linewidth. The tunable laser optical power (up to 215 mW) is coupled to a 5 μm diameter single mode fiber optic and the end of the fiber is placed at the focal distance of the lens sub-system which

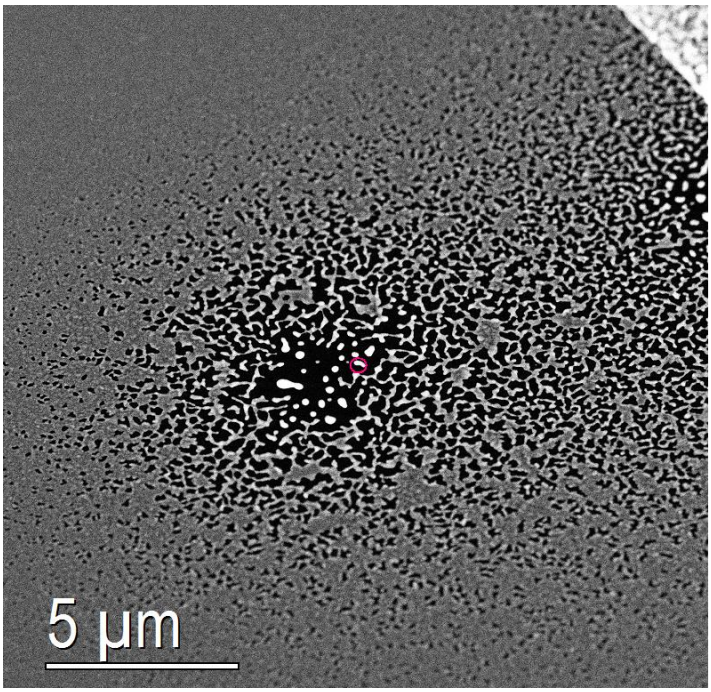

Fig. 5.1 HAADF image of the dewetted silver film.

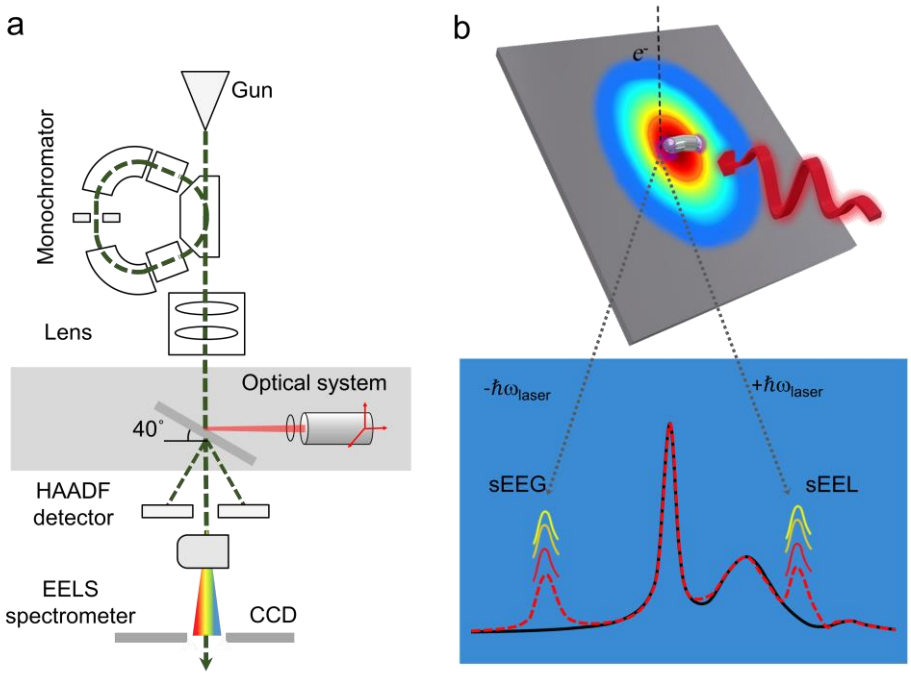

Fig. 5.2 Overview of (S)TEM/EELS and laser system. (a), Schematic of the monochromated (S)TEM/EELS instrument with the optical delivery system mounted orthogonal to the electron beam. (b), Illustration of the coincident and cw focused laser light and 200 keV electron beam; the laser spot has a 3.7 mm radius Gaussian profile and interacts with the sample to produce signature sEEL and sEEG peaks whose intensities vary with laser irradiance.

re-images the fiber optic end with unit magnification at an approximate working distance of 1 cm. As shown in Fig. 5.2, the unpolarized 3.7 μm radius Gaussian laser spot (at $1/e^2$ irradiance measured at normal incidence and thus slightly elongated due to the tilt) is focused and aligned to the (S)TEM electron coincident point on a 40° tilted sample via a 3-axis nanomanipulator system [see Wu et al. for system details].[102] While all results presented here were operated in cw, the laser can be pulsed down to a several ns pulse width at up to 16 MHz frequency at a wavelength of 785 nm (1.58 eV). At maximum power and focus, a cw irradiance on the 40° tilted substrate can reach up to ~2×10^9 W/m^2.

5.1.2 sEEL and sEEG of a silver irregular nanoparticle

Fig. 5.3 shows the unprocessed low-loss sEEL/sEEG point spectra of a photothermally dewetted silver nanoparticle (see HAADF (S)TEM image in inset) as a function of laser power at the aloof beam position indicated by position A (see Fig. 5.4 for full spectra). Inspection of the EEL spectrum (without laser irradiation) reveals an energy resolution of 0.136 eV as measured by the FWHM of the ZLP. During the experiment, there are slight changes in the ZLP attributed to microscope instabilities and a change in the high-energy side of the background consistent with electron beam induced carbon deposition from prolonged electron exposure. The surface plasmons are clearly visible and no noise reduction or other data enhancement was performed on the spectra. In the laser irradiated spectra, two additional peaks emerge, and are attributed to the sEEL and sEEG peaks at $\pm\hbar\omega_{\mathrm{laser}}$, respectively, at $\pm$1.58 eV. For clarity we plot the data using standard EELS convention so the sEEG signature is at negative electron energy-loss.

For the zero irradiance spectra (laser off), there are two plasmon peaks in this low loss region of interest: one centered at ~1.05 eV and another small peak centered near the laser wavelength 1.48 eV. Detailed peak fitting of the spectra was performed to analyze the full low-loss/gain spectra (Fig. 5.4). Position, width, amplitude, and scattering probability (integral of peak area) of all peaks are

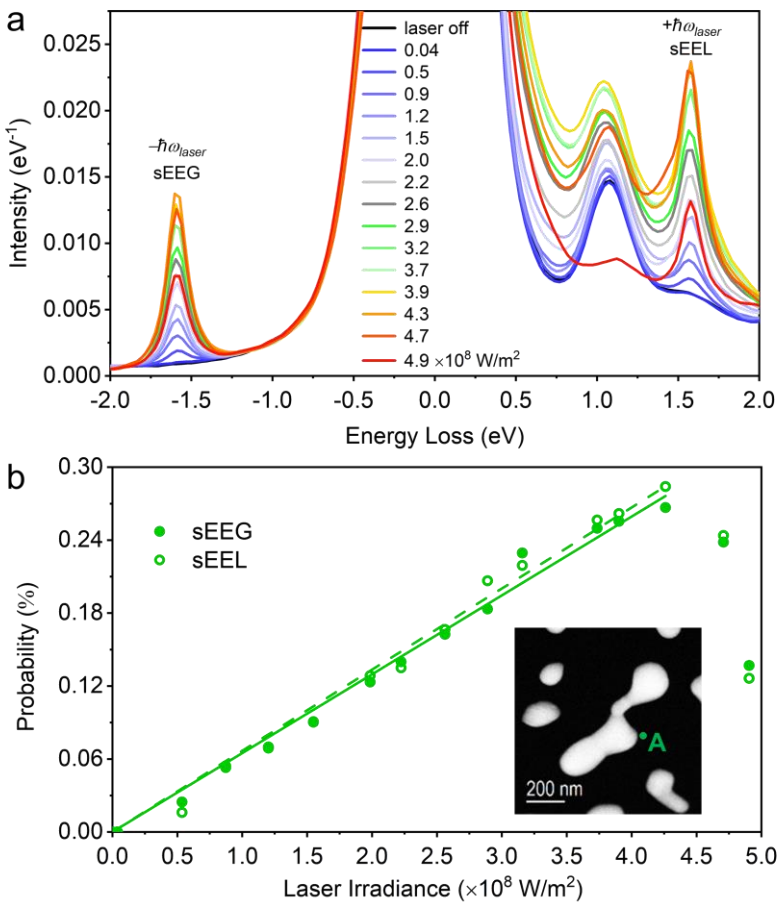

Fig. 5.3 sEEL and sEEG of a silver irregular nanoparticle as a function of laser irradiance. (a), The unprocessed low-loss EEL/EEG point spectra of a photo-thermally dewetted silver nanoparticle as a function of laser irradiance (×10^8 W/m^2) at the aloof beam position indicated by the green bullet and label A. (b), The integrated sEEG and sEEL probabilities as a function of laser irradiance for the spectra in (a). The solid and dashed lines are linear fits to the sEEG and sEEL data, respectively.

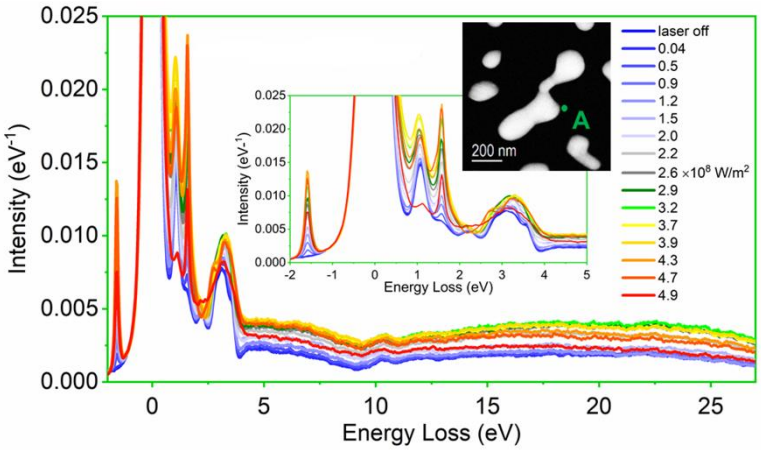

Fig. 5.4 The unprocessed low-loss EEL/EEG point spectra of a photothermally dewet silver nanoparticles as a function of laser irradiance (W/m^2) for the Position A in Fig. 5.3.

Table 5.1 Evolution of the probability (%) of every peak (eV) with increasing laser energy irradiance ($\times 10^8$ W/m^2) at Position A in Fig. 5.3.

	EEGS	0.721	1.051	1.476	SEELS	2.147	2.785	3.204	5.164	18.442
0	0	0.008	0.400	0.386	0	0.224	0.046	0.590	0.614	3.549
0.04	0	0.022	0.369	0.393	0	0.218	0.057	0.570	0.613	3.391
0.5	0.025	0	0.398	0.389	0.016	0.178	0.034	0.596	0.844	3.474
0.9	0.054	0.035	0.499	0.386	0.053	0.241	0.073	0.622	0.983	3.609
1.2	0.069	0	0.414	0.375	0.070	0.200	0.042	0.611	0.886	3.763
1.5	0.091	0.037	0.480	0.425	0.090	0.199	0.046	0.667	0.988	4.740
2.0	0.123	0.026	0.428	0.386	0.129	0.204	0.054	0.623	0.965	4.490
2.2	0.141	0.178	0.520	0.567	0.132	0.191	0.062	0.651	1.104	6.136
2.6	0.163	0.226	0.542	0.567	0.167	0.190	0.060	0.649	1.116	7.140
2.9	0.183	0.396	0.542	0.567	0.207	0.170	0.051	0.629	1.124	7.474
3.2	0.229	0.250	0.542	0.567	0.219	0.183	0.006	0.763	1.161	7.811
3.7	0.250	0.249	0.542	0.567	0.257	0.141	0.043	0.673	1.170	7.458
3.9	0.255	0.188	0.542	0.565	0.262	0.277	0.028	0.780	1.211	7.600
4.3	0.267	0.116	0.542	0.520	0.284	0.203	0.092	0.682	1.167	6.778
4.7	0.238	0.204	0.591	0.423	0.244	0.203	0.174	0.603	1.163	6.295
4.9	0.137	0.057	0.203	0.258	0.126	0.343	0.001	0.730	0.831	4.826

Table 5.2 Evolution of the position (eV) of every peak (eV) with increasing laser energy irradiance ($\times 10^8$ W/m^2) at Position A in Fig. 5.3.

	EEGS	0.721	1.051	1.476	SEELS	2.147	2.785	3.204	5.164	18.442
0	Null	0.77	1.06	1.50	Null	2.21	2.83	3.17	5.28	19.02
0.04	Null	0.84	1.07	1.52	Null	2.27	2.86	3.18	5.27	18.52
0.5	-1.585	0.73	1.06	1.52	1.580	2.21	2.81	3.14	5.03	18.51
0.9	-1.588	0.76	1.07	1.52	1.582	2.27	2.86	3.21	5.57	18.56
1.2	-1.589	0.74	1.06	1.50	1.582	2.20	2.83	3.16	5.09	17.65
1.5	-1.587	0.76	1.06	1.50	1.582	2.18	2.82	3.18	5.21	18.23
2.0	-1.587	0.79	1.06	1.49	1.582	2.19	2.83	3.18	5.15	17.93
2.2	-1.590	0.64	1.04	1.49	1.582	2.22	2.82	3.21	5.20	18.88
2.6	-1.592	0.64	1.02	1.48	1.582	2.27	2.85	3.22	5.07	19.37
2.9	-1.589	0.62	1.04	1.48	1.582	2.27	2.84	3.22	4.91	19.28
3.2	-1.587	0.74	1.06	1.46	1.582	2.01	2.72	3.17	5.19	19.33
3.7	-1.588	0.84	1.08	1.58	1.582	2.27	2.79	3.24	5.17	18.85
3.9	-1.587	0.71	1.04	1.35	1.582	1.88	2.72	3.20	5.29	18.77
4.3	-1.588	0.72	1.04	1.44	1.582	2.02	2.70	3.25	5.22	18.15
4.7	-1.587	0.71	1.08	1.49	1.578	1.98	2.65	3.30	5.09	17.74
4.9	-1.589	0.72	1.02	1.40	1.587	2.05	2.72	3.17	5.17	16.91

Table 5.3 Evolution of the FWHM (eV) of every peak (eV) with increasing laser energy irradiance ($\times 10^8$ W/m^2) at Position A in Fig. 5.3. Please note that the FWHM of EEGS and SEELS are the same as that of the zero-loss peak.

	EEGS	0.721	1.051	1.476	SEELS	2.147	2.785	3.204	5.164	18.442
0	0.13	0.18	0.34	0.67	0.13	0.63	0.32	0.87	3.57	20.78
0.04	0.13	0.18	0.31	0.68	0.13	0.63	0.32	0.87	3.64	20.43
0.5	0.14	0.17	0.32	0.68	0.14	0.63	0.32	0.87	4.57	19.89
0.9	0.15	0.16	0.37	0.66	0.15	0.63	0.32	0.87	4.57	17.72
1.2	0.13	0.21	0.34	0.67	0.13	0.63	0.32	0.87	4.57	20.33
1.5	0.13	0.18	0.36	0.67	0.13	0.63	0.32	0.87	4.57	23.02
2.0	0.13	0.16	0.34	0.66	0.13	0.63	0.32	0.87	4.57	22.36
2.2	0.15	0.24	0.37	0.74	0.15	0.63	0.32	0.87	4.57	22.54
2.6	0.15	0.24	0.37	0.74	0.15	0.63	0.32	0.87	4.57	24.06
2.9	0.15	0.36	0.37	0.74	0.15	0.63	0.32	0.87	4.57	24.98
3.2	0.14	0.32	0.37	0.74	0.14	0.63	0.32	0.99	4.57	24.98
3.7	0.13	0.48	0.37	0.74	0.13	0.63	0.32	0.89	4.57	24.98
3.9	0.13	0.24	0.37	0.74	0.13	0.63	0.32	1.06	4.57	24.98
4.3	0.13	0.24	0.37	0.68	0.13	0.63	0.32	0.94	4.57	24.98
4.7	0.13	0.32	0.40	0.55	0.13	0.66	0.50	0.87	4.57	24.98
4.9	0.13	0.16	0.40	0.60	0.13	0.93	0.15	1.14	4.21	23.47

Table 5.4 Evolution of the amplitude (ev^{-1}) of every peak (eV) with increasing laser energy irradiance ($\times 10^8$ W/m^2) at Position A in Fig. 5.3.

	EEGS	0.721	1.051	1.476	SEELS	2.147	2.785	3.204	5.164	18.442
0	0	0.001	0.011	0.006	0	0.003	0.001	0.007	0.002	0.002
0.04	0	0.001	0.011	0.006	0	0.003	0.002	0.006	0.002	0.002
0.5	0.001	0.000	0.012	0.006	0.001	0.003	0.001	0.007	0.002	0.002
0.9	0.003	0.002	0.013	0.006	0.003	0.004	0.002	0.007	0.002	0.002
1.2	0.004	0.000	0.012	0.005	0.004	0.003	0.001	0.007	0.002	0.002
1.5	0.005	0.002	0.013	0.006	0.005	0.003	0.001	0.007	0.002	0.003
2.0	0.007	0.002	0.012	0.006	0.007	0.003	0.002	0.007	0.002	0.002
2.2	0.007	0.007	0.013	0.007	0.007	0.003	0.002	0.007	0.002	0.003
2.6	0.008	0.009	0.014	0.007	0.008	0.003	0.002	0.007	0.002	0.004
2.9	0.009	0.011	0.014	0.007	0.010	0.003	0.002	0.007	0.002	0.004
3.2	0.012	0.008	0.014	0.007	0.011	0.003	0.000	0.007	0.002	0.004
3.7	0.013	0.005	0.014	0.007	0.013	0.002	0.001	0.007	0.003	0.004
3.9	0.013	0.008	0.014	0.007	0.013	0.004	0.001	0.007	0.003	0.004
4.3	0.014	0.005	0.014	0.007	0.015	0.003	0.003	0.007	0.002	0.003
4.7	0.013	0.006	0.014	0.007	0.013	0.003	0.003	0.007	0.002	0.003
4.9	0.007	0.003	0.005	0.004	0.007	0.004	0.000	0.006	0.002	0.003

provided in the Table 5.1-5.4. Notably, the average FWHM of the sEEL and sEEG peaks fits (0.136±0.0089 eV) match well with the FWHM of the ZLP.

Fig.5.3b is a plot of the integrated sEEG and sEEL probabilities as a function of laser irradiance for the spectra in Fig. 5.3a. Interestingly, the EEL spectrum in Fig. 5.3a at zero laser irradiance has only a small plasmon peak near the 1.58 eV laser energy; however, the laser couples strongly to this apparent bright mode, which also interacts with the field of the swift (<500 attosecond interaction time) passing STEM electron as evidenced by the strong sEEL and sEEG peaks in the spectrum. Notably, the sEEL and sEEG peaks increase approximately linearly as a function of laser irradiance in the range of 8.8×10^{7} W/m^2 to 4.3×10^{8} W/m^2. Consistent with previous PINEM results[63, 64] and as discussed below in our modeling results, the sEEL and sEEG peak intensities have approximately the same integrated probability. Note that because of the relatively low cw laser irradiance values relative to PINEM, only single quantum exchanges of energy between the laser, target, and electron beam are observed as no multi-photon sEEL and sEEG responses are detected. Additionally, and consistent with the lower irradiance, there is no detectable change in the ZLP intensity. Interestingly, both peak intensities decrease at irradiance values > 4.3×10^{8} W/m^2, which is attributed to photothermal heating of the silver nanostructure, which is known to damp plasmons and shift the resonance to lower energy. When the laser is increased slightly to 5×10^{8} W/m^2, the silver nanostructures studied evaporate completely (see Fig. 5.7 for images). Furthermore, the broad plasmon modes associated with the electron-beam induced carbon deposition also concurrently decrease in the > 4.3×10^{8} W/m^2 irradiance region.

5.1.3 sEEL and sEEG of a silver nanoparticle with rod-like structure

Fig. 5.5a and b show the point spectra as a function of irradiance at the aloof positions of the rod-like structure shown in the inset of Fig. 5.5c (see Fig. 5.6 for full low-loss spectra). Position, width, amplitude, and scattering probability (integral

of peak area) of all peaks are provided in the Table 5.5-5.12. Again no data processing was performed for the spectra. Fig. 5.5c is a plot of the integrated sEEL and sEEG probabilities as a function of irradiance taken at these two positions (ignoring the spontaneous EEL contribution convoluted on the loss side); note the sEEL and sEEG probabilities are again comparable for each position. The rod has approximate dimensions of ~330 nm long, an average width of ~120 nm and average height of ~100 nm (assuming an equilibrium wetting angle for the trans-axial dimension of 135 degrees). At the aloof positions at the rod ends, the spectra consist of peaks associated with the longitudinal dipole (1.21 eV), longitudinal quadrupole (2.3 eV), and several higher-energy (> 3 eV) modes including the transverse dipole among higher-order modes. Note the intensity of the higher order mode peak at ~ 3.5 eV varies in the unprocessed data, which has contributions from carbon deposition (and removal at higher irradiance) and likely slight electron beam mispositioning over the duration of the experiment. No multi-photon sEEL is contributing as evidenced by the energy gain region having no peaks at $-2\hbar\omega_{\mathrm{laser}}$= 3.16 eV. Fig. 5.5d illustrates the 1.21 eV dipole mode EELS map at zero irradiance, which has the expected high probability distribution at the rod ends (see Fig. 5.8 for complementary 2.3 eV quadrupole mode map). Fig. 5.5e and f are the associated sEEG and sEEL probability maps, respectively, when exposed to an irradiance of ~2×10^8 W/m^2. The sEEG probability map is consistent with the longitudinal dipole map, which suggests good coupling to this bright mode despite the laser energy being detuned ~0.37 eV to higher energy from the dipole plasmon resonance. As the spectra illustrate in Fig. 5.5e and f and the longitudinal dipole map suggests in Fig. 5.5d, the EEL probability is slightly higher on the right side of the rod and thus concomitantly the sEEG and sEEL probabilities are slightly higher on the right hand side of the rod. For position A, where relatively higher laser powers were explored, the sEEL and sEEG probabilities decrease when the irradiance exceeded ~ 4×10^8 W/m^2 and the silver nanostructure evaporated when the irradiance exceeded 5.4×10^8 W/m^2 (Fig. 5.7).

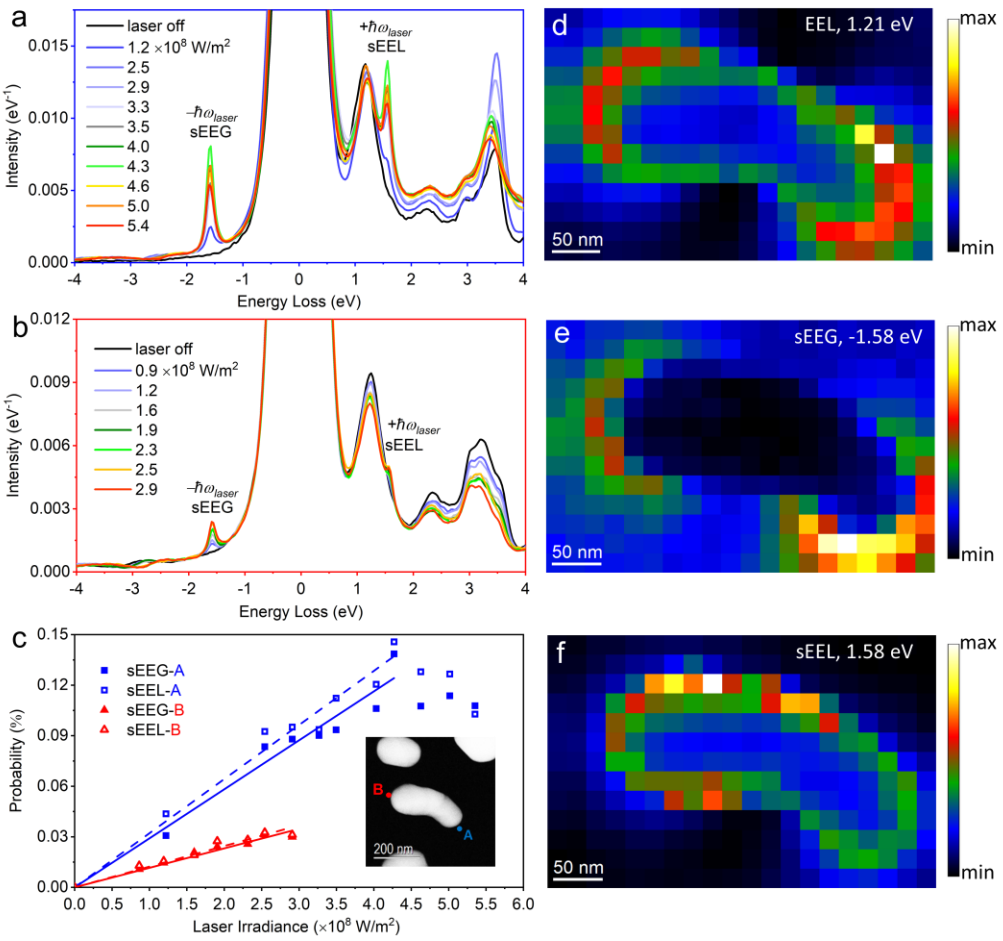

Fig. 5.5 sEEL and sEEG of a silver rod-like nanoparticle as a function of laser irradiance. Unprocessed low-loss EEL spectra of silver rod-like structures at (a), position A and (b), position B as a function of laser irradiance (×10^8 W/m^2) at the aloof beam position. The positions A and B are indicated in the inset of (c). (c), Integrated sEEG and sEEL probabilities as a function of laser irradiance. The solid (sEEG) and dashed (sEEL) lines are linear fits for the data obtained at position B (blue) and C (red), respectively. The solid and dashed lines are linear fits to the sEEG and sEEL data, respectively. EEL maps of (d), the 1.21 eV dipole peak at zero irradiance; (e), -1.58 eV sEEG map and (f), the +1.58 eV sEEL map, both at 2×10^8 W/m^2 irradiance.

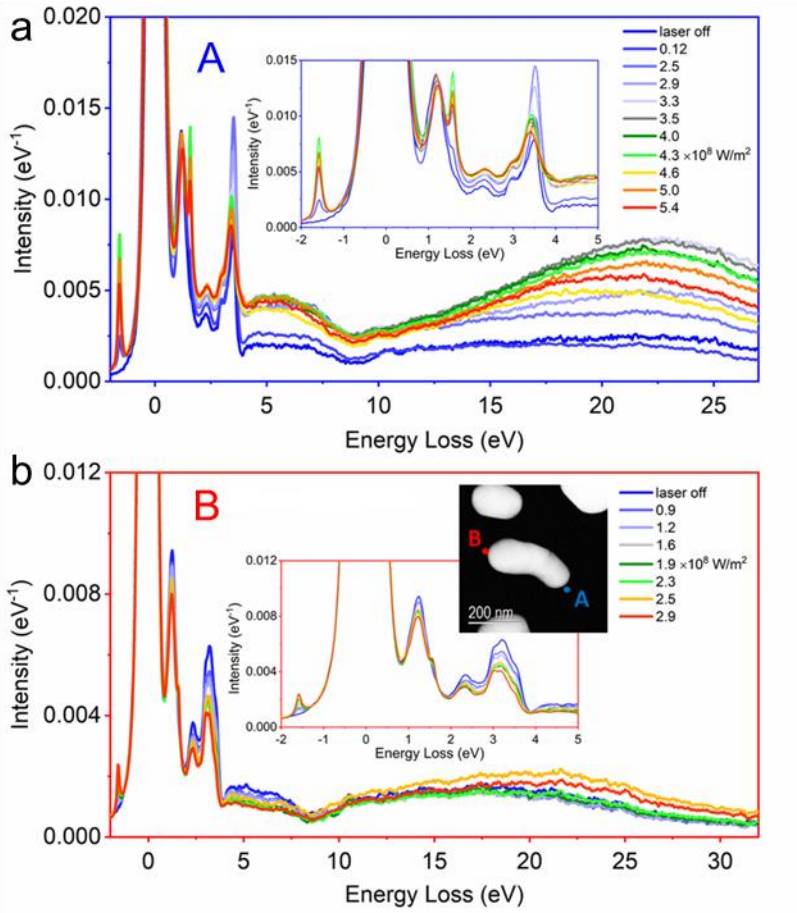

Fig. 5.6 The unprocessed low-loss EEL/EEG point spectra of a photothermally dewet silver nanoparticles as a function of laser irradiance (W/m^2) for the Positions A and B in Fig. 5.5 .

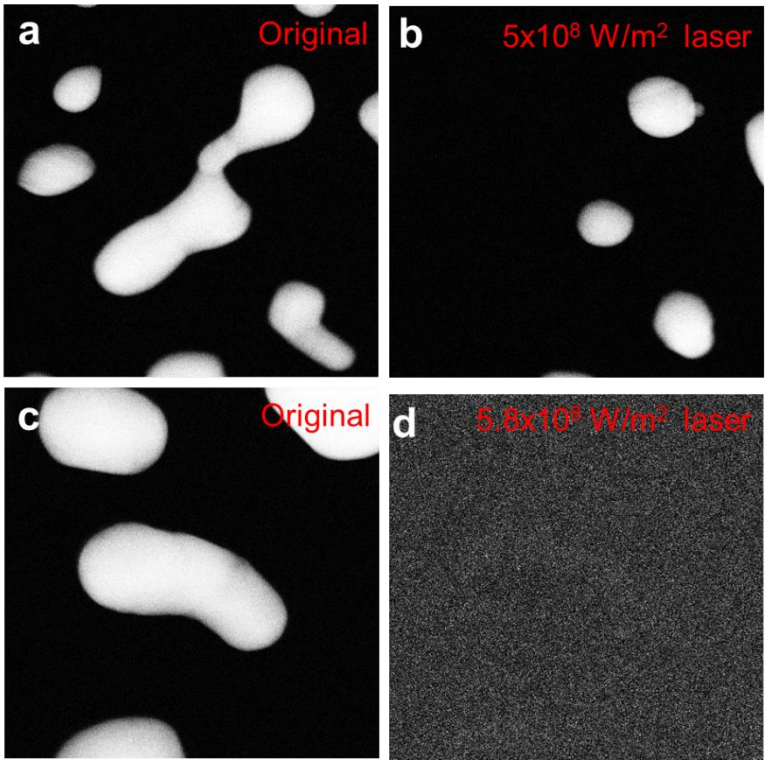

Fig. 5.7 HAADF images taken before laser heating (a) and (c), and after the nanoparticles were evaporated at (b), 5×10^8 W/m^2 and (d), 5.8×10^8 W/m^2 laser irradiation.

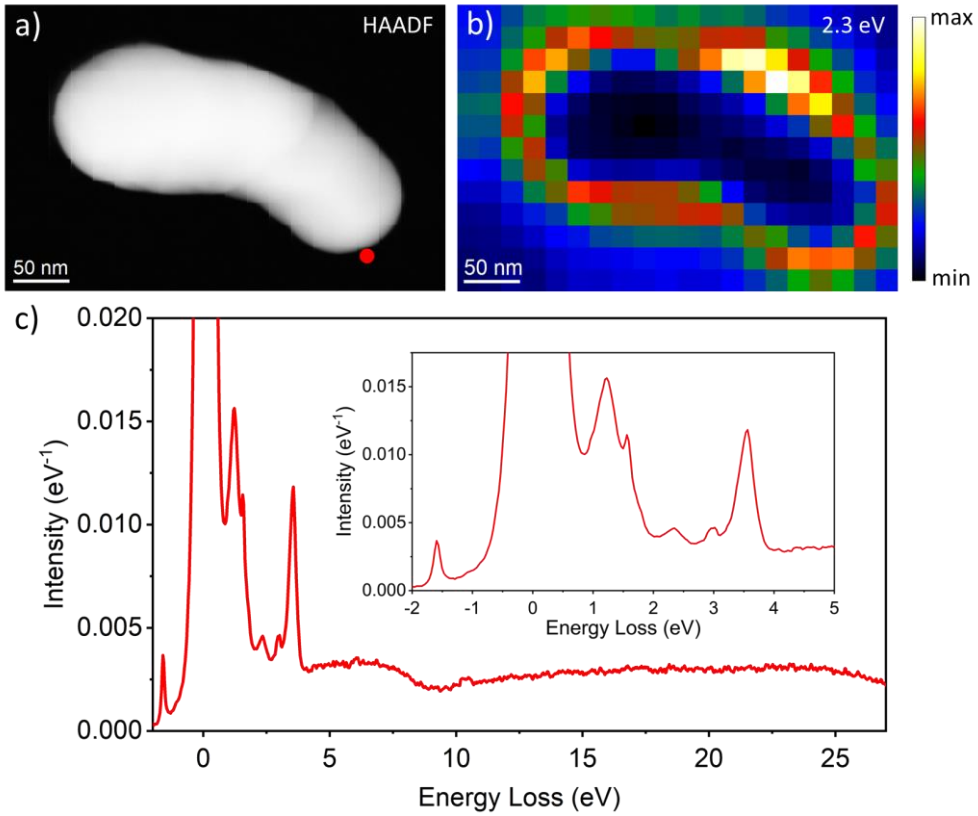

Fig. 5.8 (a), HAADF image of the bean shown in Figure 3b. (b), An EEL map of a 2.3 eV quadrupole mode excited in the bean. Note the SEEL probability map for the internal positions of the relatively thick silver contains a diffraction artifact thus they may be ignored as no modes exist for the internal position at this energy (yellow and white spots in b). (c), A representative single spectrum of red-dot pixel marked in a.

Table 5.5 Evolution of the probability (%) of every peak (eV) with increasing laser energy irradiance ($\times 10^8$ W/m^2) at Position A in Fig. 5.5.

	EEGS	0.702	1.209	SEELS	2.171	3.031	3.452	5.252	21
1.2	0.031	0	0.529	0.044	0.427	0.069	0.306	0.820	3.781
2.5	0.084	0.012	0.554	0.093	0.437	0.071	0.398	1.389	6.970
2.9	0.088	0.095	0.573	0.095	0.430	0.066	0.344	1.512	7.969
3.3	0.090	0.032	0.572	0.094	0.397	0.068	0.337	1.926	9.859
3.5	0.094	0.105	0.573	0.112	0.499	0.070	0.268	1.965	10.804
4.0	0.106	0.026	0.572	0.121	0.538	0.061	0.258	1.748	10.288
4.3	0.139	0.024	0.573	0.146	0.456	0.063	0.265	2.119	9.885
4.6	0.108	0.012	0.525	0.128	0.529	0.063	0.240	1.547	7.597
5.0	0.114	0.007	0.535	0.127	0.481	0.067	0.243	2.049	9.227
5.4	0.108	0.063	0.602	0.103	0.514	0.065	0.222	1.851	8.466

Table 5.6 Evolution of the position (eV) of every peak (eV) with increasing laser energy irradiance ($\times 10^8$ W/m^2) at Position A in Fig. 5.5.

	EEGS	0.702	1.209	SEELS	2.171	3.031	3.452	5.252	21
1.2	-1.574	0.77	1.23	1.582	2.19	3.02	3.48	5.31	17.86
2.5	-1.581	0.72	1.22	1.582	2.17	3.05	3.50	5.43	19.53
2.9	-1.579	0.55	1.20	1.582	2.13	3.04	3.49	5.21	21.37
3.3	-1.581	0.68	1.21	1.582	2.13	3.03	3.46	5.21	22.41
3.5	-1.581	0.63	1.18	1.582	2.11	3.02	3.43	5.21	22.29
4.0	-1.582	0.77	1.23	1.582	2.27	3.04	3.44	5.29	21.73
4.3	-1.584	0.70	1.21	1.582	2.16	3.02	3.43	5.21	22.13
4.6	-1.584	0.77	1.20	1.582	2.18	3.02	3.43	5.21	19.99
5.0	-1.584	0.77	1.21	1.582	2.17	3.04	3.44	5.21	21.72
5.4	-1.591	0.66	1.20	1.582	2.18	3.03	3.43	5.21	20.82

Table 5.7 Evolution of the FWHM (eV) of every peak (eV) with increasing laser energy irradiance ($\times 10^8$ W/m^2) at Position A in Fig. 5.5. Please note that the FWHM of EEGS and SEELS are the same as that of the zero-loss peak.

	EEGS	0.702	1.209	SEELS	2.171	3.031	3.452	5.252	21
1.2	0.13	0.19	0.48	0.13	1.26	0.31	0.37	3.98	20.57
2.5	0.13	0.19	0.51	0.13	1.43	0.31	0.34	4.43	23.44
2.9	0.15	0.23	0.55	0.15	1.43	0.31	0.36	4.79	22.80
3.3	0.13	0.23	0.55	0.13	1.43	0.31	0.37	5.17	21.35
3.5	0.15	0.23	0.55	0.15	1.43	0.31	0.39	4.83	19.23
4.0	0.13	0.19	0.55	0.13	1.43	0.31	0.39	4.29	18.77
4.3	0.13	0.23	0.55	0.13	1.43	0.31	0.39	5.16	18.89
4.6	0.15	0.19	0.51	0.15	1.43	0.31	0.39	4.48	17.80
5.0	0.14	0.23	0.49	0.14	1.43	0.31	0.39	4.98	18.74
5.4	0.15	0.23	0.55	0.15	1.43	0.31	0.39	4.76	17.94

Table 5.8 Evolution of the amplitude (eV^{-1}) of every peak (eV) with increasing laser energy irradiance ($\times 10^8$ W/m^2) at Position A in Fig. 5.5.

	EEGS	0.702	1.209	SEELS	2.171	3.031	3.452	5.252	21
1.2	0.0017	0	0.0105	0.0023	0.0032	0.0021	0.0078	0.0020	0.0021
2.5	0.0043	0.0006	0.0103	0.0048	0.0029	0.0022	0.0110	0.0030	0.0038
2.9	0.0044	0.0041	0.0099	0.0048	0.0029	0.0020	0.0092	0.0030	0.0047
3.3	0.0047	0.0014	0.0099	0.0049	0.0026	0.0021	0.0086	0.0036	0.0064
3.5	0.0047	0.0043	0.0099	0.0056	0.0033	0.0021	0.0066	0.0039	0.0075
4.0	0.0055	0.0013	0.0099	0.0062	0.0036	0.0019	0.0063	0.0039	0.0070
4.3	0.0074	0.0010	0.0099	0.0078	0.0030	0.0019	0.0065	0.0040	0.0069
4.6	0.0055	0.0006	0.0099	0.0065	0.0035	0.0020	0.0059	0.0033	0.0050
5.0	0.0060	0.0003	0.0105	0.0067	0.0032	0.0021	0.0060	0.0040	0.0063
5.4	0.0054	0.0026	0.0105	0.0052	0.0034	0.0020	0.0054	0.0037	0.0057

Table 5.9 Evolution of the probability (%) of every peak (eV) with increasing laser energy irradiance ($\times 10^8$ W/m^2) at Position B in Fig. 5.5.

	EEGS	1.248	SEELS	2.381	3.008	3.283	4.895	18.1
0.0	0	0.379	0	0.4741	0.0307	0.2089	0.4389	2.7592
0.9	0.0108	0.3895	0.0129	0.3784	0.03	0.2022	0.3968	2.4607
1.2	0.0146	0.3799	0.0156	0.3513	0.0226	0.2101	0.3836	2.4556
1.6	0.0208	0.3713	0.0192	0.3333	0.0226	0.1798	0.332	2.4356
1.9	0.0241	0.3464	0.0274	0.3232	0.0236	0.1539	0.3021	2.4775
2.3	0.0257	0.3622	0.0282	0.3256	0.0203	0.1633	0.3145	2.4686
2.5	0.0312	0.3538	0.0325	0.3115	0.0137	0.1798	0.3262	3.4656
2.9	0.0299	0.3169	0.0312	0.3654	0.0193	0.1121	0.2789	2.891

Table 5.10 Evolution of the position (eV) of every peak (eV) with increasing laser energy irradiance ($\times 10^8$ W/m^2) at Position B in Fig. 5.5.

	EEGS	1.248	SEELS	2.381	3.008	3.283	4.895	18.1
0.0	NULL	1.25	NULL	2.45	3.01	3.31	5.16	17.57
0.9	-1.596	1.23	1.582	2.39	3.01	3.31	4.98	17.28
1.2	-1.585	1.27	1.582	2.38	3.00	3.29	4.96	17.28
1.6	-1.578	1.24	1.582	2.34	3.00	3.29	4.82	17.92
1.9	-1.581	1.27	1.582	2.42	3.01	3.30	4.84	17.81
2.3	-1.575	1.23	1.582	2.34	3.01	3.28	4.79	18.29
2.5	-1.583	1.25	1.582	2.34	3.03	3.24	4.80	19.31
2.9	-1.582	1.25	1.582	2.38	3.00	3.25	4.83	19.37

Table 5.11 Evolution of the FWHM (eV) of every peak (eV) with increasing laser energy irradiance ($\times 10^8$ W/m^2) at Position B in Fig. 5.5. Please note that the FWHM of EEGS and SEELS are the same as that of the zero-loss peak.

	EEGS	1.248	SEELS	2.381	3.008	3.283	4.895	18.1
0.0	0.13	0.50	0.13	1.65	0.19	0.50	3.68	18.48
0.9	0.15	0.51	0.15	1.39	0.19	0.53	3.68	18.48
1.2	0.13	0.50	0.13	1.35	0.19	0.55	3.68	18.48
1.6	0.13	0.50	0.13	1.35	0.19	0.54	3.68	18.48
1.9	0.13	0.50	0.13	1.35	0.19	0.53	3.68	18.48
2.3	0.15	0.50	0.15	1.35	0.19	0.53	3.68	18.48
2.5	0.13	0.50	0.13	1.35	0.19	0.59	3.68	19.11
2.9	0.13	0.50	0.13	1.65	0.19	0.49	3.68	18.63

Table 5.12 Evolution of the amplitude (eV^{-1}) of every peak (eV) with increasing laser energy irradiance ($\times 10^8$ W/m^2) at Position B in Fig. 5.5.

	EEGS	1.248	SEELS	2.381	3.008	3.283	4.895	18.1
0.0	0	0.0073	0	0.0028	0.0015	0.0040	0.0011	0.0016
0.9	0.0006	0.0073	0.0007	0.0026	0.0015	0.0037	0.0010	0.0014
1.2	0.0008	0.0073	0.0008	0.0025	0.0011	0.0037	0.0010	0.0014
1.6	0.0011	0.0072	0.0010	0.0024	0.0011	0.0032	0.0009	0.0015
1.9	0.0013	0.0067	0.0015	0.0023	0.0012	0.0027	0.0008	0.0015
2.3	0.0014	0.0069	0.0015	0.0023	0.0010	0.0029	0.0008	0.0015
2.5	0.0017	0.0069	0.0017	0.0022	0.0007	0.0029	0.0008	0.0021
2.9	0.0016	0.0062	0.0017	0.0021	0.0010	0.0022	0.0007	0.0018

5.2 A theoretical description of sEEL and sEEG

This theoretical description was performed by David J. Masiello, Zhongwei Hu, and Jacob A. Busche. According to Das et al.,[143] at low laser intensities where the stimulated sEELS and sEEGS intensities are on the order of the spontaneous EELS intensity, the mean number of stimulated plasmons (M) can be deduced by taking a ratio of the spontaneous plus stimulated loss intensity to the stimulated gain intensity, where this ratio is equal to (M+1)/M. Based on the deconvolved spectra that includes only the longitudinal dipole peak (at 1.2 eV) and the stimulated gain (at -1.58 eV) and loss (at 1.58eV) peaks, the experimental peak integrated intensities were determined from Fig. 5.5a spectra collected at 1.2, 2.5 and $4\text{x}10^8$ W/m^2 irradiance. The experimental ratios were determined to be 24.1, 10.5, and 8.7, respectively; thus the mean number of photoexcited plasmons at these irradiances were estimated to be 0.04, 0.10, and 0.13, respectively.

Due to the weak interaction of light with matter and the low cw laser intensity and (S)TEM electron current used herein, the spectral signatures of sEEL and sEEG can be well understood using time-dependent perturbation theory up to second order in electron-plasmon and photon-plasmon interactions. Each of these interactions either reduce or increase the (S)TEM electron momentum from $\hbar k_i$ to $\hbar k_f = \hbar k_i - \hbar q$, with $\hbar q$ a small ($|\hbar q| \ll \hbar k_i$) transfer momentum that is positive in energy-loss events and negative in energy-gain events.

In both cases, the cw laser and nanoparticle plasmons are assumed to have reached a steady state prior to the electron-plasmon interaction. Additionally, we choose the the initial population $M_\lambda(\omega) = M_\lambda^{\max} \frac{\gamma_{\text{laser}}^2}{(\omega - \omega_{\text{laser}})^2 + \gamma_{\text{laser}}^2}$ of each plasmon state λ to be frequency-dependent to model the excitation of a continuous plasmon density of states by a laser of linewidth γ_{laser} and peak frequency ω_{laser}. Letting the laser polarization and longitudinal dipole plasmon be oriented along the x-axis, the longitudinal plasmon occupation number is $M_x(\omega) \geq 0$ such that the initial state of the three dipole plasmons is $|M_x(\omega), 0_y, 0_z\rangle$, with the occupation numbers of the

undriven transverse (y, z) plasmons taken to be zero. The initial state of the laser-populated photon field is given by the collective photon state $|\{N\}\rangle = |\ldots, N_\alpha, N_{\alpha'}, N_{\alpha''}, \ldots\rangle$, with α the collective index of each photon mode and N_α the occupation number of the α^{th} photon mode. Additionally, the initial state of the (S)TEM electron, whose motion along directions perpendicular to its propagation axis can be safely neglected for sufficiently small q, is well-approximated as a box-quantized, one-dimensional free particle with a wavefunction $\langle \boldsymbol{r}|k_i\rangle = \phi_R(\boldsymbol{R})\exp(\mathrm{i}k_i z)/\sqrt{L}$. Here, $\boldsymbol{R}$ is the cylindrical radial vector and $|\phi_R(\boldsymbol{R})| \approx \delta(\boldsymbol{R} - \boldsymbol{R}_0)$, with $\boldsymbol{R}_0$ the impact parameter of the electron.[68] To be consistent with the definition of the photon field, the electron wavefunction is described in second quantization as $|k_i\rangle = |\ldots, 0, 1_{k_i}, 0, \ldots\rangle$, with all modes having an occupation number of zero except the k_i^{th} state of momentum $\hbar k_i$ which has an occupation number of one.

Collectively, the initial state of the system is then $|i\rangle = |k_i, \{N\}, \{M_x(\omega), 0_y, 0_z\}\rangle$, and the allowed final states are determined by the electron-plasmon and photon-plasmon coupling, $\widehat{H}_{el-pl} = -\hat{\mathbf{d}} \cdot \hat{\mathbf{E}}_{el} = \sum_{kk'\lambda}(g_{k'k\lambda}\hat{c}_{k'}^{\dagger}\hat{c}_k\hat{b}_\lambda^{\dagger} + g_{k'k\lambda}^{*}\hat{c}_k^{\dagger}\hat{c}_{k'}\hat{b}_\lambda)$ and $\widehat{H}_{ph-pl} = -\hat{\mathbf{d}} \cdot \hat{\mathbf{E}}_{ph} = \sum_{\alpha\lambda} g_{\alpha\lambda}(\hat{b}_\lambda^{\dagger}\hat{a}_\alpha - \hat{b}_\lambda\hat{a}_\alpha^{\dagger})$, with $\lambda = x, y, z$ labeling the three nanoparticle dipole plasmons and $\hat{\mathbf{E}}_{el}$ and $\hat{\mathbf{E}}_{ph}$ the time-dependent electric field operators of the electron and photon fields. Here, $\hat{\mathbf{d}} = \sum_\lambda d_\lambda(\hat{b}_\lambda + \hat{b}_\lambda^{\dagger})\mathbf{e}_\lambda$ is the transition dipole operator of the dipole plasmon modes of the rod with $\hat{b}_\lambda$ the annihilation operator of the dipole plasmon oriented in the λ-direction, denoted by the unit vector $\mathbf{e}_\lambda$. Analogously, $\hat{a}_\alpha$ and $\hat{c}_k$ are the annihilation operators of the α^{th} photon mode and k^{th} electron mode, respectively. The coupling strengths $g_{k'k\lambda} = -\frac{2e|k'-k|d_\lambda}{\gamma^2 L}\kappa_\lambda\left(\frac{|k'-k|R_0}{\gamma}\right)$ and $g_{\alpha\lambda} = -\mathrm{i}\sqrt{\frac{2\pi\hbar\omega_\alpha}{V}}d_\lambda(\mathbf{e}_\lambda \cdot \boldsymbol{\epsilon}_\alpha)$, in which $\kappa_{x,y}\left(\frac{|k'-k|R_0}{\gamma}\right) = -\gamma K_1\left(\frac{|k'-k|R_0}{\gamma}\right)\frac{\mathbf{R}_0\cdot\mathbf{e}_{x,y}}{R_0}$ and $\kappa_z\left(\frac{|k'-k|R_0}{\gamma}\right) = -\mathrm{i}\frac{k'-k}{|k'-k|}K_0\left(\frac{|k'-k|R_0}{\gamma}\right)$, depend upon the

radiation mode frequencies ω_α, polarizations $\boldsymbol{\epsilon}_\alpha$, and quantization volume V, as well as the Lorentz contraction factor γ and quantization length L.

Inspection of the different allowed time orderings of $\hat{H}_{el-pl}$ and $\hat{H}_{ph-pl}$ within the calculation of a second-order transition rate from $|i\rangle = |k_i, \{N\}, \{M_x(\omega), 0_y, 0_z\}\rangle$, to $|f\rangle = |k_f, \{N'\}, \{M'_x(\omega), M'_y, M'_z\}\rangle$, reveals that only four second-order scattering processes contribute: the plasmon may gain (simultaneous plasmon excitation (SPE)) or lose (simultaneous plasmon deexcitation (SPD)) two quanta of energy during the interaction, or it may simply mediate energy transfer from the photon field to the electron probe (stimulated electron energy-gain (sEEG)) or vice versa (stimulated electron-induced emission of radiation (sEIRE)).

Of the four processes, only SPE and sEIRE can contribute to the total loss signal. As SPE is the stimulated analog of the more commonly known EEL process, one might expect its contribution to the loss signal to be of prime importance. The transition rate for SPE is given by

$$w_{\mathrm{SPE}}^{(2)} = \frac{2\pi}{\hbar}\left|\sum_m \frac{\langle k_f, \{\dots, N_\alpha - 1, \dots\}, \{M_x(\omega)+2, 0_y, 0_z\}|\hat{H}_{el-pl}|m\rangle\langle m|\hat{H}_{ph-pl}|k_i, \{N\}, \{M_x(\omega), 0_y, 0_z\}\rangle}{E_i - E_m} + \sum_{m'} \frac{\langle k_f, \{\dots, N_\alpha - 1, \dots\}, \{M_x(\omega)+2, 0_y, 0_z\}|\hat{H}_{ph-pl}|m'\rangle\langle m'|\hat{H}_{el-pl}|k_i, \{N\}, \{M_x(\omega), 0_y, 0_z\}\rangle}{E_i - E_{m'}}\right|^2 \delta(E_f - E_i), \quad (5.1)$$

wherein the first term describes the properly time-ordered single-electron and single-photon interaction with the initial plasmon state $|\{M_x(\omega), 0_y, 0_z\}\rangle$, leaving the (S)TEM electron decelerated ($q > 0$) by interaction with the excited surface plasmon. The second represents the improper time-ordering of the two interactions, in which the electron scattering precedes the absorption of a photon. While not intuitive, the fact that both time orderings contribute to this scattering process (as opposed to the strictly causal interactions) has been discussed extensively in the literature.[144-146] Remarkably, the addition of the two oppositely time-ordered terms in equation (5.1) results in a transition rate of zero. As a result, the second-order contribution to the total loss signal is completely determined by

the rate of the sEIRE process as demonstrated below, with SPE providing no contribution.

Analyzing the two possible gain processes, SPD and sEEG, one can show that the transition rate of SPD,

$$w_{\mathrm{SPD}}^{(2)} = \frac{2\pi}{\hbar}\left|\sum_{m}\frac{\langle k_f,\{\dots,N_\alpha+1,\dots\},\{M_x(\omega)-2,0_y,0_z\}|\widehat{H}_{el-pl}|m\rangle\langle m|\widehat{H}_{ph-pl}|k_i,\{N\},\{M_x(\omega),0_y,0_z\}\rangle}{E_i-E_m}\right. + \left.\sum_{m'}\frac{\langle k_f,\{\dots,N_\alpha+1,\dots\},\{M_x(\omega)-2,0_y,0_z\}|\widehat{H}_{ph-pl}|m'\rangle\langle m'|\widehat{H}_{el-pl}|k_i,\{N\},\{M_x(\omega),0_y,0_z\}\rangle}{E_i-E_{m'}}\right|^2 \delta(E_f-E_i), \tag{5.2}$$

is also zero by similar reasoning. Therefore, the second-order contributions to the total loss and gain signals are entirely described by the transition rates $w_{\mathrm{sEIRE}}^{(2)}$ and $w_{\mathrm{sEEG}}^{(2)}$, respectively, which describe the likelihood that the (S)TEM electron and a photon will interact simultaneously with the plasmon causing a deceleration and acceleration of the electron, respectively. These transition rates can be calculated as

$$w_{\mathrm{sEIRE}}^{(2)} = \frac{2\pi}{\hbar}\left|\sum_{m}\frac{\langle k_f,\{\dots,N_\alpha+1,\dots\},\{M_x(\omega),0_y,0_z\}|\widehat{H}_{el-pl}|m\rangle\langle m|\widehat{H}_{ph-pl}|k_i,\{N\},\{M_x(\omega),0_y,0_z\}\rangle}{E_i-E_m}\right. + \left.\sum_{m'}\frac{\langle k_f,\{\dots,N_\alpha+1,\dots\},\{M_x(\omega),0_y,0_z\}|\widehat{H}_{ph-pl}|m'\rangle\langle m'|\widehat{H}_{el-pl}|k_i,\{N\},\{M_x(\omega),0_y,0_z\}\rangle}{E_i-E_{m'}}\right|^2 \delta(E_f-E_i), \tag{5.3}$$

$$w_{\mathrm{sEEG}}^{(2)} = \frac{2\pi}{\hbar}\left|\sum_{m}\frac{\langle k_f,\{\dots,N_\alpha-1,\dots\},\{M_x(\omega),0_y,0_z\}|\widehat{H}_{el-pl}|m\rangle\langle m|\widehat{H}_{ph-pl}|k_i,\{N\},\{M_x(\omega),0_y,0_z\}\rangle}{E_i-E_m}\right. + \left.\sum_{m'}\frac{\langle k_f,\{\dots,N_\alpha-1,\dots\},\{M_x(\omega),0_y,0_z\}|\widehat{H}_{ph-pl}|m'\rangle\langle m'|\widehat{H}_{el-pl}|k_i,\{N\},\{M_x(\omega),0_y,0_z\}\rangle}{E_i-E_{m'}}\right|^2 \delta(E_f-E_i) \tag{5.4}$$

with $k_f < k_i$ in $w_{\mathrm{sEIRE}}^{(2)}$ and $k_f > k_i$ in $w_{\mathrm{sEEG}}^{(2)}$. It is straightforward to show that the second-order sEEG transition rate recovers the same result given in Ref.[68] with $M_x(\omega) \to 0$, as the second (improper) term of equation (5.4) becomes zero. However, even at finite $M_x(\omega)$, both $w_{\mathrm{sEEG}}^{(2)}$ and $w_{\mathrm{sEIRE}}^{(2)}$ turn out to be independent of the initial plasmon occupation number and $w_{\mathrm{sEEG}}^{(2)}$ agrees with previous work for

any $M_x(\omega)$. It is also important to note that even though sEIRE photons are not detected in our experiment, equation (5.3) nonetheless shows that the loss signatures of the sEIRE process are encoded in the final electron energy spectrum.

In addition to the second-order contributions to the total loss rate, the fast electron probe can also lose or gain energy by interacting with the laser-excited plasmon mode *without* the simultaneous creation or destruction of a photon. The rates of these phenomena are calculated at first order. In the case of energy loss, the electron can further lose energy to modes beyond those that are pumped by the laser such that the total first-order energy loss rate of all three plasmons is $w_{\mathrm{EEL}} + w^{(1)}_{\mathrm{sEEL}} = \sum_\lambda \frac{2\pi}{\hbar} \left|\langle k_f,\ \{N\},\ \{\dots, M_\lambda(\omega)+1, \dots\} \middle| \widehat{H}_{el-pl} \middle| k_i,\ \{N\},\ \{M_x(\omega), 0_y, 0_z\}\rangle\right|^2 \delta(E_f - E_i)$, with w_{EEL} the well-known spontaneous EEL rate and $w^{(1)}_{\mathrm{sEEL}}$ the first-order stimulated EEL rate. Therefore, $w^{(1)}_{\mathrm{sEEL}}$ and w_{EEL} must be added to $w^{(2)}_{\mathrm{sEIRE}}$ to reconstruct the total loss spectrum measured in our experiment.

Similarly, the total first-order contribution to the gain rate is $w^{(1)}_{\mathrm{sEEG}} = \frac{2\pi}{\hbar} \left|\langle k_f,\ \{N\},\ \{M_x(\omega)-1, 0_y, 0_z\} \middle| \widehat{H}_{el-pl} \middle| k_i,\ \{N\},\ \{M_x(\omega), 0_y, 0_z\}\rangle\right|^2 \delta(E_f - E_i)$ which, in contrast to the first-order loss rate, contains no spontaneous contributions. It is thus clear that the total gain signal, $w^{(1)}_{\mathrm{sEEG}} + w^{(2)}_{\mathrm{sEEG}}$, is entirely caused by the sEEG process, allowing the label “total gain” to be dropped. Similarly dropping the label “total loss” in favor of sEEL now that all loss processes are accounted for, the sEEL and sEEG functions can be expressed in the following intuitive forms,

$$\Gamma_{\mathrm{sEEL}}(\omega) \approx \Gamma_{\mathrm{EEL}}(\omega) + \left(M_x(\omega) + \frac{\pi}{2\hbar\omega_x}\sigma_x(\omega_x)\mathcal{I}(\omega)\right)\Gamma_{\mathrm{EELx}}(\omega) \tag{5.5}$$

$$\Gamma_{\mathrm{sEEG}}(\omega) = \left(M_x(-\omega) + \frac{\pi}{2\hbar\omega_x}\sigma_x(\omega_x)\mathcal{I}(-\omega)\right)\Gamma^{(-)}_{\mathrm{EELx}}(\omega), \tag{5.6}$$

which are simply related to the sum of the individual rates[68] over the full spectrum of possible final states of the electron probe and photon field and are expressed in units of percent per unit loss/gain energy. Specifically, $\Gamma_{\mathrm{EELx}}(\omega)$ is a measure of EEL to *only* the longitudinal dipole plasmon with natural frequency

$\Omega_x = \omega_x - \mathrm{i}\gamma_x(\omega)$ while $\Gamma_{\mathrm{EEL}}(\omega)$ is simply the sum of the EEL contributions from all three dipolar plasmons modes. $\mathcal{I}(\omega)$ is the spectral intensity, measured in units of intensity per unit frequency of the cw laser source and $\sigma_x(\omega)$ is the extinction cross section of the longitudinal dipole plasmon. In equation (5.6), the superscript $(-)$ indicates that the EELx function of equation (5.5) has been reflected across $\omega = 0$ such that the sEEG signal appears at negative frequencies. Explicitly, $\Gamma_{\mathrm{EELx}}(\omega) = \frac{4e^2\omega^2}{\pi\hbar^2 v^4\gamma^4}\left[\frac{\gamma^2(\boldsymbol{R_0}\cdot\mathbf{e}_x)^2}{R_0^2}K_1^2\left(\frac{|\omega|R}{v\gamma}\right)\right]\mathrm{Im}\{\alpha_x(\omega)\}$, with $\alpha_x(\omega) = d_x^2/(\hbar\Omega_{\mathrm{x}} - \hbar\omega)$; the expression for $\Gamma_{\mathrm{EELx}}^{(-)}(\omega)$ can then be acquired by letting $\omega \to -\omega$.

For sufficiently narrow laser linewidths, equations (5.5) and (5.6) can be simplified by letting $\mathcal{I}(\omega)\Gamma_{\mathrm{EELx}}(\omega) \to I_{\mathrm{laser}}\frac{1}{\pi}\frac{\gamma_{\mathrm{laser}}}{(\omega-\omega_{\mathrm{laser}})^2+\gamma_{\mathrm{laser}}^2}\Gamma_{\mathrm{EELx}}(\omega_{\mathrm{laser}})$ and $\mathcal{I}(-\omega)\Gamma_{\mathrm{EELx}}^{(-)}(\omega) \to I_{\mathrm{laser}}\frac{1}{\pi}\frac{\gamma_{\mathrm{laser}}}{(-\omega-\omega_{\mathrm{laser}})^2+\gamma_{\mathrm{laser}}^2}\Gamma_{\mathrm{EELx}}^{(-)}(-\omega_{\mathrm{laser}})$, respectively, with I_{laser} the peak laser irradiance, giving

$$\Gamma_{\mathrm{sEEL}}(\omega) \approx \Gamma_{\mathrm{EEL}}(\omega) + M_x(\omega)\Gamma_{\mathrm{EELx}}(\omega) + \left(\frac{\sigma_x(\omega_x)I_{\mathrm{laser}}}{2\hbar\omega_x}\frac{N+1}{N}\frac{\gamma_{\mathrm{laser}}}{(\omega-\omega_{\mathrm{laser}})^2+\gamma_{\mathrm{laser}}^2}\right)\Gamma_{\mathrm{EELx}}(\omega_{\mathrm{laser}}) \quad (5.7)$$

and

$$\Gamma_{\mathrm{sEEG}}(\omega) \approx M_x(-\omega)\Gamma_{\mathrm{EELx}}^{(-)}(\omega) + \frac{\sigma_x(\omega_x)I_{\mathrm{laser}}}{2\hbar\omega_{\mathrm{x}}}\frac{\gamma_{\mathrm{laser}}}{(-\omega-\omega_{\mathrm{laser}})^2+\gamma_{\mathrm{laser}}^2}\Gamma_{\mathrm{EELx}}^{(-)}(-\omega_{\mathrm{laser}}) \quad (5.8)$$

Here N is the occupation number of the single cw laser mode modeled in the narrow-width limit. Note that for large N, the sEEL and sEEG functions become equivalent, up to the magnitude of the EEL signal, at each $\pm\omega$. Note also that sEEL reduces to EEL while sEEG vanishes in the limit where the laser irradiance (and therefore $M_x(\omega)$) is reduced to zero. These expressions, while approximate, make explicit the dependence of sEEL and sEEG upon optical extinction and EELS and provide a simple route to computing sEEL and sEEG spectra using continuum optical and electron scattering codes like the DDA,[147, 148] MNPBEM,[149] and e-DDA.[150, 151]

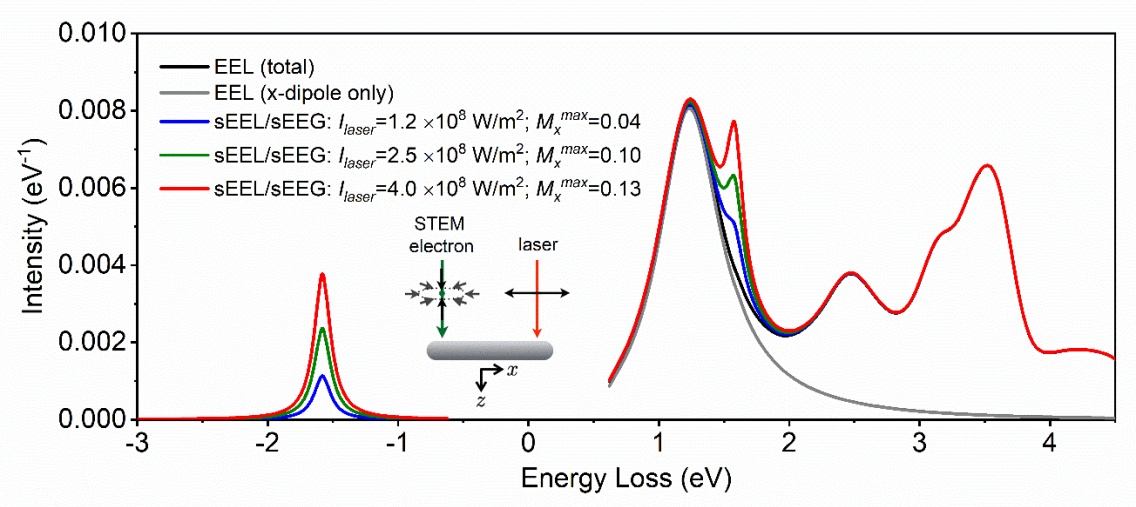

Fig. 5.9 Computed total loss and gain spectra of a silver nanorod interacting with the pair of co-propagating cw laser and STEM-electron beams illustrated in the inset. The simulated EEL spectrum is also shown for reference and is the limiting behavior of the sEEL signal when the laser field is removed. The sEEL and sEEG profiles are symmetrically distributed at $\pm\hbar\omega_{laser} = \pm 1.58$ eV and, after subtracting the EEL spectral profile, are otherwise of equal amplitude up to a factor of $(N+1)/N$. The sEEL and sEEG spectra were calculated with an electron beam impact parameter of 107 nm and a plasmon effective mass of 1.6×10^{-34} g. Additionally, the theoretical curves were calculated with a maximum plasmon occupation number of $M_x^{\max}$ of 0.04, 0.10, and 0.13, which are extracted from the measured I_{laser} = 1.2, 2.5, and $4.0\text{x}10^8$ W/m^2 spectra in Fig. 5.5a together with Eqs. (5.7-5.8). Finally, all curves were convolved with a normalized Lorentzian distribution with a FWHM of 150 meV to model the finite energy resolution of the instrument.

Fig. 5.9 shows the theoretical sEEL, sEEG, and EEL spectra calculated for a 321×120×120 nm^3 silver nanorod lying on a SiO_2 substrate in vacuum. Here, the electron beam and laser field co-propagate down an axis that is oriented normal to the long axis of the nanorod (see inset). The spectra are convolved pointwise with a normalized Lorentzian distribution of variance determined by the width of the ZLP (150 meV). Subtraction of the EEL spectrum from the sEEL spectrum would show that the stimulated gain and loss functions are nearly equivalent in amplitude as noted previously[68] with the difference arising only from the ratio $(N+1)/N$ that appears in $w_{\mathrm{sEIRE}}^{(2)}$. In the limit of large laser occupation numbers ($N+1 \approx N$), integration of the experimental sEEL and sEEG spectra of Fig. 4.3sa as well as the theory given in Equations 5.7 and 5.8 between 0 and ± 2 eV allows for the inference of $M_x^{\max}$. For peak laser intensities of 1.2, 2.5, and 4.0×10^8 W/m^2, the inferred maximum plasmon occupation numbers are 0.04, 0.10, and 0.13, respectively. Comparison of Fig. 5.9 and 5.3a highlights the remarkable quantitative agreement between the sEEG and sEEL peaks of experiment and theory. This supports the idea that the low intensity cs laser used in our experiment only weakly populates the nanoparticle plasmon mode, yet, we are still able to measure gain signal.

The experimental demonstration and theoretical underpinnings of low irradiance laser sEEL and sEEG illustrated here are an exciting first step in co-continuous electron and photon photoinduced nearfield electron microscopy using a monochromated STEM and high-resolution EELS. To extend the optical power range, higher thermal conductivity and smaller membranes could be used to enhance heat dissipation at high irradiance. Furthermore, multi-spectral cw photoexcited sEEL and sEEG would be possible by coupling other laser diode wavelengths to the single mode fiber, a project that is now underway. For instance, while EELS conveniently has access to the entire plasmonic spectrum, the combination of EELS and multi-spectral low-irradiance photoexcited sEEL and sEEG could distinguish between optically bright and dark modes as well as the

excited state internal field structure of the former. Thus we envision that the nearfield optical phenomena previously only visible with highly specialized UEMs will be accessible with a standard (S)TEM system equipped with the cw optical delivery source.[102]

5.3 Summary

In this chapter, we have demonstrated stimulated electron energy-loss and stimulated electron energy-gain spectroscopy with a continuous wave laser source and monochromated electron source in a (S)TEM. These signatures emerge at an irradiance value of $\sim 5\times10^{7}$ W/m^2 and increase approximately linearly to $\sim 5\times10^{8}$ W/m^2. Above this irradiance range, photothermal heating causes the sEEG and sEEL probability to decrease. sEEL and sEEG mapping of a rod-like silver nanostructure confirms that 1.58 eV photons couple to the bright longitudinal dipole plasmon mode. Analytical modeling of the simultaneous (S)TEM electron- and cw laser photon-plasmon interactions based on time-dependent perturbation theory demonstrates the connection between the total loss and gain spectra and the more intuitive optical extinction, laser intensity, and normal EEL spectrum. By exploiting this connection, model simulations of the sEEL and sEEG of an individual silver nanorod elucidate the fundamental processing underlying our experimental observations. The ability to visualize the field structure of excited state plasmons opens up new directions for optically-stimulated fast electron spectroscopy of electronically excited nanomaterials, such as, e.g., the direct testing of optoelectronic circuits. One can also imagine that coupled with a gas cell, plasmon-based sensors and catalytic reactions can be synchronously imaged and correlated to those modes that are bright. Importantly, the photon delivery instrument used in this study can be attached to practically any microscope and equipped with various light sources, thus providing a more universal approach to visualizing atomic scale nearfield phenomena that are critical to many photonic applications.

Chapter 6. Conclusions

In summary, capabilities of laser irradiation for real-time synthesis and characterization within the TEM were shown by synthesis of Van der Waals bilayer using *in situ* laser-induced heating, controllably formation of Janus WSSe using in situ diagnostics and characterization of plasmons using photon stimulated electron energy-gain.

Two-dimensional (2D) heteroepitaxial heterostructures were successfully synthesized via direct PLD of WSe_2 precursors at 600°C on monolayer $MoSe_2$, however, disoriented polycrystalline films were produced on graphene. The pathways for the assembly of both structures from amorphous precursors on $MoSe_2$ and on graphene are described from *in situ* TEM studies utilizing pulsed laser heating. Crystallization is observed to proceed through a series of metastable phases and changes in stoichiometry, with discrete thresholds, until a 1:2 W:Se ratio is observed, when a 2D layered crystal forms, as measured by *in situ* electron energy loss (EEL) experiments. *In situ* SAED and HRTEM imaging reveals significant recrystallization of nanodomains to form larger domains. In the early stage, crystallites nucleate homogenously with different orientations and begin to grow together. In the stage of post-nucleation growth, crystallization and coalescence are facilitated by a variety of competing processes, including Ostwald ripening, recrystallization, oriented attachment, translation, and rotation.

This non-equilibrium synthesis process permits materials of interest to be controllably implanted to different depths within atomically thin layers. The key to success in creating the Janus monolayers is tuning the kinetic energy of the plasma plume, which is controlled by slowing the plasma plume using argon gas in a pressure-controlled chamber. The relationship between the kinetic energy and the final structure of converted material is understood both experimentally and theoretically using first-principle calculation and molecular dynamics simulations. These results provide valuable insights to guide the bottom-up PLD synthesis of 2D materials and to develop hyperthermal implantation as a top-down method to

explore the synthesis of metastable 2D Janus layers and alloys of variable composition.

The most important factor determining domain size is the guiding role of the substrate, with graphene (25.8% lattice mismatch) produces disoriented polycrystalline films, while 2D $MoSe_2$ (0.4% lattice mismatch) guides the assembly to nearly single-crystalline films. These results, utilizing laser-annealing of amorphous precursors deposited by PLD at room temperature, are similar with the direct PLD of these precursors at 600°C. These experiments provide valuable insight on the mechanisms of 2D crystal growth by PLD, and more generally a method to explore and tailor the synthesis pathways from amorphous precursors to different phases utilizing *in situ* laser processing within a transmission electron microscope.

The non-equilibrium laser synthesis process using *in situ* diagnostics permits materials of interest to be controllably implanted to different depths within atomically thin layers. The key to success in creating the Janus monolayers is tuning the kinetic energy of the plasma plume, which is controlled by slowing the plasma plume using argon gas in a pressure-controlled chamber. The relationship between the kinetic energy and the final structure of converted material is understood using atomic resolution STEM technique. These results provide valuable insights to guide the bottom-up PLD synthesis of 2D materials and to develop hyperthermal implantation as a top-down method to explore the synthesis of metastable 2D Janus layers and alloys of variable composition.

For laser characterization in the TEM, we have demonstrated stimulated electron energy-loss and stimulated electron energy-gain spectroscopy with a continuous wave laser source and monochromated electron source in a (S)TEM. These signatures emerge at an irradiance value of $\sim 5\times10^7$ W/m^2 and increase approximately linearly to $\sim 5\times10^8$ W/m^2. Above this irradiance range, photothermal heating causes the sEEG and sEEL probability to decrease. sEEL and sEEG mapping of a rod-like silver nanostructure confirms that 1.58 eV photons couple to

the bright longitudinal dipole plasmon mode. Analytical modeling of the simultaneous (S)TEM electron- and cw laser photon-plasmon interactions based on time-dependent perturbation theory demonstrates the connection between the total loss and gain spectra and the more intuitive optical extinction, laser intensity, and normal EEL spectrum. By exploiting this connection, model simulations of the sEEL and sEEG of an individual silver nanorod elucidate the fundamental processing underlying our experimental observations. The ability to visualize the field structure of excited state plasmons opens up new directions for optically-stimulated fast electron spectroscopy of electronically excited nanomaterials, such as, e.g., the direct testing of optoelectronic circuits. One can also imagine that coupled with a gas cell, plasmon-based sensors and catalytic reactions can be synchronously imaged and correlated to those modes that are bright. Importantly, the photon delivery instrument used in this study can be attached to practically any microscope and equipped with various light sources, thus providing a more universal approach to visualizing atomic scale nearfield phenomena that are critical to many photonic applications.

LIST OF REFERENCES

[1] C. Buzea, I.I. Pacheco, K. Robbie, Nanomaterials and nanoparticles: sources and toxicity, Biointerphases 2 (2007) MR17-MR71.
[2] M.-C. Daniel, D. Astruc, Gold nanoparticles: assembly, supramolecular chemistry, quantum-size-related properties, and applications toward biology, catalysis, and nanotechnology, Chemical reviews 104 (2004) 293-346.
[3] M. Mahjouri-Samani, R. Gresback, M. Tian, K. Wang, A.A. Puretzky, C.M. Rouleau, G. Eres, I.N. Ivanov, K. Xiao, M.A. McGuire, G. Duscher, D.B. Geohegan, Pulsed Laser Deposition of Photoresponsive Two-Dimensional GaSe Nanosheet Networks, Adv. Funct. Mater. 24 (2014) 6365-6371.
[4] K.-K. Liu, W. Zhang, Y.-H. Lee, Y.-C. Lin, M.-T. Chang, C.-Y. Su, C.-S. Chang, H. Li, Y. Shi, H. Zhang, C.-S. Lai, L.-J. Li, Growth of Large-Area and Highly Crystalline MoS2 Thin Layers on Insulating Substrates, Nano Letters 12 (2012) 1538-1544.
[5] K. Tran, G. Moody, F. Wu, X. Lu, J. Choi, K. Kim, A. Rai, D.A. Sanchez, J. Quan, A. Singh, Evidence for moiré excitons in van der Waals heterostructures, Nature (2019) 1.
[6] C. Jin, E.C. Regan, A. Yan, M. Iqbal Bakti Utama, D. Wang, S. Zhao, Y. Qin, S. Yang, Z. Zheng, S. Shi, K. Watanabe, T. Taniguchi, S. Tongay, A. Zettl, F. Wang, Observation of moire excitons in WSe2/WS2 heterostructure superlattices, Nature 567 (2019) 76-80.
[7] K. Wang, B. Huang, M. Tian, F. Ceballos, M.-W. Lin, M. Mahjouri-Samani, A. Boulesbaa, A.A. Puretzky, C.M. Rouleau, M. Yoon, H. Zhao, K. Xiao, G. Duscher, D.B. Geohegan, Interlayer Coupling in Twisted WSe_2/WS_2 Bilayer Heterostructures Revealed by Optical Spectroscopy, ACS Nano 10 (2016) 6612-6622.
[8] Y.C. Lin, C. Liu, Y. Yu, E. Zarkadoula, M. Yoon, A.A. Puretzky, L. Liang, X. Kong, Y. Gu, A. Strasser, H.M. Meyer, 3rd, M. Lorenz, M.F. Chisholm, I.N. Ivanov, C.M. Rouleau, G. Duscher, K. Xiao, D.B. Geohegan, Low Energy Implantation into

Transition-Metal Dichalcogenide Monolayers to Form Janus Structures, ACS Nano 14 (2020) 3896-3906.
[9] R.H. Ritchie, Plasma Losses by Fast Electrons in Thin Films, Physical Review 106 (1957) 874-881.
[10] P. Pattnaik, Surface plasmon resonance, Applied Biochemistry and Biotechnology 126 (2005) 79-92.
[11] S. Linic, P. Christopher, D.B. Ingram, Plasmonic-metal nanostructures for efficient conversion of solar to chemical energy, Nat Mater 10 (2011) 911-21.
[12] G. Li, C. Cherqui, Y. Wu, N.W. Bigelow, P.D. Simmons, P.D. Rack, D.J. Masiello, J.P. Camden, Examining Substrate-Induced Plasmon Mode Splitting and Localization in Truncated Silver Nanospheres with Electron Energy Loss Spectroscopy, J Phys Chem Lett 6 (2015) 2569-76.
[13] P. Cheben, R. Halir, J.H. Schmid, H.A. Atwater, D.R. Smith, Subwavelength integrated photonics, Nature 560 (2018) 565-572.
[14] M. Salerno, J.R. Krenn, B. Lamprecht, G. Schider, H. Ditlbacher, N. Félidj, A. Leitner, F.R. Aussenegg, Plasmon polaritons in metal nanostructures: the opto-electronic route to nanotechnology, Opto-electronics review 10 (2002) 217-224.
[15] Z. Liang, J. Sun, Y. Jiang, L. Jiang, X. Chen, Plasmonic Enhanced Optoelectronic Devices, Plasmonics 9 (2014) 859–866.
[16] T.J. Davis, D.E. Gómez, A. Roberts, Plasmonic circuits for manipulating optical information, Nanophotonics 6 (2017) 543–559.
[17] H. Wei, Z. Wang, X. Tian, M. Käll, H. Xu, Cascaded logic gates in nanophotonic plasmon networks, Nature Communications 2 (2011) 387.
[18] S.I. Bozhevolnyi, N. Asger Mortensen, Plasmonics for emerging quantum technologies, Nanophotonics 6 (2017) 1185–1188.
[19] M.L. Andersen, S. Stobbe, A.S. Sørensen, P. Lodahl, Strongly modified plasmon–matter interaction with mesoscopic quantum emitters, Nature Physics 7 (2010) 215.

[20] J. Homola, S.S. Yee, G. Gauglitz, Surface plasmon resonance sensors: review, Sensors and Actuators B: Chemical 54 (1999) 3-15.
[21] P.C. Ray, Size and Shape Dependent Second Order Nonlinear Optical Properties of Nanomaterials and Their Application in Biological and Chemical Sensing, Chemical Reviews 110 (2010) 5332-5365.
[22] L.-Y. Hsu, W. Ding, G.C. Schatz, Plasmon-Coupled Resonance Energy Transfer, The Journal of Physical Chemistry Letters 8 (2017) 2357-2367.
[23] J. Li, S.K. Cushing, F. Meng, T.R. Senty, A.D. Bristow, N. Wu, Plasmon-induced resonance energy transfer for solar energy conversion, Nature Photonics 9 (2015) 601.
[24] C. Clavero, Plasmon-induced hot-electron generation at nanoparticle/metal-oxide interfaces for photovoltaic and photocatalytic devices, Nature Photonics 8 (2014) 95.
[25] R. Sundararaman, P. Narang, A.S. Jermyn, W.A. Goddard Iii, H.A. Atwater, Theoretical predictions for hot-carrier generation from surface plasmon decay, Nature Communications 5 (2014) 5788.
[26] M.L. Brongersma, N.J. Halas, P. Nordlander, Plasmon-induced hot carrier science and technology, Nature Nanotechnology 10 (2015) 25.
[27] J.A. Scholl, A.L. Koh, J.A. Dionne, Quantum plasmon resonances of individual metallic nanoparticles, Nature 483 (2012) 421-427.
[28] R. Sachan, A. Malasi, J. Ge, S. Yadavali, H. Krishna, A. Gangopadhyay, H. Garcia, G. Duscher, R. Kalyanaraman, Ferroplasmons: intense localized surface plasmons in metal-ferromagnetic nanoparticles, ACS Nano 8 (2014) 9790-8.
[29] K.C. Phillips, H.H. Gandhi, E. Mazur, S.K. Sundaram, Ultrafast laser processing of materials: a review, Advances in Optics and Photonics 7 (2015).
[30] J.M. Liu, R. Yen, H. Kurz, N. Bloembergen, Phase transformation on and charged particle emission from a silicon crystal surface, induced by picosecond laser pulses, Applied Physics Letters 39 (1981) 755-757.

[31] S. Sundaram, E. Mazur, Inducing and probing non-thermal transitions in semiconductors using femtosecond laser pulses, Nature materials 1 (2002) 217.
[32] C. Dorman, M. Schulze, Picosecond Micromachining Update: Unique fiber‐based laser technology delivers high pulse energy and average power, Laser Technik Journal 5 (2008) 44-47.
[33] D.B. Geohegan, A.A. Puretzky, A. Boulesbaa, G. Duscher, G. Eres, X. Li, L. Liang, M. Mahjouri-Samani, C. Rouleau, W. Tennyson, Laser Synthesis, Processing, and Spectroscopy of Atomically-Thin Two Dimensional Materials, Advances in the Application of Lasers in Materials Science, Springer2018, pp. 1-37.
[34] M. Mahjouri-Samani, M. Tian, K. Wang, A. Boulesbaa, C.M. Rouleau, A.A. Puretzky, M.A. McGuire, B.R. Srijanto, K. Xiao, G. Eres, Digital transfer growth of patterned 2D metal chalcogenides by confined nanoparticle evaporation, Acs Nano 8 (2014) 11567-11575.
[35] D.H. Lowndes, D. Geohegan, A. Puretzky, D. Norton, C. Rouleau, Synthesis of novel thin-film materials by pulsed laser deposition, Science 273 (1996) 898-903.
[36] M. Mahjouri‐Samani, R. Gresback, M. Tian, K. Wang, A.A. Puretzky, C.M. Rouleau, G. Eres, I.N. Ivanov, K. Xiao, M.A. McGuire, Pulsed laser deposition of photoresponsive two‐dimensional GaSe nanosheet networks, Advanced Functional Materials 24 (2014) 6365-6371.
[37] M. Mahjouri-Samani, M. Tian, A.A. Puretzky, M. Chi, K. Wang, G. Duscher, C.M. Rouleau, G. Eres, M. Yoon, J. Lasseter, K. Xiao, D.B. Geohegan, Nonequilibrium Synthesis of TiO_2 Nanoparticle "Building Blocks" for Crystal Growth by Sequential Attachment in Pulsed Laser Deposition, Nano Lett. 17 (2017) 4624-4633.
[38] M. Mahjouri-Samani, M.-W. Lin, K. Wang, A.R. Lupini, J. Lee, L. Basile, A. Boulesbaa, C.M. Rouleau, A.A. Puretzky, I.N. Ivanov, Patterned arrays of lateral

heterojunctions within monolayer two-dimensional semiconductors, Nature communications 6 (2015) 1-6.
[39] A.-Y. Lu, H. Zhu, J. Xiao, C.-P. Chuu, Y. Han, M.-H. Chiu, C.-C. Cheng, C.-W. Yang, K.-H. Wei, Y. Yang, Janus monolayers of transition metal dichalcogenides, Nature nanotechnology 12 (2017) 744-749.
[40] J. Zhang, S. Jia, I. Kholmanov, L. Dong, D. Er, W. Chen, H. Guo, Z. Jin, V.B. Shenoy, L. Shi, Janus monolayer transition-metal dichalcogenides, ACS nano 11 (2017) 8192-8198.
[41] L. Dong, J. Lou, V.B. Shenoy, Large in-plane and vertical piezoelectricity in Janus transition metal dichalchogenides, ACS nano 11 (2017) 8242-8248.
[42] A.C. Riis-Jensen, T. Deilmann, T. Olsen, K.S. Thygesen, Classifying the electronic and optical properties of Janus monolayers, Acs Nano 13 (2019) 13354-13364.
[43] B. Eggleston, S. Varlamov, M. Green, Large-area diode laser defect annealing of polycrystalline silicon solar cells, IEEE Transactions on Electron Devices 59 (2012) 2838-2841.
[44] C.-H. Kim, I.-H. Song, W.-J. Nam, M.-K. Han, A poly-Si TFT fabricated by excimer laser recrystallization on floating active structure, IEEE Electron Device Letters 23 (2002) 315-317.
[45] H. Kwon, W. Choi, D. Lee, Y. Lee, J. Kwon, B. Yoo, C.P. Grigoropoulos, S. Kim, Selective and localized laser annealing effect for high-performance flexible multilayer MoS 2 thin-film transistors, Nano research 7 (2014) 1137-1145.
[46] M.E. McConney, N.R. Glavin, A.T. Juhl, M.H. Check, M.F. Durstock, A.A. Voevodin, T.E. Shelton, J.E. Bultman, J. Hu, M.L. Jespersen, Direct synthesis of ultra-thin large area transition metal dichalcogenides and their heterostructures on stretchable polymer surfaces, Journal of Materials Research 31 (2016) 967-974.
[47] J.F. Fernando, C. Zhang, K.L. Firestein, D. Golberg, Optical and optoelectronic property analysis of nanomaterials inside transmission electron microscope, Small 13 (2017) 1701564.

[48] M. Tian, C. Liu, J. Ge, D. Geohegan, G. Duscher, G. Eres, Recent progress in characterization of the core–shell structure of black titania, Journal of Materials Research 34 (2019) 1138-1153.
[49] F.I. Allen, E. Kim, N.C. Andresen, C.P. Grigoropoulos, A.M. Minor, In situ TEM Raman spectroscopy and laser-based materials modification, Ultramicroscopy 178 (2017) 33-37.
[50] M. Picher, S. Mazzucco, S. Blankenship, R. Sharma, Vibrational and optical spectroscopies integrated with environmental transmission electron microscopy, Ultramicroscopy 150 (2015) 10-15.
[51] T. Kizuka, M. Oyama, Individual Cathodoluminescence and Photoluminescence Spectroscopy of Zinc Oxide Nanoparticles in Combination with <I>In Situ</I> Transmission Electron Microscopy, Journal of Nanoscience and Nanotechnology 11 (2011) 3278-3283.
[52] C.N. Marcus, P. Aaron, W. Ulrich, R. Christoph, Coherent x-ray diffraction imaging of photo-induced structural changes in BiFeO 3 nanocrystals, New Journal of Physics 18 (2016) 093003.
[53] X. Shen, R.K. Li, U. Lundstrom, T.J. Lane, A.H. Reid, S.P. Weathersby, X.J. Wang, Femtosecond mega-electron-volt electron microdiffraction, Ultramicroscopy 184 (2018) 172-176.
[54] B. Barwick, A.H. Zewail, Photonics and plasmonics in 4D ultrafast electron microscopy, Acs Photonics 2 (2015) 1391-1402.
[55] D. Shorokhov, A.H. Zewail, Perspective: 4D ultrafast electron microscopy—Evolutions and revolutions, The Journal of chemical physics 144 (2016) 080901.
[56] A. Howie, New instrumentation and cutting edge research, Ultramicroscopy 180 (2017) 52-58.
[57] A. Losquin, T.T.A. Lummen, Electron microscopy methods for space-, energy-, and time-resolved plasmonics, Frontiers of Physics 12 (2016) 127301.
[58] A.H. Zewail, Four-Dimensional Electron Microscopy, Science (New York, N.Y.) 328 (2010) 187.

[59] H. Boersch, J. Geiger, W. Stickel, Interaction of 25-keV Electrons with Lattice Vibrations in LiF. Experimental Evidence for Surface Modes of Lattice Vibration, Physical Review Letters 17 (1966) 379-381.
[60] J.C. Idrobo, A.R. Lupini, T. Feng, R.R. Unocic, F.S. Walden, D.S. Gardiner, T.C. Lovejoy, N. Dellby, S.T. Pantelides, O.L. Krivanek, Temperature Measurement by a Nanoscale Electron Probe Using Energy Gain and Loss Spectroscopy, Physical Review Letters 120 (2018) 095901.
[61] A. Howie, Electrons and photons: exploiting the connection Institute of Physics Conference Series 161 (1999) 311-4.
[62] F.J.G.d. Abajo, M. Kociak, Electron energy-gain spectroscopy, New Journal of Physics 10 (2008) 073035.
[63] B. Barwick, D.J. Flannigan, A.H. Zewail, Photon-induced near-field electron microscopy, Nature 462 (2009) 902.
[64] A. Yurtsever, J.S. Baskin, A.H. Zewail, Entangled Nanoparticles: Discovery by Visualization in 4D Electron Microscopy, Nano Letters 12 (2012) 5027-5032.
[65] E. Pomarico, I. Madan, G. Berruto, G.M. Vanacore, K. Wang, I. Kaminer, F.J. García de Abajo, F. Carbone, meV Resolution in Laser-Assisted Energy-Filtered Transmission Electron Microscopy, ACS Photonics 5 (2018) 759-764.
[66] F.J. García de Abajo, A. Asenjo-Garcia, M. Kociak, Multiphoton Absorption and Emission by Interaction of Swift Electrons with Evanescent Light Fields, Nano Lett 10 (2010) 1859-1863.
[67] S.T. Park, M.M. Lin, A.H. Zewail, Photon-induced near-field electron microscopy (PINEM): theoretical and experimental, New J Phys 12 (2010).
[68] A. Asenjo-Garcia, F.J. García de Abajo, Plasmon electron energy-gain spectroscopy, New Journal of Physics 15 (2013) 103021.
[69] F.J.G. García de Abajo, Optical excitations in electron microscopy, Rev Mod Phys 82 (2010) 209-275.

[70] X.-D. Xiang, X. Sun, G. Briceno, Y. Lou, K.-A. Wang, H. Chang, W.G. Wallace-Freedman, S.-W. Chen, P.G. Schultz, A combinatorial approach to materials discovery, Science 268 (1995) 1738-1740.
[71] K.L. Klein, A.V. Melechko, P.D. Rack, J.D. Fowlkes, H. Meyer, M.L. Simpson, Cu–Ni composition gradient for the catalytic synthesis of vertically aligned carbon nanofibers, Carbon 43 (2005) 1857-1863.
[72] Y. Wu, J.D. Fowlkes, P.D. Rack, The optical properties of Cu-Ni nanoparticles produced via pulsed laser dewetting of ultrathin films: The effect of nanoparticle size and composition on the plasmon response, Journal of Materials Research 26 (2011) 277-287.
[73] H. Zheng, Y.S. Meng, Y. Zhu, Frontiers of in situ electron microscopy, Mrs Bulletin 40 (2015) 12-18.
[74] M.L. Taheri, E.A. Stach, I. Arslan, P.A. Crozier, B.C. Kabius, T. LaGrange, A.M. Minor, S. Takeda, M. Tanase, J.B. Wagner, Current status and future directions for in situ transmission electron microscopy, Ultramicroscopy 170 (2016) 86-95.
[75] H. Zheng, Y. Zhu, Perspectives on in situ electron microscopy, Ultramicroscopy 180 (2017) 188-196.
[76] Y. Jiang, Z. Zhang, W. Yuan, X. Zhang, Y. Wang, Z. Zhang, Recent advances in gas-involved in situ studies via transmission electron microscopy, Nano Research 11 (2018) 42-67.
[77] X. Chen, C. Li, H. Cao, Recent developments of the in situ wet cell technology for transmission electron microscopies, Nanoscale 7 (2015) 4811-4819.
[78] B.K. Miller, P.A. Crozier, System for in situ UV-visible illumination of environmental transmission electron microscopy samples, Microscopy and Microanalysis 19 (2013) 461-469.
[79] F. Allen, E. Kim, N. Andresen, C. Grigoropoulos, A. Minor, In situ TEM Raman spectroscopy and laser-based materials modification, Ultramicroscopy 178 (2017) 33-37.

[80] J.S. Kim, T. LaGrange, B.W. Reed, M.L. Taheri, M.R. Armstrong, W.E. King, N.D. Browning, G.H. Campbell, Imaging of transient structures using nanosecond in situ TEM, Science 321 (2008) 1472-1475.
[81] B. Barwick, D.J. Flannigan, A.H. Zewail, Photon-induced near-field electron microscopy, Nature 462 (2009) 902-906.
[82] H. Liu, O.-H. Kwon, J. Tang, A.H. Zewail, 4D imaging and diffraction dynamics of single-particle phase transition in heterogeneous ensembles, Nano letters 14 (2014) 946-954.
[83] J. Li, W.-G. Yin, L. Wu, P. Zhu, T. Konstantinova, J. Tao, J. Yang, S.-W. Cheong, F. Carbone, J.A. Misewich, Dichotomy in ultrafast atomic dynamics as direct evidence of polaron formation in manganites, NPJ Quantum Materials 1 (2016) 1-7.
[84] M. Kaplan, B.K. Yoo, J. Tang, T.E. Karam, B. Liao, D. Majumdar, D. Baltimore, G.J. Jensen, A.H. Zewail, Photon‐Induced Near‐Field Electron Microscopy of Eukaryotic Cells, Angewandte Chemie 129 (2017) 11656-11659.
[85] N.A. Roberts, G.A. Magel, C.D. Hartfield, T.M. Moore, J.D. Fowlkes, P.D. Rack, In situ laser processing in a scanning electron microscope, Journal of Vacuum Science & Technology A: Vacuum, Surfaces, and Films 30 (2012) 041404.
[86] N.A. Roberts, C.M. Gonzalez, J.D. Fowlkes, P.D. Rack, Enhanced by-product desorption via laser assisted electron beam induced deposition of W (CO) 6 with improved conductivity and resolution, Nanotechnology 24 (2013) 415301.
[87] M.G. Stanford, B.B. Lewis, J.H. Noh, J.D. Fowlkes, P.D. Rack, Inert gas enhanced laser-assisted purification of platinum electron-beam-induced deposits, ACS applied materials & interfaces 7 (2015) 19579-19588.
[88] B.B. Lewis, R. Winkler, X. Sang, P.R. Pudasaini, M.G. Stanford, H. Plank, R.R. Unocic, J.D. Fowlkes, P.D. Rack, 3D Nanoprinting via laser-assisted electron beam induced deposition: growth kinetics, enhanced purity, and electrical resistivity, Beilstein journal of nanotechnology 8 (2017) 801-812.

[89] M.G. Stanford, B.B. Lewis, V. Iberi, J.D. Fowlkes, S. Tan, R. Livengood, P.D. Rack, In situ mitigation of subsurface and peripheral focused ion beam damage via simultaneous pulsed laser heating, Small 12 (2016) 1779-1787.
[90] M.G. Stanford, K. Mahady, B.B. Lewis, J.D. Fowlkes, S. Tan, R. Livengood, G.A. Magel, T.M. Moore, P.D. Rack, Laser-assisted focused he+ ion beam induced etching with and without XeF2 gas assist, ACS applied materials & interfaces 8 (2016) 29155-29162.
[91] M.G. Stanford, B.B. Lewis, K. Mahady, J.D. Fowlkes, P.D. Rack, Advanced nanoscale patterning and material synthesis with gas field helium and neon ion beams, Journal of Vacuum Science & Technology B, Nanotechnology and Microelectronics: Materials, Processing, Measurement, and Phenomena 35 (2017) 030802.
[92] M. Tian, O. Dyck, J. Ge, G. Duscher, Measuring the areal density of nanomaterials by electron energy-loss spectroscopy, Ultramicroscopy 196 (2019) 154-160.
[93] W.P. Huhn, B. Lange, V.W.-z. Yu, M. Yoon, V. Blum, GPU acceleration of all-electron electronic structure theory using localized numeric atom-centered basis functions, Comput. Phys. Commun. (2020) 107314.
[94] J.P. Perdew, K. Burke, M. Ernzerhof, Generalized gradient approximation made simple, Phys. Rev. Lett. 77 (1996) 3865–3868.
[95] A. Tkatchenko, M. Scheffler, Accurate molecular van der Waals interactions from ground-state electron density and free-atom reference data, Phys. Rev. Lett. 102 (2009) 073005.
[96] C.T. Koch, Determination of core structure periodicity and point defect density along dislocations, 2002.
[97] T. Vercauteren, X. Pennec, A. Perchant, N. Ayache, Diffeomorphic demons using ITK’s finite difference solver hierarchy, The Insight Journal 1 (2007).

[98] A. Alkauskas, S.D. Schneider, S. Sagmeister, C. Ambrosch-Draxl, C. Hébert, Theoretical analysis of the momentum-dependent loss function of bulk Ag, Ultramicroscopy 110 (2010) 1081-1086.
[99] G. Langer, J. Hartmann, M. Reichling, Thermal conductivity of thin metallic films measured by photothermal profile analysis, Review of Scientific Instruments 68 (1997) 1510-1513.
[100] G. Chen, P. Hui, Thermal conductivities of evaporated gold films on silicon and glass, Applied physics letters 74 (1999) 2942-2944.
[101] S.-M. Lee, D.G. Cahill, Heat transport in thin dielectric films, Journal of applied physics 81 (1997) 2590-2595.
[102] Y. Wu, C. Liu, T.M. Moore, G.A. Magel, D.A. Garfinkel, J.P. Camden, M.G. Stanford, G. Duscher, P.D. Rack, Exploring Photothermal Pathways via in Situ Laser Heating in the Transmission Electron Microscope: Recrystallization, Grain Growth, Phase Separation, and Dewetting in $Ag_{0.5}Ni_{0.5}$ Thin Films, Microsc. Microanal. 24 (2018) 647-656.
[103] A. Molina-Sánchez, M. Palummo, A. Marini, L. Wirtz, Temperature-dependent excitonic effects in the optical properties of single-layer MoS_2, Phys. Rev. B 93 (2016) 155435.
[104] L.H.G. Tizei, Y.-C. Lin, A.-Y. Lu, L.-J. Li, K. Suenaga, Electron energy loss spectroscopy of excitons in two-dimensional-semiconductors as a function of temperature, Appl. Phys. Lett. 108 (2016) 163107.
[105] S. Tongay, J. Zhou, C. Ataca, K. Lo, T.S. Matthews, J. Li, J.C. Grossman, J. Wu, Thermally driven crossover from indirect toward direct bandgap in 2D semiconductors: $MoSe_2$ versus MoS_2, Nano Lett. 12 (2012) 5576-5580.
[106] P.K. Gogoi, Y.C. Lin, R. Senga, H.P. Komsa, S.L. Wong, D. Chi, A.V. Krasheninnikov, L.J. Li, M.B.H. Breese, S.J. Pennycook, A.T.S. Wee, K. Suenaga, Layer rotation-angle-dependent excitonic absorption in van der Waals heterostructures revealed by electron energy loss spectroscopy, ACS nano 13 (2019) 9541-9550.

[107] C.Z. Liu, Y.Y. Wu, Z.W. Hu, J.A. Busche, E.K. Beutler, N.P. Monton, T.M. Moore, G.A. Magel, J.P. Camden, D.J. Masiello, G. Duscher, P.D. Rack, Continuous Wave Resonant Photon Stimulated Electron Energy-Gain and Electron Energy-Loss Spectroscopy of Individual Plasmonic Nanoparticles, ACS Photonics 6 (2019) 2499-2508.
[108] B.K. Choi, M. Kim, K.-H. Jung, J. Kim, K.-S. Yu, Y.J. Chang, Temperature dependence of band gap in $MoSe_2$ grown by molecular beam epitaxy, Nanoscale Res. Lett. 12 (2017) 1-7.
[109] K.P. O'donnell, X. Chen, Temperature dependence of semiconductor band gaps, Appl. Phys. Lett. 58 (1991) 2924-2926.
[110] A.A. Puretzky, Y.-C. Lin, C. Liu, A.M. Strasser, Y. Yu, S. Canulescu, C.M. Rouleau, K. Xiao, G. Duscher, D.B. Geohegan, In situ laser reflectivity to monitor and control the nucleation and growth of atomically thin 2D materials, 2D Mater. 7 (2020) 025048.
[111] Y. Zhang, T.R. Chang, B. Zhou, Y.T. Cui, H. Yan, Z. Liu, F. Schmitt, J. Lee, R. Moore, Y. Chen, H. Lin, H.T. Jeng, S.K. Mo, Z. Hussain, A. Bansil, Z.X. Shen, Direct observation of the transition from indirect to direct bandgap in atomically thin epitaxial MoSe2, Nat Nanotechnol 9 (2014) 111-5.
[112] A. Azizi, S. Eichfeld, G. Geschwind, K. Zhang, B. Jiang, D. Mukherjee, L. Hossain, A.F. Piasecki, B. Kabius, J.A. Robinson, N. Alem, Freestanding van der Waals heterostructures of graphene and transition metal dichalcogenides, ACS nano 9 (2015) 4882-4890.
[113] L. Fei, S. Lei, W.-B. Zhang, W. Lu, Z. Lin, C.H. Lam, Y. Chai, Y. Wang, Direct TEM observations of growth mechanisms of two-dimensional MoS_2 flakes, Nat. Commun. 7 (2016) 12206.
[114] N. Kondekar, M.G. Boebinger, M. Tian, M.H. Kirmani, M.T. McDowell, The Effect of Nickel on MoS_2 Growth Revealed with in Situ Transmission Electron Microscopy, ACS nano 13 (2019) 7117-7126.

[115] S.M. Eichfeld, L. Hossain, Y.C. Lin, A.F. Piasecki, B. Kupp, A.G. Birdwell, R.A. Burke, N. Lu, X. Peng, J. Li, A. Azcatl, S. McDonnell, R.M. Wallace, M.J. Kim, T.S. Mayer, J.M. Redwing, J.A. Robinson, Highly scalable, atomically thin WSe_2 grown via metal-organic chemical vapor deposition, ACS Nano 9 (2015) 2080–2087.

[116] R. Yue, Y. Nie, L.A. Walsh, R. Addou, C. Liang, N. Lu, A.T. Barton, H. Zhu, Z. Che, D. Barrera, L. Cheng, P.-R. Cha, Y.J. Chabal, J.W.P. Hsu, J. Kim, M.J. Kim, L. Colombo, R.M. Wallace, K. Cho, C.L. Hinkle, Nucleation and growth of WSe_2: enabling large grain transition metal dichalcogenides, 2D Mater. 4 (2017) 045019.

[117] X. Sang, X. Li, A.A. Puretzky, D.B. Geohegan, K. Xiao, R.R. Unocic, Atomic Insight into Thermolysis‐Driven Growth of 2D MoS_2, Adv. Funct. Mater. 29 (2019) 1902149.

[118] S.N. Grigoriev, V.Y. Fominski, R.I. Romanov, A.G. Gnedovets, M.A. Volosova, Shadow masked pulsed laser deposition of WSe_x films: Experiment and modeling, Appl. Surf. Sci. 282 (2013) 607-614.

[119] Y.C. Lin, B. Jariwala, B.M. Bersch, K. Xu, Y. Nie, B. Wang, S.M. Eichfeld, X. Zhang, T.H. Choudhury, Y. Pan, R. Addou, C.M. Smyth, J. Li, K. Zhang, M.A. Haque, S. Folsch, R.M. Feenstra, R.M. Wallace, K. Cho, S.K. Fullerton-Shirey, J.M. Redwing, J.A. Robinson, Realizing large-scale, electronic-grade two-dimensional semiconductors, ACS nano 12 (2018) 965-975.

[120] Y. Fan, A.W. Robertson, Y. Zhou, Q. Chen, X. Zhang, N.D. Browning, H. Zheng, M.H. Rümmeli, J.H. Warner, Electrical breakdown of suspended mono-and few-layer tungsten disulfide via sulfur depletion identified by in situ atomic imaging, ACS nano 11 (2017) 9435-9444.

[121] S.-Y. Chung, Y.-M. Kim, J.-G. Kim, Y.-J. Kim, Multiphase transformation and Ostwald’s rule of stages during crystallization of a metal phosphate, Nat. Phys. 5 (2009) 68-73.

[122] B.C. Bayer, R. Kaindl, M. Reza Ahmadpour Monazam, T. Susi, J. Kotakoski, T. Gupta, D. Eder, W. Waldhauser, J.C. Meyer, Atomic-scale in situ observations of crystallization and restructuring processes in two-dimensional MoS_2 films, ACS nano 12 (2018) 8758-8769.
[123] V.K. Ivanov, P.P. Fedorov, A.Y. Baranchikov, V.V. Osiko, Oriented attachment of particles: 100 years of investigations of non-classical crystal growth, Russ. Chem. Rev. 83 (2014) 1204–1222.
[124] Q. Zhang, S.-J. Liu, S.-H. Yu, Recent advances in oriented attachment growth and synthesis of functional materials: concept, evidence, mechanism, and future, J. Mater. Chem. 19 (2009) 191-207.
[125] D.M. Dabbs, I.A. Aksay, Self-assembled ceramics produced by complex-fluid templation, Annu. Rev. Phys. Chem. 51 (2000) 601-622.
[126] H. Zheng, R.K. Smith, Y.-w. Jun, C. Kisielowski, U. Dahmen, A.P. Alivisatos, Observation of single colloidal platinum nanocrystal growth trajectories, science 324 (2009) 1309-1312.
[127] D. Li, M.H. Nielsen, J.R. Lee, C. Frandsen, J.F. Banfield, J.J. De Yoreo, Direction-specific interactions control crystal growth by oriented attachment, Science 336 (2012) 1014-1018.
[128] D. Wang, G. Chen, C. Li, M. Cheng, W. Yang, S. Wu, G. Xie, J. Zhang, J. Zhao, X. Lu, P. Chen, G. Wang, J. Meng, J. Tang, R. Yang, C. He, D. Liu, D. Shi, K. Watanabe, T. Taniguchi, J. Feng, Y. Zhang, G. Zhang, Thermally induced graphene rotation on hexagonal boron nitride, Phys. Rev. Lett. 116 (2016) 126101.
[129] C.R. Woods, F. Withers, M.J. Zhu, Y. Cao, G. Yu, A. Kozikov, M. Ben Shalom, S.V. Morozov, M.M. van Wijk, A. Fasolino, M.I. Katsnelson, K. Watanabe, T. Taniguchi, A.K. Geim, A. Mishchenko, K.S. Novoselov, Macroscopic self-reorientation of interacting two-dimensional crystals, Nat. Commun. 7 (2016) 1-5.
[130] Y. Gong, S. Lei, G. Ye, B. Li, Y. He, K. Keyshar, X. Zhang, Q. Wang, J. Lou, Z. Liu, R. Vajtai, W. Zhou, P.M. Ajayan, Two-step growth of two-dimensional $WSe_2/MoSe_2$ heterostructures, Nano Lett. 15 (2015) 6135-6141.

[131] P.K. Nayak, Y. Horbatenko, S. Ahn, G. Kim, J.U. Lee, K.Y. Ma, A.R. Jang, H. Lim, D. Kim, S. Ryu, H. Cheong, N. Park, H.S. Shin, Probing evolution of twist-angle-dependent interlayer excitons in $MoSe_2/WSe_2$ van der Waals heterostructures, ACS Nano 11 (2017) 4041-4050.
[132] J. He, K. Hummer, C. Franchini, Stacking effects on the electronic and optical properties of bilayer transition metal dichalcogenides MoS 2, MoSe 2, WS 2, and WSe 2, Phys. Rev. B 89 (2014) 075409.
[133] K. Elibol, T. Susi, O.B. M, B.C. Bayer, T.J. Pennycook, N. McEvoy, G.S. Duesberg, J.C. Meyer, J. Kotakoski, Grain boundary-mediated nanopores in molybdenum disulfide grown by chemical vapor deposition, Nanoscale 9 (2017) 1591-1598.
[134] X. Zhao, Y. Ji, J. Chen, W. Fu, J. Dan, Y. Liu, S.J. Pennycook, W. Zhou, K.P. Loh, Healing of Planar Defects in 2D Materials via Grain Boundary Sliding, Adv. Mater. 31 (2019) 1900237.
[135] J.M. Yuk, M. Jeong, S.Y. Kim, H.K. Seo, J. Kim, J.Y. Lee, In situ atomic imaging of coalescence of Au nanoparticles on graphene: rotation and grain boundary migration, Chem. Commun. 49 (2013) 11479–11481.
[136] X. Li, L. Basile, B. Huang, C. Ma, J. Lee, I.V. Vlassiouk, A.A. Puretzky, M.W. Lin, M. Yoon, M. Chi, J.C. Idrobo, C.M. Rouleau, B.G. Sumpter, D.B. Geohegan, K. Xiao, Van der Waals Epitaxial Growth of Two-Dimensional Single-Crystalline GaSe Domains on Graphene, ACS Nano 9 (2015) 8078-88.
[137] F. Peymanirad, S. Kumar Singh, H. Ghorbanfekr-Kalashami, K.S. Novoselov, F.M. Peeters, M. Neek-Amal, Thermal activated rotation of graphene flake on graphene, 2D Mater. 4 (2017) 025015.
[138] J.J. De Yoreo, P.U. Gilbert, N.A. Sommerdijk, R.L. Penn, S. Whitelam, D. Joester, H. Zhang, J.D. Rimer, A. Navrotsky, J.F. Banfield, A.F. Wallace, F.M. Michel, F.C. Meldrum, H. Colfen, P.M. Dove, Crystallization by particle attachment in synthetic, biogenic, and geologic environments, Science 349 (2015) aaa6760.

[139] A. Puretzky, D. Geohegan, G. Hurst, M. Buchanan, B. Luk'yanchuk, Imaging of vapor plumes produced by matrix assisted laser desorption: a plume sharpening effect, Physical review letters 83 (1999) 444.
[140] D.B. Geohegan, A.A. Puretzky, C. Rouleau, J. Jackson, G. Eres, Z. Liu, D. Styers-Barnett, H. Hu, B. Zhao, I. Ivanov, Laser interactions in nanomaterials synthesis, Laser-Surface Interactions for New Materials Production, Springer2010, pp. 1-17.
[141] A. Berkdemir, H.R. Gutiérrez, A.R. Botello-Méndez, N. Perea-López, A.L. Elías, C.-I. Chia, B. Wang, V.H. Crespi, F. López-Urías, J.-C. Charlier, Identification of individual and few layers of WS 2 using Raman Spectroscopy, Scientific reports 3 (2013) 1-8.
[142] A. Kandemir, H. Sahin, Bilayers of Janus WSSe: monitoring the stacking type via the vibrational spectrum, Physical Chemistry Chemical Physics 20 (2018) 17380-17386.
[143] P. Das, J.D. Blazit, M. Tencé, L.F. Zagonel, Y. Auad, Y.H. Lee, X.Y. Ling, A. Losquin, C. Colliex, O. Stéphan, F.J. García de Abajo, M. Kociak, Stimulated electron energy loss and gain in an electron microscope without a pulsed electron gun, Ultramicroscopy 203 (2019) 44-51.
[144] S. Mukamel, Causal versus noncausal description of nonlinear wave mixing: Resolving the damping-sign controversy, Physical Review A 76 (2007) 021803.
[145] I. Bialynicki-Birula, T. Sowiński, Quantum electrodynamics of qubits, Physical Review A 76 (2007) 062106.
[146] D.J. Masiello, G.C. Schatz, Many-body theory of surface-enhanced Raman scattering, Physical Review A 78 (2008) 042505.
[147] E.M. Purcell, C.R. Pennypacker, Scattering and Absorption of Light by Nonspherical Dielectric Grains, Astrophysical Journal 186 (1973) 705-714.
[148] B.T. Draine, P.J. Flatau, Discrete-Dipole Approximation For Scattering Calculations, Journal of the Optical Society of America A 11 (1994) 1491-1499.

[149] U. Hohenester, A. Trügler, MNPBEM – A Matlab toolbox for the simulation of plasmonic nanoparticles, Computer Physics Communications 183 (2012) 370-381.
[150] N.W. Bigelow, A. Vaschillo, J.P. Camden, D.J. Masiello, Signatures of Fano Interferences in the Electron Energy Loss Spectroscopy and Cathodoluminescence of Symmetry-Broken Nanorod Dimers, ACS Nano 7 (2013) 4511-4519.
[151] N.W. Bigelow, A. Vaschillo, V. Iberi, J.P. Camden, D.J. Masiello, Characterization of the Electron- and Photon-Driven Plasmonic Excitations of Metal Nanorods, ACS Nano 6 (2012) 7497-7504.

VITA

Ms. Chenze Liu was born in Shaoyang City, Hunan Province, China in 1989. After graduation from high school in 2008, she entered the Department of Materials Science and Engineering at Central South University. She received her Bachelor's degree in 2012 and Master's degree in 2015. She joined Prof. Gerd Duscher's group in June 2016 to pursue a PhD degree in the Department of Materials Science and Engineering at the University of Tennessee, Knoxville.